Deformation Behavior and Microstructural Evolution of Armox 500T with Varying Strain Rates and Temperatures

Gurnek Tak

A Thesis submitted to the Faculty of Graduate Studies in Partial Fulfillment of the Requirements for the Degree of Master of Applied Science

Mechanical Engineering

York University, Toronto, Ontario

August 2024

Abstract

Armour steels have long been used for ballistic performance application purposes as they provide high hardness, toughness, and strength to resist penetration. However, literature lacks a complete understanding of failure mode analysis under various stress-loading conditions. This thesis explores the microstructure and evolution of Armox 500T as well as the correlated stress-strain data to characterize and gain a deeper understanding of its behaviour under compression, tension, and torsion with temperatures ranging from 0°C - 400°C. Results indicate that performance was increased in high strain rate compression at elevated temperatures up to 200°C, withstanding 2.0% more impact momentum and 3.7% higher toughness than room temperature samples. Temperatures above 200°C showed compromised microstructural properties and decreased performance. At 400°C high strain rate compression, the samples fractured at lower impact momentum and displayed increased brittleness and microhardness. In a reduced temperature of 0°C, low strain rate tensile test conditions decreased toughness by 11.8%.

Declaration

This work is supported by Defense Research and Development Canada (DRDC), General Dynamics Land Systems – Canada, and NP Aerospace through the NSERC Alliance project ALLRP 560447-2020. The observations, views, and conclusions in this document are those of the authors and should not be interpreted as representing the official policies, either expressed or implied, of General Dynamics, NP Aerospace, DRDC or the Government of Canada. The Government of Canada is authorized to reproduce and distribute reprints for Government purposes notwithstanding any copyright notation herein.

Acknowledgements

Firstly, I would like to thank the Lassonde Mechanical Engineering Department and all of its resources including staff, technicians, program directors, and professors for granting me the opportunity to pursue academia without restriction and for providing support during this period.

I would like to thank the members of my lab team as well as members from the Melenka lab group for all their assistance with testing, analysis, calculations, and late-night study sessions full of laughter. These events were entertained by the food of El Jefe De Pollo and their famous fried chicken sandwich recipe (which the lab collectively and successfully was able to reverse and engineer and reconstruct).

A special thank you to my family for their guidance, love, support, and belief in my abilities. For fueling my determination to always pursue excellence with my full capability and standing by me regardless of my shortcomings.

Dedication

To those who strive for greatness, challenge ideas, and challenge themselves. Despite doubts, failures, naysayers, and moments of hopelessness, we continue to press beyond our limits to achieve something far greater than most would think is possible. We dare to be different.

"*I'm a peacock, you've gotta let me fly!*" – Detective Terry Hoitz

Adam McKay, The Other Guys, 2010

Table of Contents

List of Figures

List of Tables

List of Abbreviations

ASB	Adiabatic Shear Band
ASM	American Society for Metals
ASTM	American Society for Testing and Materials
BCC	Body Centered Cubic
BCT	Body Centered Tetragonal
CNC	Computer Numerical Control
DAQ	Data Acquisition System
DHF	Ductile Hole Formation
DHPB	Direct Hopkinson Pressure Bar
DIC	Digital Image Correlation
DR	Dynamic Recovery
DRX	Dynamic Recrystallization
EDM	Electrical Discharge Machining
EDS	Energy Dispersive Spectroscopy
FCC	Face Centered Cubic
FEA	Finite Element Analysis
GISSMO	Generalized Incremental Stress-State Dependent Damage Model
HB	Brinell Hardness
HR	Rockwell Hardness
HRC	Rockwell hardness
LAVs	Light Armored Vehicles
MST	Martensitic Start Temperature

MTS	Materials Test System
NATO	North Atlantic Treaty Organization
NSERC	Natural Sciences and Engineering Research Council of Canada
OM	Optical Microscope
SEM	Scanning Electron Microscope
SSAB	Svenskt Stål AB
STANAG	Standardization Agreement

CHAPTER 1
Introduction

Since the beginning of global conflicts, methods of reducing casualties and protecting civilian lives have been sought out by countries around the world. In doing so, the development of suitable armour protection led highly specialized metallurgists to apply their technical knowledge and skills to create the world's first all steel vehicle in 1916 with steel plates no more than a few millimetres thick [1]. Now, well over a century later, the development of this field and its application have seen dramatic changes as weapons technology and projectile threats have become more advanced over the years including phases of homologous armour, aluminum-alloy armour, composite armour, reactive armour, and electromagnetic armour [2]. These armour plates have the necessity to be mobile, resistant to cracking, spalling, and fracture from a range of projectiles and impact conditions. Different grades of steels have been used to accomplish these criteria. What makes a grade of steel good for armour material is generally one with a high flow stress and high stiffness [3].

Low carbon steels which are less than 0.3% carbon content come in the form of ferritic microstructure, which has a low yield strength and is considered to be relatively soft [4]. Much higher carbon content steels, greater than 2% carbon content such as cast irons, are extremely brittle [5]. Both of these would therefore be considered unsuited as armour materials. It has been emphasized in industry that armours of 300 Brinell Hardness (HB) require careful manufacturing to prevent cracking and spallation [6]. Even with 0.95% carbon content tool steels, there were limitations of crack and discing failure [6].

Medium carbon grades (less than 0.6% carbon) of high-quality steels with the presence of alloying elements are generally selected for ballistic applications [7]. In the field of armour materials

engineering, the focus of development is concentrated on the research and development of materials with low density and high strength [1] [2]. These materials gain their strength through manufacturing methods such as quenching and tempering, allowing it to achieve a high strength and hardness martensitic microstructure. Hardenability and hardness are said to be the most important factors in armour steel designs, specifically in dynamic compression stresses, where the material is required to be strong throughout its entire thickness [8].

1.1 Ballistic Steels and Armour Applications in Modern Warfare

Armed forces around the world use many forms of armour as part of a grand-scale effort for personal protection and is well known for reducing fatalities in military environments [9]. With the rapid development of modern weapons systems and ongoing conflicts around the world, there is growing concern for the safety of military personnel [10]. Countries under war conditions such as Ukraine have made an effort to gather as many as 124,000 armour plates from across several North Atlantic Treaty Organization (NATO) countries [11]. Other parts of the world such as the Asia-Pacific region have become some of the fastest-growing markets for vehicle armour as a result of military modernization initiatives, political tensions, and overall economic growth in market opportunity [12]. The demand for improved material properties for ballistic armour plates, both on people and vehicles, has significantly increased with a roughly US$ 2.0 billion global market projected for 2023 [13]. Among this market, the demand for armoured tanks and bullet vehicles represents the largest demand as shown in Figure 1-1 [13].

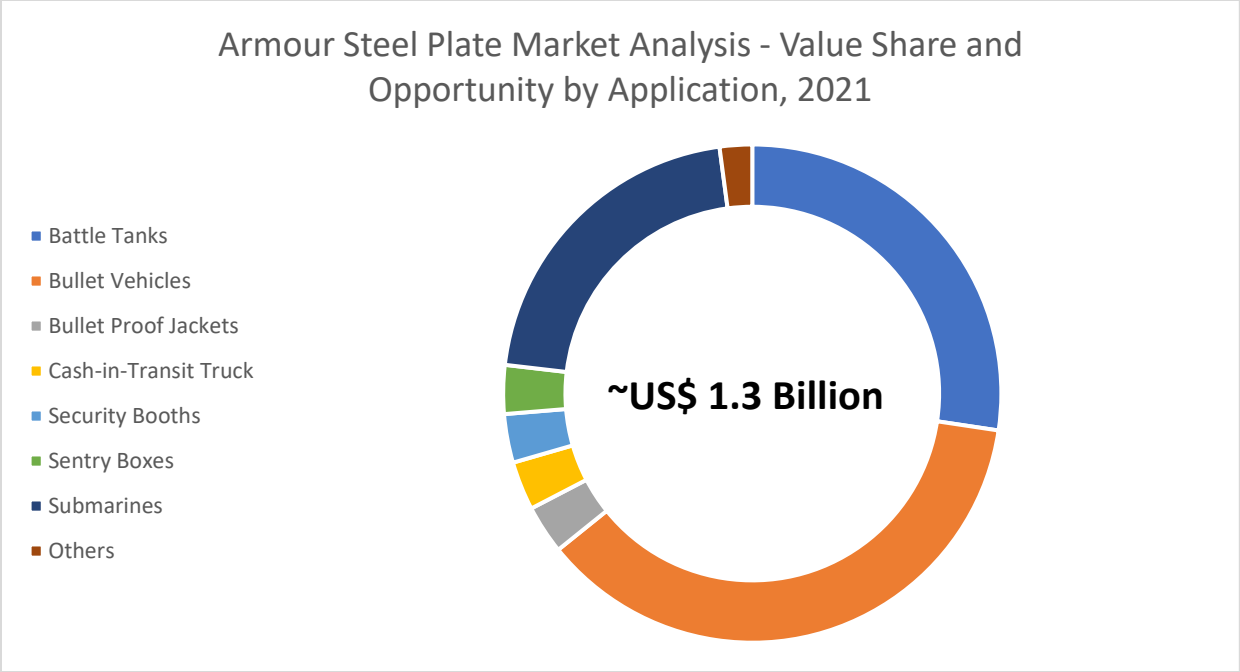

Figure 1-1: Armour steel plate market forecast analysis [13]

Ballistic armour has made many advancements over recent decades. A balance of high hardness and high toughness is what makes ballistic steels effective against high-calibre projectiles [8]. High-hardness steels such as AR500 [14] and ultra-high-hardness steels such as Armox Advance are a result of this development and are effective as defensive materials [9]. Advancements to Armox-based materials have further improved properties of weight and size while maintaining their favourable characteristics of high performance as demonstrated in Figure 1-2 [15].

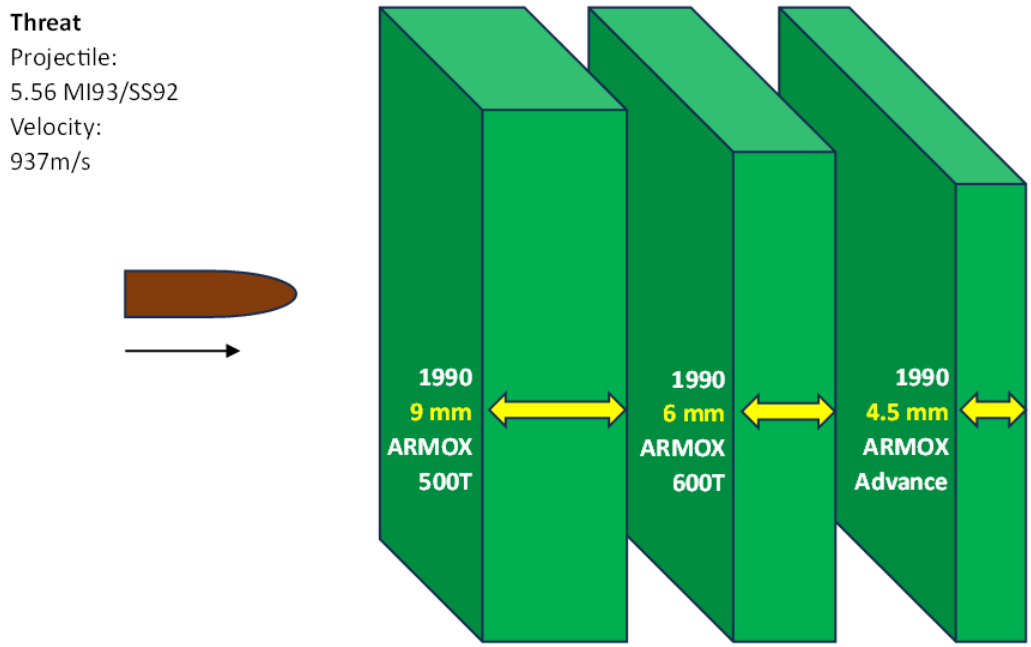

Figure 1-2: SSAB Armour plate technology over time demonstrating an equal amount of protection with less required material

1.2 Armox Steels

Svenskt Stål AB (SSAB), a company based out of Stockholm, Sweden develops and manufactures high-quality steel plates [16]. Amongst these quality steels is the Armox series, designed for high penetration resistance and blast protection as it is well renowned for its high toughness in relation to its hardness [17] [18]. The hardness of the material is achieved through the addition of carbon into the element matrix and the toughness is a result of the balanced use of elements as well as post-quenching heat treatment methods.

1.3 Application of Understanding

The aim is to develop Canadian-made, add-on armour for Light Armored Vehicles (LAVs), targeting protection against Standardization Agreement (STANAG) 4569 Level 6 threats. This is based on the NATO standardization determining protection levels of logistic and light armoured vehicles against threats of small and medium calibre kinetic energy ballistic projectiles and artillery shell fragment penetration [19]. The use of this research and data is geared toward material

characterization and experimentation, materials and armour system ballistic testing, modelling of materials and armour systems, armour design, development, and manufacturing. This work can also be used to create more accurate simulation models for armoured plating without the use of live round testing and expensive consumption of materials. This research also aims to fill current gaps in the literature as well as provide recommendations to future researchers in the field of ballistic defence materials studies. This thesis will focus mainly on material characterization and experimentation, specifically with Armox 500T.

The importance of being able to fully understand the material behaviour can be crucial for assisting in the manufacturing and performance of Armox 500T. For example, in combat scenarios, a bullet impact can increase the surface temperature of Armox 500T by 623-773 K [20]. Therefore, when a second shot is fired in close proximity to the first, the material will not have the same response. Because of this, high-temperature testing is critical to understanding the performance of Armox 500T in combat applications. It is also incredibly useful for the general characterization of the material because of the amount of data that is required for input when designing high-fidelity finite element analysis (FEA) and the Generalized Incremental Stress State dependent damage Model (GISSMO).

Overall, understanding the deformation behaviour and microstructural evolution of Armox 500T under high strain rate compression allows for the optimization of its mechanical properties. With enhanced knowledge of its abilities, the researchers and manufacturers can tailor the treatment processes to prepare the material for a desired application. Microstructural information achieved from testing will demonstrate when the material has failed, prior to its point of fracture through the indication of microcracks and deformation. This information is crucial to predict the failure of the material or identify any compromise that may not be visible in a typical stress-strain curve.

This combined with high-temperature conditions is rarely seen in literature as it has high complexity in system apparatus.

Similarly, the rotational force of projectiles can be very high and affect how it impacts the Armox 500T armour. Performing high-strain rate torsional testing with systematically greater forces can allow for a greater understanding of the material behaviour and be correlated with other high-strain rate available data. However, the Torsional Kolsky Bar testing apparatus is infrequently observed. In current public knowledge, York University possesses the only functioning one in Canada

Although high strain rate impact is the defensive application of Armox, quasistatic analysis is critical for general forces and stresses applied on an armoured vehicle. An often-overlooked testing condition is in reduced temperatures such as in vehicles used in arctic operations. It is also useful to understand the plastic forming methods when manufacturing complex shaped components around joints, bends, and corners of a vehicle.

1.4 Scope and Objective

The objective of this work is to study the microstructural effects of Armox with respect to varying strain rates and temperature exposure and to understand the mechanism of failure present in Armox 500T. This can be done by taking a systematic approach and using microstructural analysis as supporting evidence of how the material is affected at different points in the stress flow with respect to the temperature the material is subjected to. To accomplish this, the material underwent extensive testing and was exposed to a number of stresses including high strain rate deformation and quasistatic stresses under a range of thermal environments. These tests are critical in the application of the defense industry given the conditions the material must operate under.

Compression, tension, and torsion loading were performed to better characterize the material. This included various temperatures ranging from 0°C to 400°C. A specific temperature of interest for testing was 200°C because this temperature is where the material is tempered in its final stage of manufacturing [21] [22]. The tempering process is a crucial step in forming the initially strong microstructure of Armox 500T.

1.5 Thesis Outline

This thesis consists of six chapters. Chapter 2 begins with a literature review explaining current literature and the significant fundamental concepts and topics discussed throughout this paper. This chapter entails three main topics. First is the concept of varied strain rates and its effect on material plastic deformation. The second topic introduces the concept of adiabatic shear band formation including triggering mechanisms such as Dynamic Recrystallization (DRX) and Dynamic Recovery (DR). Lastly, the temperature dependence of Armox and its correlation with high strain rate deformation behaviour. These topics are collectively analyzed to summarize the gaps in the literature in which this research will serve a purpose as well as the scope and objective.

Chapter 3 covers the high strain rate compression testing with varying temperatures on Armox 500T. It begins with a detailed methodology, testing apparatus, and data processing. It then continues to the results and discussion which review the in-depth analysis that took place including stress-strain curves developed by a MATLAB code, optical microscope (OM) imaging, scan electron microscope (SEM) imaging, and Vickers hardness testing. All these categories are used to help characterize Armox 500T as a material and draw conclusions about its performance under high strain rate compression in various temperature conditions.

Chapter 4 outlines the quasistatic tensile load testing with varying temperatures on Armox 500T. It initiates with an introduction to the concept of this testing, detailed methodology, testing

apparatus, and data processing. It then moves to the results and discussion which covers stress-strain plotting developed in Microsoft Excel and MATLAB for data analysis, and then imaging to compare the performance of Armox 500T in each of the conditions. Finally, a conclusion is drawn from the results and discussion section.

Chapter 5 discusses the high strain rate torsion load testing on Armox 500T. This chapter begins with an introduction to the approach being taken and its importance to the understanding of this material. It also discusses this testing, detailed methodology, testing apparatus, and data processing before moving to the results and discussion which covers stress-strain plotting developed in Microsoft Excel and MATLAB for data analysis to compare the performance of Armox 500T. Finally, a conclusion is drawn from the results and discussion section.

Chapter 6 summarizes the findings of each chapter as well as future work that can provide further insight. This summary includes the overall performance of Armox 500T under various strain rates, applied loads, and temperatures based on evidence from imaging, data analysis, and hardness tests to draw a conclusion about the material`s behaviour. It also provides insight and recommendations for the use of Armox 500T in various environments. The future work part of this chapter explains the further testing or recommendations that could not be completed due to the timeframe or available resources.

1.6 References

[1] I. G. Crouch, "Metallic armour - from cast aluminium alloys to high-strength steels," *Materials Forum,* vol. 12, pp. 31-37, 1988.

[2] Y. Bao, X. Gao, Y. Wu, M. Sun and G. Li, "Research progress of armor protection materials," vol. 1855, no. 1, 2021.

[3] I. Crouch, S. Cimpoeru, H. Li and D. Shanmugam, "Armour steels," in *The Science of Armour Materials*, 2017, pp. 55-115.

[4] R. Singh, Classification of steels, Butterworth-Heinemann, 2020, pp. 53-60.

[5] K. Sotoodeh, "Corrosion study and material selection for cryogenic valves in an LNG plant," in *Cryogenic Valves for Liquefied Natural Gas Plants*, Gulf Professional Publishing, 2022, pp. 175-211.

[6] M. Edwards and A. Mathewson, "The ballistic properties of tool steel as a potential improvised armour plate," *International Journal of Impact Engineering,* vol. 19, no. 4, pp. 297-309, 1997.

[7] R. Singh, "Classification of Steels," in *Applied Welding Engineering (Second Edition)*, Butterworth-Heinemann, 2016, pp. 57-64.

[8] I. G Crouch, The science of armour materials, Elsevier Science, 2017.

[9] I. G. Crouch, "Body armour - New materials, new systems," *Defence Technology,* vol. 15, no. 3, pp. 241-253, 2019.

[10] B. Larsen, K. Netto and B. Aisbett, "The Effect of Body Armor on Performance, Thermal Stress, and Exertion: A Critical Review," *Military Medicine,* vol. 176, no. 11, pp. 1265-1273, 2011.

[11] T. Guest, "Ukraine's complex body armour story," *European Security & Defence,* February 2024.

[12] MarketsandMarkets, "Vehicle Armour Materials Market," 2024.

[13] Fact.MR, "Armour Steel Plate Market," October 2022. [Online]. Available: https://www.factmr.com/report/4659/armour-steel-plate-market. [Accessed 04 05 2023].

[14] Armored Republic, "Armored Republic AR500 Armor Body Armor," 2012. [Online]. Available: https://www.ar500armor.com/. [Accessed 04 05 2023].

[15] Army Technology, "SSAB: Armox Steel Protection Plates," 2023. [Online]. Available: https://www.army-technology.com/contractors/protection/ssab/. [Accessed 04 05 2023].

[16] A. Popławski, . P. Kędzierski and A. Morka, "Identification of Armox 500T steel failure properties in the modeling of perforation problems," *Materials & Design,* vol. 190, 2020.

[17] SSAB, "Armor steel protects people and property," 2023. [Online]. Available: https://www.ssab.com/en-ca/brands-and-products/steel-categories/armor-steel. [Accessed 06 05 2023].

[18] D. D. Showalter, W. Gooch, M. Burkins and R. Koch, "Ballistic testing of SSAB ultra-high-hardness steel for Armor Applications," in *Defense Technical Information Center*, 2008.

[19] North Atlantic Treaty Organization (NATO), "Standardization Agreement (STANAG)," 2004.

[20] A. Saxena, A. Kumaraswamy, N. Kotkunde and K. Suresh, "Constitutive modeling of high-temperature flow stress of armor steel in ballistic applications: A comparative study," *Journal of Materials Engineering and Performance,* vol. 20, no. 10, pp. 6505-6513, 2019.

[21] I. Barényi, P. Lipták and S. Vojtovič, "Effect of over tempering at UHSLA Steel Armox 500," *Advanced Materials Research,* pp. 1324-1328, 2014.

[22] M. Saleh, M. Kariem, V. Luzin, K. Toppler, H. Li and D. Ruan, "High strain rate deformation of ARMOX 500T and effects on texture development using neutron diffraction techniques and SHPB testing," *Materials Science and Engineering: A,* vol. 709, pp. 30-39, 2018.

CHAPTER 2
Literature Review

The objective of this work is to develop an understanding of the overall performance of Armox 500T under various temperature and strain rate conditions and conclude its method of failure as a result of these stresses. This chapter introduces the critical discussion topics and the extensive literature review of these topics. The following sections explain the fundamental principles based on the currently available literature on variable strain rate behaviour, stress collapse, Adiabatic Shear Bands (ASBs), and temperature-dependent testing. This chapter will also determine the purpose of the work being performed in this thesis based on the gaps in the literature that were identified.

The plastic flow of a material is governed by the motion of dislocations [1]. This involves the movement of atoms, atomic planes, vacancies, grain boundaries, twinning, and much more. These mechanisms are affected by the stress, strain rate, temperature, and microstructure of the material [1]. Stress is a highly investigated area of study when analyzing material properties. However, strain rate, temperature, and microstructural effects on the performance of a material are understudied, specifically when these conditions are coupled together. This makes it difficult to characterize and computationally understand the behaviour and stress response the material will have in a given design.

Traditional ballistics studies papers look at direct projectile impact and the effects it has on the armour material [2] [3] [4]. This thesis gains deeper insight as to exactly how these materials behave in a spectrum of stress conditions to create the most accurate understanding for characterization models. Furthermore, a microstructural analysis is used to explain the exact nature of the behaviour in each testing condition.

2.1 Armox Steels

The Armox steels are a series of high-performance ballistic protection metals manufactured by SSAB in Stockholm, Sweden. It has key properties such as its hardness and toughness, which allow it to excel in penetration resistance and blast protection [5] [6].

2.1.1 Armox Manufacturing

The Armox series is known to be a very clean steel with no more than 0.01% sulphur and phosphorus [7]. This is achieved by the production of iron through blast furnaces, steel deoxidation in an LD-converter, and vacuum treatment [6]. This involves the removal of excess oxygen from molten metal through the addition of carbon to the liquid steel to form carbon monoxide (CO), which can bubble out through the liquid [8]. The high quality of the fine-grained microstructure of austenitic grains is achieved through the use of the four-high hot rolling mill at a temperature of 1250°C before being solution annealed in oil at 850°C [9]. Beyond this, the steel is then quenched from 1000°C and tempered at 180-500°C [7] [9] [10]. The resultant microstructure of this process is a fine-tempered, high martensitic lathed structure [10]. The temperatures throughout the manufacturing process vary based on the types of steels SSAB offers. The manufacturing process can be seen in Figure 2-1.

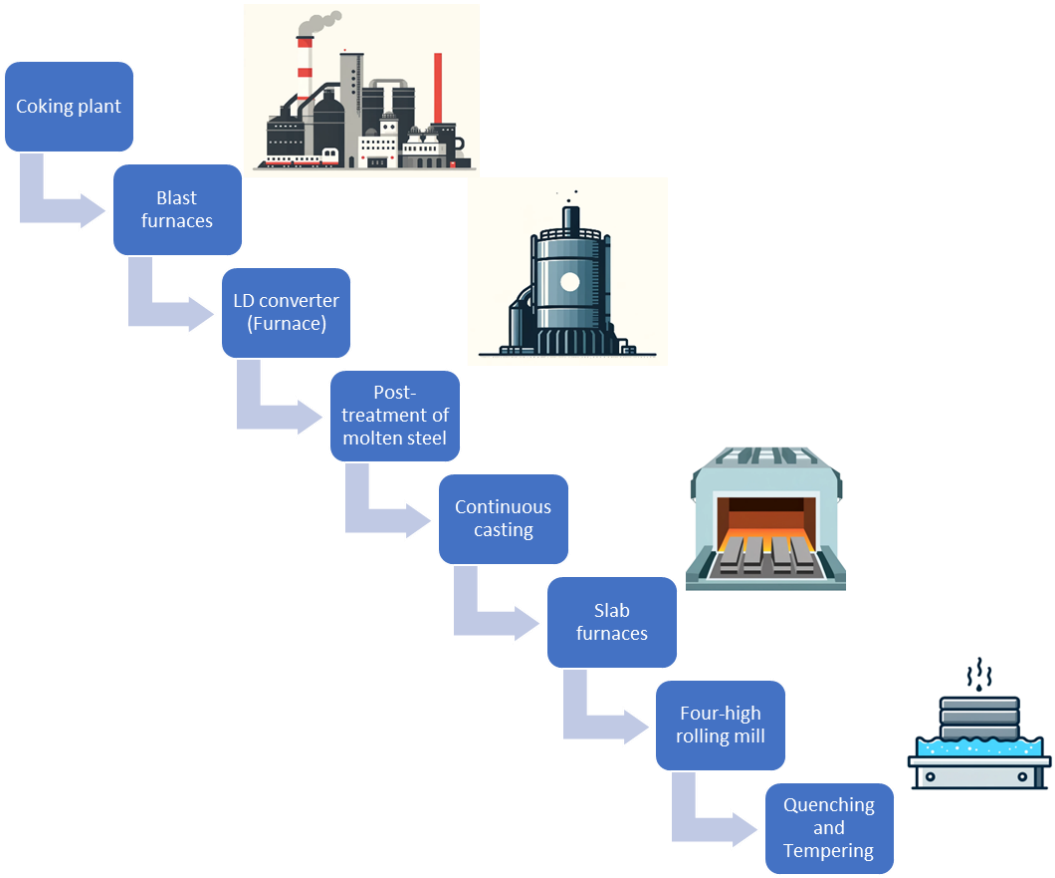

Figure 2-1: Production flow diagram at SSAB for ARMOX steel plate manufacture [6]

2.1.2 Armox 500T

As part of the SSAB Armox series, Armox 500T is a medium carbon steel that excels in high-strain rate applications. The quenching and tempering phase of the production heavily contributes to the unique balance of hardness and toughness in the steel [9]. This process gives the material a high martensitic structure and mechanical properties that allow this metal to be used in extreme loading conditions as shown in Figure 2-2. Table 2.1-1 shows the chemical composition of Armox 500T, demonstrating minimal impurities such as sulphur and phosphorus (less than 0.01%) and the hardenability of the steel which is increased by the chromium, molybdenum, manganese, and boron [7].

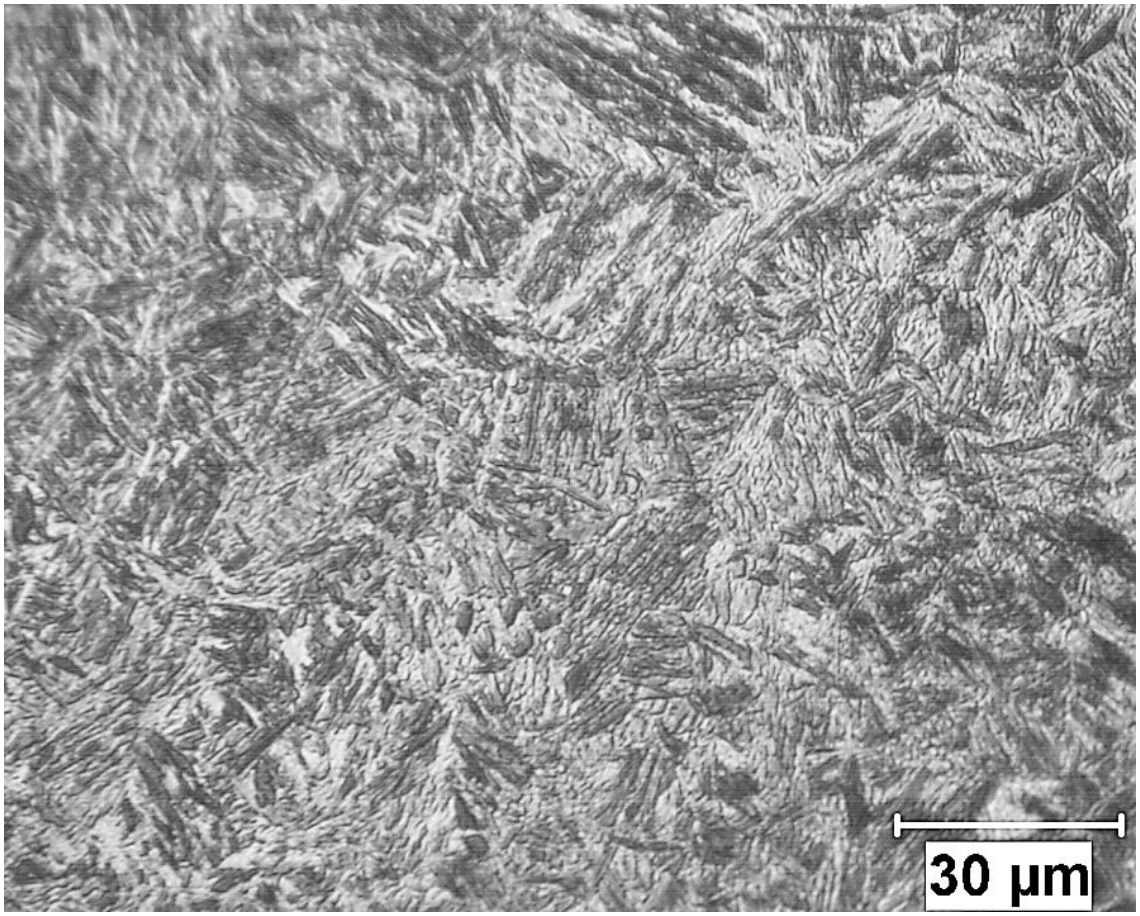

Figure 2-2: Optical microscope image of as-received martensitic microstructure of Armox 500T at 400x magnification

Ultimately, the main reason for the high hardness property is due to the high carbon content and quenched properties. Hardness measures the material's resistance to indentation, scratching, or penetration which is proportional to strength as shown in Table 2.1-2. Whereas, hardenability describes the potential for a steel to be hardened through treatment or deformation processes which are dependent on both the carbon content and the alloying elements as shown in Table 2.1-1 [11] [12]. Table 2.1-3 also demonstrates the hardness properties of high carbon steels such as Armox 500T with 99% martensitic transformation which are highlighted. Higher carbon content does not only increase the hardness of the material but also increases its potential hardness after martensitic transformation. Its transformation potential and microstructure are dependent on the iron-carbon phase diagram.

C (max %)	Si (max %)	Mn (max %)	P (max %)	S (max %)	Cr (max %)	Ni (max %)	Mo (max %)	B (max %)
0.32	0.4	1.2	0.010	0.003	1.0	1.8	0.7	0.005

Table 2.1-1: Chemical composition of Armox 500T (ladle analysis) [13]

Thickness (mm)	Hardness (HBW)	Hardness (HRC)	Yield strength $R_{p0.2}$ (min MPa)	Tensile strength R_m (MPa)	Elongation A_5 (min %)	Elongation A_{50} (min %)
3.0 - 80.0	480 - 540	51 - 55.5	1250	1450 - 1750	8	10

Table 2.1-2: Mechanical properties of Armox 500T [13]

Each of the elements from Table 2.1-1 plays a key role in the overall performance of Armox 500T. The silicon (Si) acts as a deoxidizer and increases the critical temperature of the steel [12]. The Manganese (Mn) increases hardenability in steel alloys and increases the critical cooling rate, allowing for enhanced quenching and hardness properties [12]. Chromium is able to form complex carbide structures in the presence of iron and carbon and greatly increases the hardenability and corrosion resistance in the steel [12]. However, excessive use of chromium can lead to oxidation on the surface and high carbide formation, decreasing the toughness [14] [12] [15]. Nickel (Ni), when combined with chromium in carbon steels, allows alloy steels to result in higher elastic ratios, hardenability, impact strength and fatigue resistance [12]. Molybdenum (Mo) helps to increase the hardenability in steels and is more potent than chromium [12]. The effects of sulphur and phosphorous are said to be negligible on thermal treatment [12]. These elements can have a significant overall influence on the hardness and performance of the material under various treatment processes [16].

Carbon %	Hardness (HRC)				
	99% Martensite	95% Martensite	90% Martensite	80% Martensite	50% Martensite
0.1	38.5	32.9	30.7	27.8	26.2
0.12	39.2	33.9	32.3	29.3	27.3
0.14	40.6	36.1	33.9	30.8	28.4
0.16	41.8	37.6	35.3	32.3	29.5
0.18	42.9	39.1	36.8	33.7	30.7
0.2	44.2	40.5	38.2	35	31.8
0.22	45.4	41.9	39.6	36.3	33
0.24	46.6	43.2	40.9	37.6	34.2
0.26	47.9	44.5	42.2	38.8	35.3
0.28	49.1	44.8	43.4	40	36.4
0.3	50.3	47	44.6	41.2	37.5
0.32	51.5	48.2	45.8	42.3	38.5
0.34	52.7	49.3	46.9	43.4	39.5
0.36	53.9	50.4	47.9	44.4	40.5
0.38	55	51.4	49	45.4	41.5
0.4	56.1	52.4	50	46.4	42.4
0.42	57.1	53.4	50.9	47.3	43.4
0.44	58.1	54.3	51.8	48.2	44.3
0.46	59.1	55.2	52.7	49	45.1
0.48	60	56	53.5	49.8	46
0.5	60.9	56.8	54.3	50.6	46.8
0.52	61.7	57.5	55	51.3	47.7
0.54	62.5	58.2	55.7	52	48.5
0.56	63.2	58.9	56.3	52.6	49.3
0.58	63.8	59.5	56.9	53.2	50
0.6	64.3	60	57.5	53.8	50.7

Table 2.1-3: Effect of Carbon Concentration and Martensite Content on the As-Quenched Hardness of Steel [11]

The significant properties and manufacturing process of Armox 500T are better understood through the iron-carbon phase diagram seen in Figure 2-3 describes the various phases of steel based on its carbon content and temperature. Iron generally comes in the form of a Body Centered Cubic (BCC) structure, also known as ferrite as depicted in Figure 2-4. Armox 500T has a carbon composition of 0.32% and according to the iron-carbon phase diagram, at elevated temperatures such as hot rolled manufacturing temperature of Armox 500T (1250°C), this structure enters the austenitic phase and becomes a Face Centered Cubic (FCC) structure. During this transition period,

there is enough space for a carbon atom to position itself inside the atomic structure. Hardenability, based on transformation diagrams, is defined by the critical cooling rate [12] [17] [18]. In steels the critical cooling rate is defined as the minimum rate that austenitic steel is continuously cooled to suppress transformations, producing 100% martensitic microstructure [19]. This can be achieved if the material is cooled fast enough through the process of quenching, where there is not enough time for the carbon atoms to diffuse out of the material matrix and it maintains its position in what is then considered a Body-Centered Tetragonal (BCT) structure, otherwise known as martensite. The BCT structure results in packets of lathes in the microstructure with overlapping grains in multiple orientations as seen in Figure 2-5. This allows Armox to have high hardness and high strength in multiple directions. The reason for the final tempering phase is that quenching can cause high hardness but high brittleness because of the extreme martensitic transformation and internal stresses within the Armox from this manufacturing process. Tempering offers a form of stress relief resulting in some ferrite structures [20]. This reduces the hardness of the overall material, however, increases the toughness and makes it less brittle [20] [21]. The eutectoid temperature is a point that allows for one solid phase to transform isothermally into two solid phases upon cooling [22]. The microstructure of Armox 500T and its sensitivity to specific temperatures make it important to study its thermomechanical model and characterization.

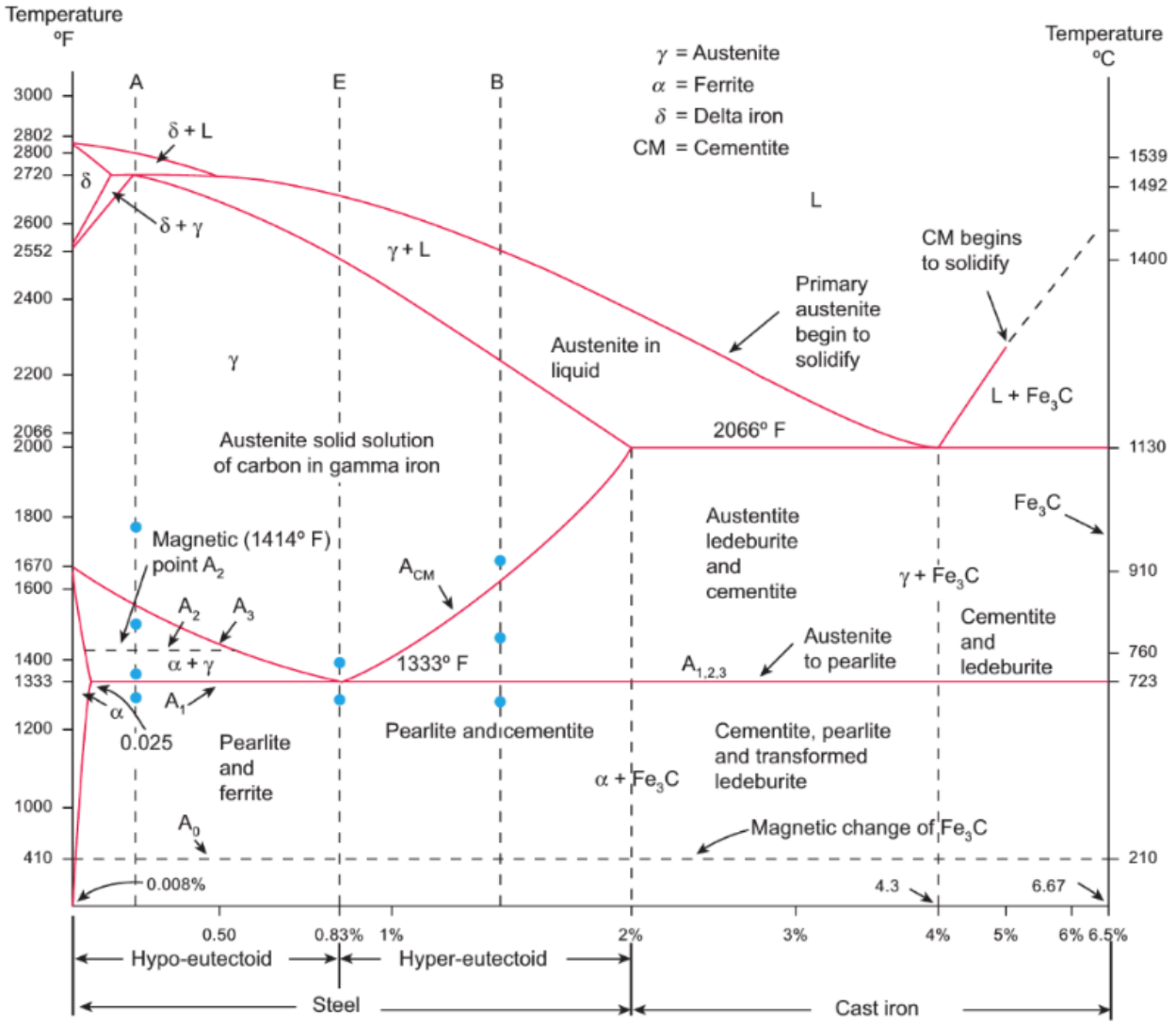

Figure 2-3: Iron-carbon phase diagram [17] [23]

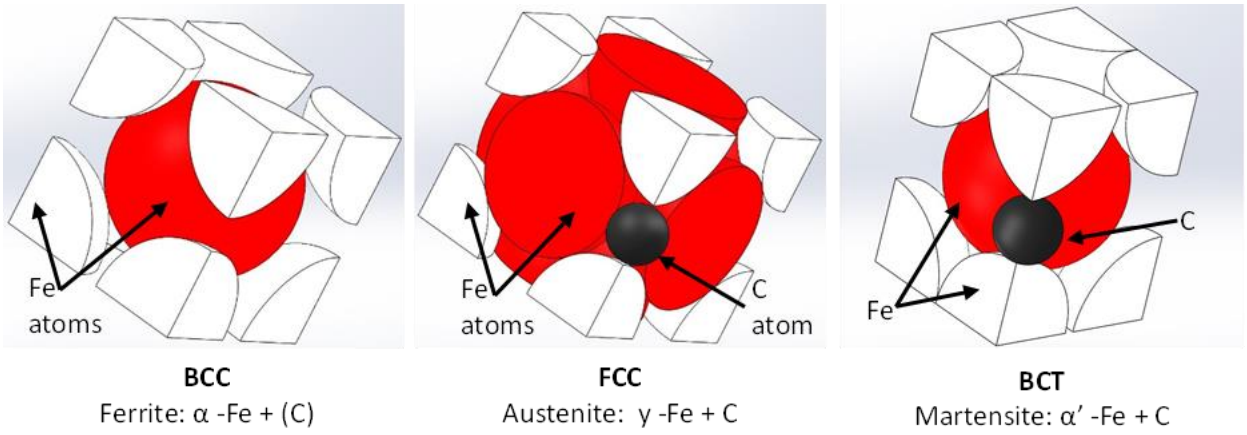

Figure 2-4: Visual of FCC, BCC and BCT structures respectively [24]

Recent literature suggests that for a high degree of ballistic protection, steel must have the following characteristics [23]:

- Through-hardened steel of uniform high hardness
- A fine equiaxed grain size, free from microsegregation
- A martensitic start temperature (MST) of less than 210°C
- A volume fraction of retained austenite of >1% in a bed of plate martensite

The martensitic start temperature (MST) of the metal is required to be low as it increases the likelihood of a complete transformation to martensite during quenching. A high MST could result in an incomplete transformation, mainly in thicker sections, which can lead to a heterogeneous microstructure. A low MST also allows for a wider tempering window, which can be used to reduce brittleness and improve toughness. The manufacturing method of Armox 500T allows for an extremely high martensitic structure with well-balanced retained austenite. It also results in a homogenous fine equiaxed grain structure which is important when involving the Hall-Petch relationship, where, the yield strength in a polycrystalline material increases as the grain size decreases [25]. Armox 500T fits all of these criteria, making it an optimal-performing ballistic steel.

2.1.3 Energy Dispersive Spectroscopy (EDS)

Energy Dispersive Spectroscopy is an analytical technique commonly used in conjunction with SEM to provide information about the elemental composition of a material's surface microstructure. It allows for the identification of the types of elements present and their relative concentrations within a particular region of interest in the sample including ASB regions. This analysis can help describe the relationship between the material’s composition and its mechanical behaviour, deformation mechanisms, and performance under different conditions.

2.1.4 As Received Armox EDS Analysis

The EDS in the as-received sample very simply demonstrates a high presence of iron, along with its alloying elements. The specifications of the analysis can be seen in the table below. These elements are evenly distributed throughout the surface of the material as seen in Figure 2-5 - Figure 2-8. These figures demonstrate that the martensitic properties affect the microstructure by creating a homogeneous distribution of all detectable elements. This eliminates typical grain boundaries, rolling direction properties, and anticipated points of failure seen in other high-performance metals.

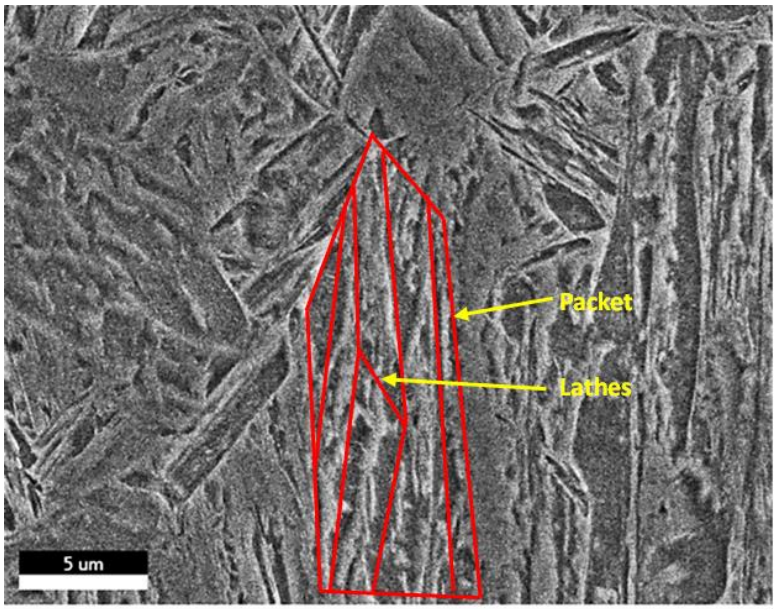

Figure 2-5: Scan electron microscope image of as-received sample used for EDS scan (5006x magnification)

Sum Spectrum SEM Specifications

kV	20
Magnification	5006
Takeoff	30.9
Live time	3.9
Amp Time	1105.9
Resolution (eV)	3.84

Table 2.1-4: Sum spectrum scan electron microscope specifications of as-received sample

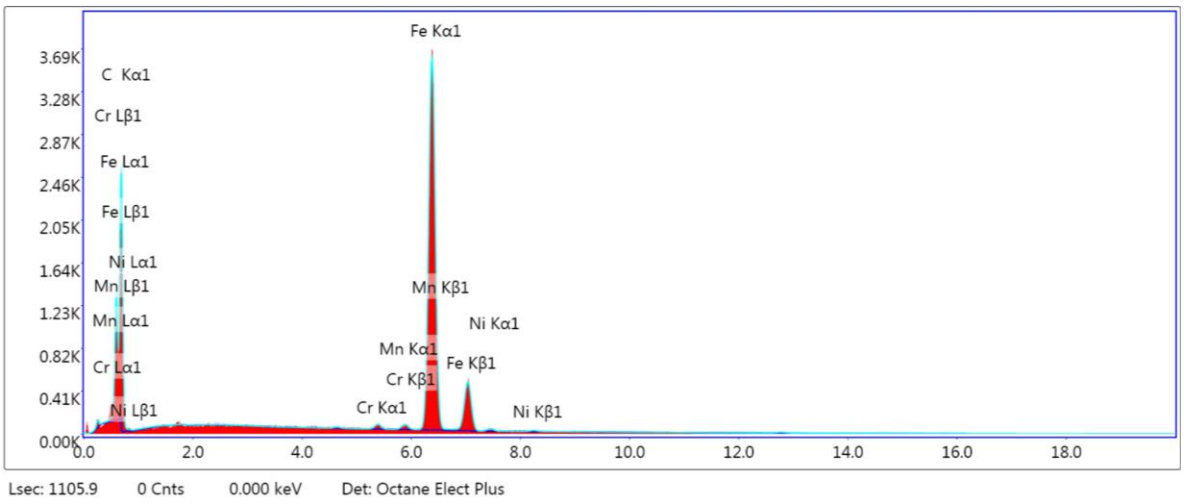

Figure 2-6: EDS spectrum analysis of the as-received sample

eZAF Smart Quant Results

Element	Weight	Atomic	Net Int.	Kratio	Z	A	F
C K	4.75	18.82	0.30	0.0131	1.2991	0.2124	1.0000
FeL	90.99	77.52	13.90	0.7539	0.9836	0.8424	1.0000
CrK	1.24	1.13	0.60	0.0165	0.9854	0.9900	1.3661
MnK	1.51	1.31	0.50	0.0167	0.9659	0.9966	1.1478
NiK	1.51	1.22	0.30	0.0153	0.9953	0.8780	1.1621

Table 2.1-5: Elemental breakdown from EDS spectrum analysis of the as-received sample

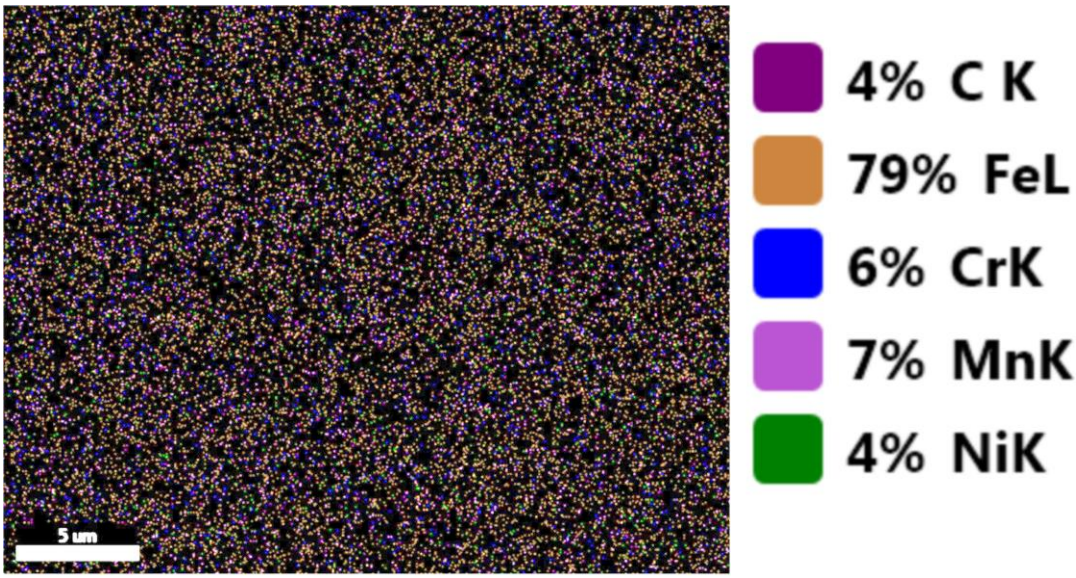

Figure 2-7: EDS elemental imaging of as-received sample including carbon, iron, chromium, manganese, and nickel

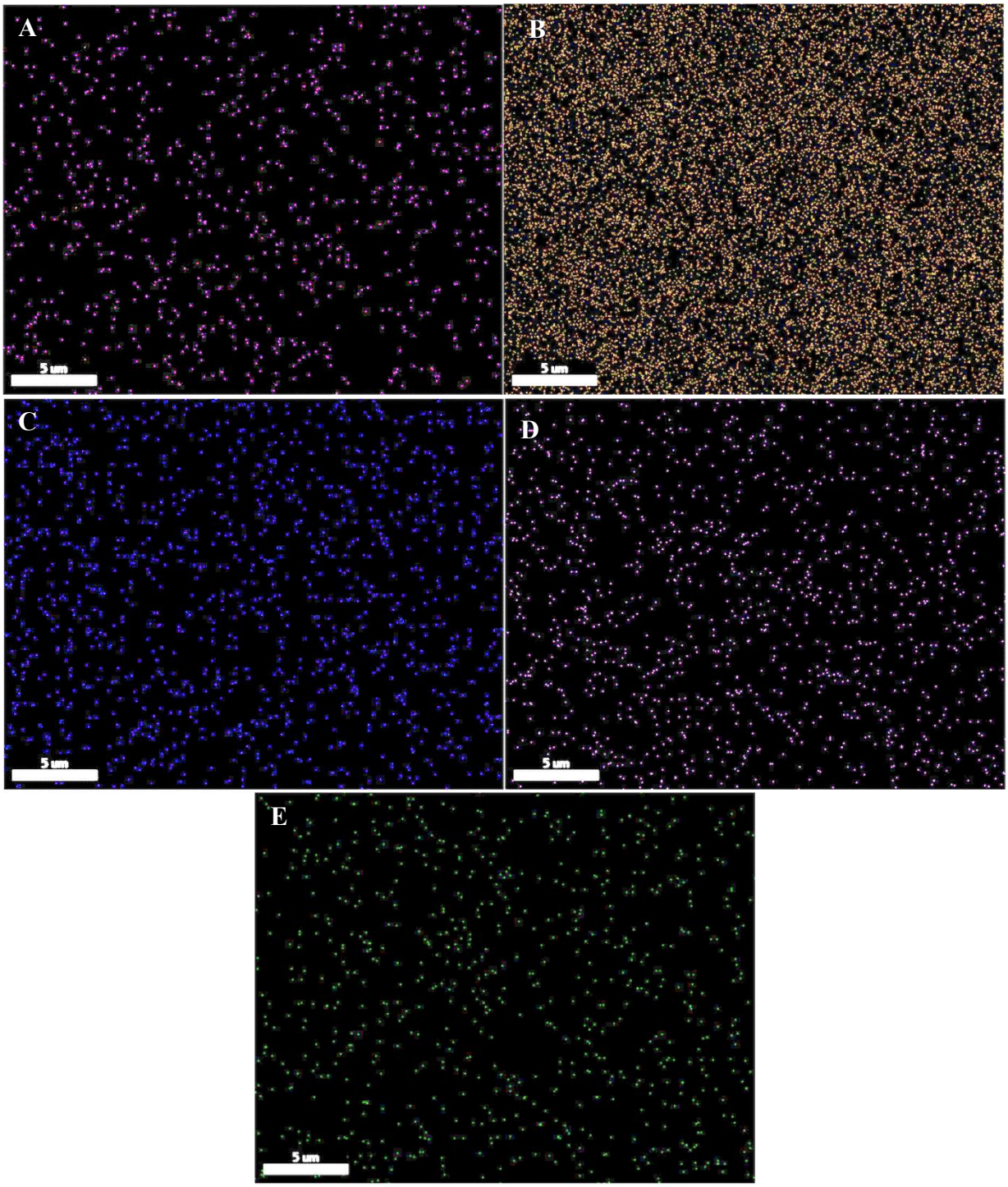

Figure 2-8: EDS individual elemental imaging of as-received Armox 500T sample including carbon (A), iron (B), chromium (C), manganese (D), and nickel (E)

2.1.5 Failure Modes for Ballistics

Under ballistics conditions, material failure may occur in many different ways as seen in Figure 2-9. Low-hardness materials are subject to ductile hole formation (DHF) [23]. In stronger

materials, soft plugging may occur as a result of through-thickness shearing around the shape of the projectile [23]. With harder materials, this is referred to as hard plugging, where there is less ductility and plastic deformation around the projectile and the possibility of shrapnel [23]. This is a result of having a high hardness, but reduced toughness material, compromising its ability to absorb impact energy.

High hardness can be correlated with ballistic armour performance. However, hardness is a quasistatic measure from an indentor that is associated with low strain rate plastic flow, meaning that it is not necessarily a measure of dynamic flow stress, yield, strain rate hardening, work hardening, or thermal softening, which are typically associated with ballistic conditions.

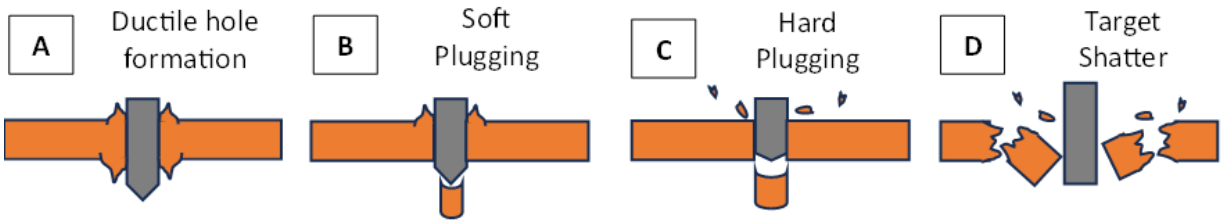

Figure 2-9: Various ballistic failure modes based on material properties [23]

2.2 Strain Rates

A fundamental concept in materials science is strain rate, where, it describes the speed at which a deformation of a material occurs over a length of time. Mathematically this is represented as:

$$\dot{\varepsilon} = \frac{d\varepsilon}{dt}$$ Equation 2.2-1

Where:
$\dot{\varepsilon}$ = strain rate
$d\varepsilon$ = change in strain
dt = change in time

Strain rates can have a significant effect on material properties and behaviour as some materials are subject to strain hardening, strain-rate sensitivity, or a thermal response. Strain rates are generally broken down into three different categories:

2.2.1 Quasistatic (Low Strain Rate):

This entails a strain rate range of 0-1 s^{-1}. This allows something called a global stress distribution where the strain rate is slow enough to distribute the defects, boundaries, and atoms throughout the entire material. The result is a low energy concentration, which is why the temperature effects are negligible in this case.

2.2.2 Dynamic (High Strain Rate):

Strain rates higher than 10^2 s^{-1} are considered dynamic, where the stress distribution becomes highly localized with a high energy concentration resulting in the possibility of significant temperature increase during the plastic deformation phase and the flow stress is coupled with temperature [26].

Oftentimes, when measuring dynamic material properties, a high strain rate uniaxial compression system is used as it allows for the ability to produce large strains resembling ballistic impact. The effect of strain rate seen in the performance of a material in terms of stress-strain is a result of the increase in flow stress known as strain hardening or strain rate effect [23].

The overall flow stress of dynamic scenarios is affected by both strain rate and temperature. This thermally activated component is related to short-range obstacles such as point defects and dislocations. These obstacles can be overcome by means of thermally activated glide of mobile slip dislocations [23].

In cases of higher levels of strain rates, high-temperature concentration leads to something called stress collapse. This is the loss of load capacity in the material during its plastic phase in which higher strain rates result in faster stress collapse [27]. This leads to thermal softening of the material, which in turn gives the material thermomechanical instability.

Alternative theories such as Baxevanis' state that stress collapse is caused by diffusion of alloying elements [28]. Where, either mechanically or thermally, the alloying elements diffuse out of the original material in the stress-concentrated areas, leaving the less stable or strong material as a result. This area then forms stress concentrations where the material becomes vulnerable to stress collapse.

Conversely, Nazimuddin`s theory is that stress collapse occurs in the non-homogenous sections of the material [29]. This implies that the impurities and defects in the material are targeted, leading to the failure of bonds in the microstructure. These differing theories demonstrate the lack of understanding and conclusiveness drawn from literature and research.

2.3 Adiabatic Shear Bands (ASB)

Shortly after stress collapse occurs in a material, the visible appearance of localized stress regions are seen in the formation of adiabatic shear bands [27]. Literature states that shear bands are a result of thermal softening mechanisms [30]. However, other studies demonstrate that the maximum temperature reached in the material is achieved after the shear band has already formed and thermal softening effects can be neglected [31] [27].

Adiabatic shear bands are localized zones of intense deformation that form in materials which undergo rapid loading conditions, such as high-velocity impacts or explosive events. During this dynamic or high strain rate deformation, significant amounts of energy are rapidly applied to the material, leading to the generation of intense stress waves. These stress waves propagate through the material, causing localized regions of intense deformation. Adiabatic shear bands are the result of this localized deformation process. Adiabatic shear bands serve as evidence that a stress collapse has occurred in the material and is considered the failure of the material's integrity. They appear as a narrow strip of localized stress with grain distortion and at times microvoids, which

demonstrates areas susceptible to forming crack initiation and possibly failure [23] [32]. They are also identifiable by its increased hardness properties compared to the pre-impacted surface or area outside of the ASB region [33] [34].

There are generally two classifications of ASBs, deformed bands and transformed bands. Deformed bands do not undergo a phase transformation, but are still subject to recrystallization due to the high temperature that is caused by the localization [35]. Transformed bands undergo phase transformations and are much more distinctive and tend to have lower coefficients of thermal diffusivities [35]. An example of these ASBs can be seen in Figure 2-10.

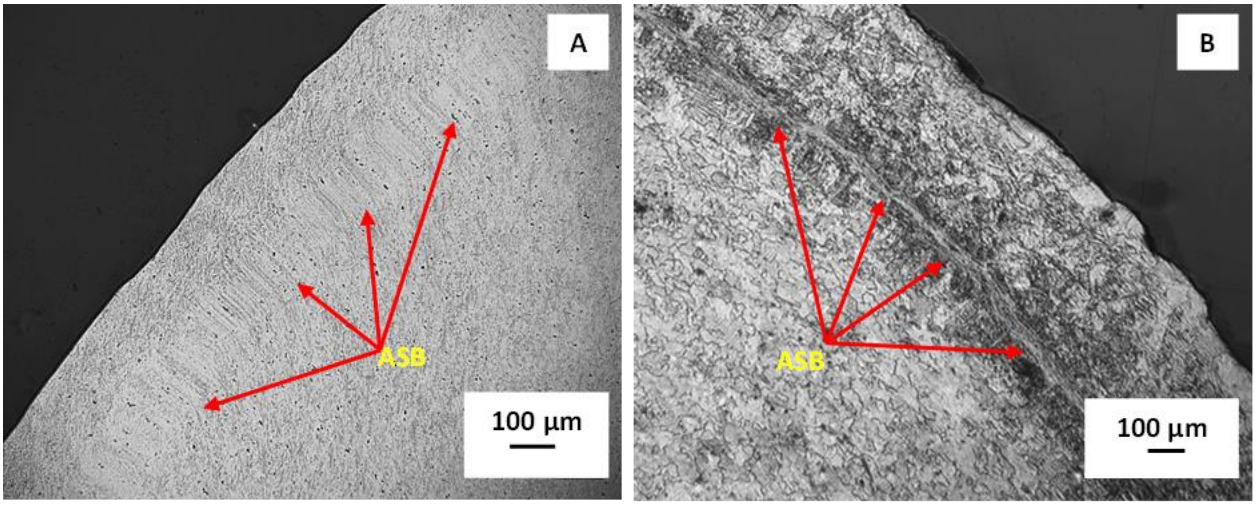

Figure 2-10: Optical microscope images of Al 7075 at 100x magnification showing a deformed band (A) and transformed band (B)

2.3.1 Formation of Adiabatic Shear Bands

The mechanisms involved in the formation of adiabatic shear bands are complex and can vary depending on the material and loading conditions. However, there are several theories and commonly observed mechanisms discovered:

2.3.1.1 Thermomechanical mechanism:

The rapid deformation and high strain rate generate heat within the material due to internal friction. This rapid and local thermal increase can soften the material, reducing its resistance to deformation and facilitating the formation of shear bands [36] [37].

2.3.1.2 Microstructural mechanism:

This can include serval factors including material properties, such as strain rate sensitivity, thermal conductivity, microstructure, and shear strength. This also includes strain localization and shear localization, dynamic recrystallization and dynamic recovery.

Understanding the mechanisms of formation of adiabatic shear bands is highly important as it explains the material response to specific conditions including conditions in which it may be susceptible to failure by means of crack initiation and failure. Studies have shown that cracks and microvoids follow the path of ASBs to connect themselves in a failure or compromising situation as illustrated in Figure 2-11 and Figure 2-12 [35].

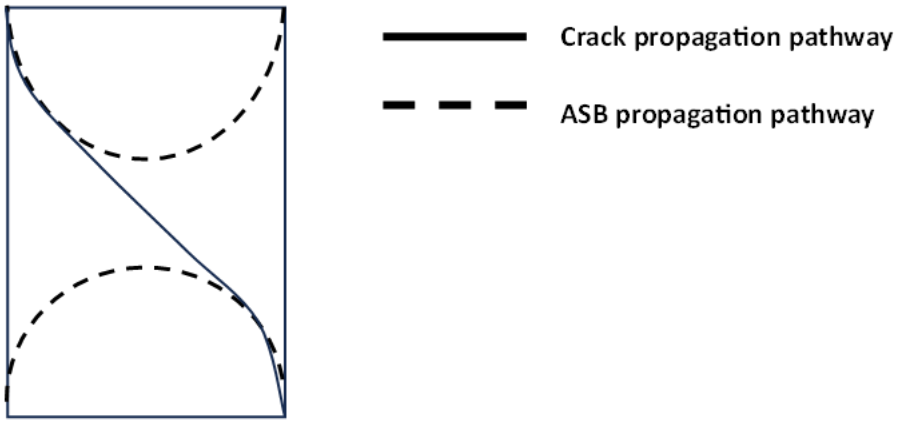

Figure 2-11: Crack propagation path with ASB in a cylindrical specimen

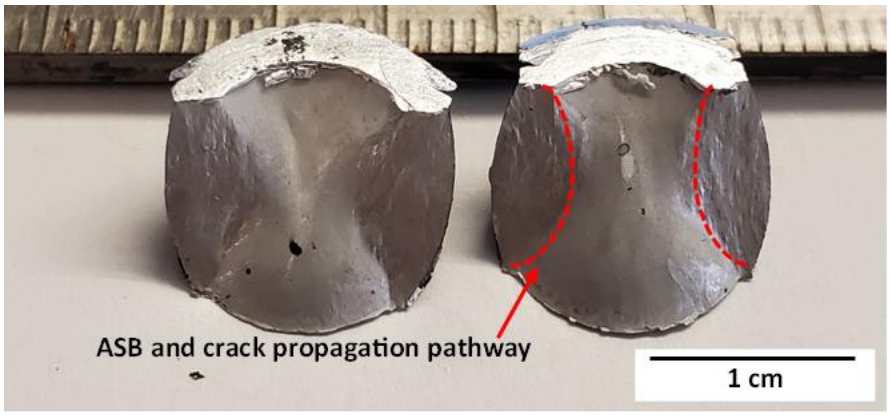

Figure 2-12: High strain-rate Al 7075 cylindrical compression specimen fracture shape

2.3.2 Thermomechanical Mechanisms Causing Adiabatic Shear Bands

Evidence through experimental analysis and models have proven a significant rise in temperature upon high strain rate impact. These temperatures can reach high enough to alter the original microstructure of the material causing instability and affecting its originally intended performance and mechanical properties. Rusinek explains that a high stain rate causes high dislocation density, which leads to strain hardening [26]. However, the dislocation density also results in a significant thermal effect high enough to thermally soften the material, which supersedes the strain-hardening effect, resulting in stress collapse and ultimately failure. Similar to this theory, Pelleg states in his work that the local increase in temperature causes thermal softening which, when greater than the work hardening induces instability of the plastic deformation and adiabatic shear band nucleation sets in [38]. However, the same study mentions that brittle failure is attributed to strain localization without mention of why these particular regions are targeted when the material is placed under high strain rate conditions. Controversial to these theories, the thermal effect of the material response is not enough to cause ultimate failure. It also does not justify the extreme localization of the stress and why the remainder of the microstructure, depending on the material sees distinctly different effects. The ASBs also have been proven in several studies to show high hardness after impact compared to the rest of the impacted surface due to its high dislocation density. However,

if the rise in temperature and its effect were significant, these dislocations should be thermally stress-relieved, resulting in lower hardness.

2.3.3 Microstructural Mechanisms Causing Adiabatic Shear Bands

In thermomechanical mechanism theories, the strain is assumed to be limited to the highly concentrated shear band regions. These theories overlook the effects of high strain rate deformation on the remainder of the microstructure of the material. The deformation can also be a result of the presence of microstructural heterogeneities, such as grain boundaries or second-phase particles and may be affected by dislocation behaviour, where the motion of dislocations within the material can interact between obstacles such as grain boundaries or precipitates, influencing the initiation and growth of ASBs. This is seen in literature as Feng and Bassim also suggest that the promotion of ASBs are initiated by the presence of geometrical imperfections [39]. In other studies, Rittel and Osovski stated that the process can be viewed as triggered by dynamic recrystallization rather than the universally assumed thermal softening theory [40]. This indicates that the initiation and formation of adiabatic shear bands require further investigation in order to reach a converging theory or explanation.

2.3.4 Dynamic Recrystallization and Dynamic Recovery

The formation of ASBs can be very complex and difficult to understand. However, two important phenomena can be used to explain this type of deformation behavior in metals under dynamic loading conditions, dynamic recrystallization and dynamic recovery. The process of large deformation and plastic work being converted to heat during dynamic loading conditions can trigger the nucleation and growth of new grains, otherwise referred to as dynamic recrystallization (DRX) [41]. DRX regions within shear bands can appear to have an alternate microstructure from the original unstrained material. These properties are widely explained by two concepts, nucleation

and grain growth. Nucleation is known to develop around vulnerable regions in the microstructure such are grain boundaries, triple junctions, defects or other structural features that provide favourable conditions where atoms can rearrange themselves into a more stable structure. This new grain structure is very refined in appearance and with continuous heat, these grains can consume atoms surrounding it, leading to grain growth.

During heavy plastic deformation, dynamic recovery can be seen as it produces ultrafine grains with both high and low-angle grain boundaries. DR refers to some restoration of a dislocation structure and occurs simultaneously during the generation of dislocation densities of nanocrystalline structures and the annihilation of these dislocations through various mechanisms such as cross-slip and reactions with vacancies. Dynamic recovery aids in minimizing the accumulation of dislocations and relieves internal stresses, increasing the ductility of the metal.

It has been reported by Rittel that the stored energy of cold work was the driving force for the rearrangement of the microstructure by DRX, then resulting in adiabatic shear bands [40]. This indicates that the internal stresses within a microstructure can trigger DRX and DR influence the formation of adiabatic shear bands and contribute to failure. Both dynamic recrystallization and dynamic recovery are dependent on several factors such as temperature, strain rate, material properties, and amount of strain. These phenomena can be observed in different materials to help understand the mechanical priorities and behaviour in untested materials.

2.4 Temperature Dependent Testing

The application of Armox 500T on armoured vehicles makes the material subject to harsh environments and extreme conditions. These conditions include northern arctic regions of deployment as well as operations in high-heat environments [42]. For these reasons, it is critical

that the performance of this material is judged in simulated environments to achieve accurate characterization and understanding of its behaviour.

2.4.1 High-Temperature Performance of Armox 500T

Depending on the amount of temperature and time of exposure, the microstructure of Armox 500T can be significantly affected in its performance capability. The most common effect on steel is the softening of the material. As temperature increases, there is a decrease in the resistance to dislocations and increased mobility of atoms. This results in reduced strength, load-bearing capacity, and hardness [43]. It could also cause recrystallization in which, new grain structures are formed and the previous deformation structures are eliminated including mechanisms that cause internal stresses within the material [44]. With extremely elevated temperatures, the material could lose its original quenched martensitic microstructure and return to an austenitic phase. With prolonged exposure, the result can cause decarburization where the carbon atoms that give the material its strength and hardness properties will diffuse out of the material matrix, compromising the original microstructure and properties of Armox. Studies reported by Rogers, Yildirim, Ravichandra, and Molinari revealed that more than 90% of energy in high strain rate deformation of metals is dissipated in the form of heat [45] [46] [47] [48] [49].

Particularly around 200°C, carbon begins to precipitate from the martensite of Armox [10] [50]. This makes its temperature and conditions above it, a range of interest for the science and defence community [9].

2.4.2 Low-Temperature Performance of Armox 500T

The exposure of Armox to low and cryogenic temperatures can also have a significant effect on its performance. The most common characteristic that shows in steel is embrittlement. The temperature could increase the dislocation density in the material causing more internal stresses

and leading to a brittle failure. This increased dislocation density and limited dislocation mobility could also lead to increased strength and hardness. In some cases, high carbon steels with exposure to cryogenic treatment saw a reduction of retained austinite and greater martensitic structure [51] [52].

2.4.3 High Strain Rate Coupled with Temperature Loading

Significant importance can be placed on the high strain rate coupled with temperature loading and its effect on the microstructure of Armox 500T. Ballistic impacts can range in strain rates from 10^2 – 10^3 s^{-1} [45]. This could lead to stress collapse, adiabatic shear bands, diffusion of alloying elements, crack initiation, propagation, and failure. All of these factors can compromise the integrity of the material and should be thoroughly studied for better understanding. As it stands currently, there are very few publicly available sources to confirm a high strain rate test coupled with high temperature performed for Armox.

2.5 Observations from Current Studies

Experiments performed with temperature coupled with different strain rates were rarely seen. It is evident that temperature has a high influence on the microstructure of metals such as Armox and its response behaviour to various strain conditions [20] [45].

Many journals and papers investigate the low and high strain rate effects on metals, yet, the emphasis strain rate effects and the gradual development of adiabatic shear bands is often overlooked. When these ASBs are observed in studies, it is with minimal experimental data and insight, leading to various opinions as to how the cracks initiate and propagate leading to failure.

Furthermore, the microstructure has an impact on the flow stress behaviour of the material. Current studies may show the pre-testing and post-mortem analysis of the microstructure, however,

samples are generally not analyzed throughout the progression of tests from low to high strain, nor are they correlated with the quantitative data from the testing they underwent.

Beyond this, there are significant gaps in the literature relating to the effects of high strain rate torsional stresses on Armox 500T. With most of its applications being for high-strain rate circumstances, this is a crucial part of developing a thorough understanding of the material's behaviour.

Being that Armox 500T is designed for ballistic performance, the material behaviour and characterization data are very limited as it is a classified material for military use in many countries.

Armox 500T has been well observed and tested under several conditions. Yet there is very limited data and information regarding the performance of this material under sub-zero operating temperatures. Given that this material is said to be designed for light armour vehicles, the operating conditions of this vehicle and its amour are exposed to both high heat and arctic low-temperature conditions [42]. For this reason, it is critical that Armox is able to withstand ballistic stresses and maintain its performance standard.

2.6 Proposed Studies

To address the existing gaps in the literature, the following proposed studies serve as a comprehensive approach. Firstly, high strain-rate compression testing was conducted and will be discussed in Chapter 3, covering a spectrum of strain rates leading progressively to specimen fracture and failure. This test matrix will be extended to include exposure to incrementally elevated temperatures. Subsequently, the specimens will undergo grinding, polishing, etching, and imaging processes to discern significant microstructural changes, including the formation of adiabatic shear

bands. The impact data will be utilized for the analysis of specific properties such as stress, strain, and toughness.

Additionally, low strain-rate tensile testing will be completed in Chapter 4, spanning a range of temperatures, including sub-room temperature conditions. This approach will provide insight into stress, strain, toughness, and failure data, which will be analyzed and compared across the specified temperature range. The mode of failure will be identified through imaging and fractography analysis.

Furthermore, high strain-rate torsional testing will be implemented in Chapter 5 using a progressively increasing strain rate. This study will result in data regarding stress, strain, and toughness, laying the groundwork for subsequent testing. This particular testing equipment and procedure has not been previously used for Armox, and therefore, will contribute insight to existing literature.

2.7 References

[1] B. Babu, "Physically based model for plasticity and creep of ti-6al-4v," Luleå , 2008.

[2] E. Konca, "A Comparison of the Ballistic Performances of Various Microstructures in MIL-A-12560 Armor Steel," *Metals,* vol. 10, no. 4, 2020.

[3] P. Si, "Ballistic Performance of Polyurea-Reinforced Ceramic/Metal Armor Subjected to Projectile Impact," *Materials,* vol. 15, 2022.

[4] C.-J. Hu and P.-Y. Lee, "Ballistic performance and microstructure of modified rolled homogeneous armor steel," *Journal of the Chinese Institute of Engineers,* vol. 25, no. 1, pp. 99-107, 2002.

[5] SSAB, "Armor steel protects people and property," 2023. [Online]. Available: https://www.ssab.com/en-ca/brands-and-products/steel-categories/armor-steel. [Accessed 06 05 2023].

[6] D. D. Showalter, W. Gooch, M. Burkins and R. Koch, "Ballistic testing of SSAB ultra-high-hardness steel for Armor Applications," in *Defense Technical Information Center*, 2008.

[7] Z. Opiekun, B. Kupiec and M. Lenik, "TECHNOLOGICAL PROCESS OF WELDING," in *Materials, technologies, constructions: Special purpose materials*, Oficyna Wydawnicza Politechniki Rzeszowskiej, 2019.

[8] J. Lancaster, "Carbon and ferritic alloy steels," *Metallurgy of Welding,* pp. 211-309, 1999.

[9] I. Barényi, P. Lipták and S. Vojtovič, "Effect of over tempering at UHSLA Steel Armox 500," *Advanced Materials Research,* pp. 1324-1328, 2014.

[10] M. Saleh, M. Kariem, V. Luzin, K. Toppler, H. Li and D. Ruan, "High strain rate deformation of ARMOX 500T and effects on texture development using neutron diffraction techniques and SHPB testing," *Materials Science and Engineering: A,* vol. 709, pp. 30-39, 2018.

[11] G. Totten, C. Bates and N. Clinton, "Chapter 2 – Measuring Hardenability and Quench Severity," in *Handbook of Quenchants and Quenching Technology*, Materials Park, OHIO: ASM International, 1993, pp. 35-68.

[12] L. Canale, L. Albano, G. Totten and L. Meekisho, "Hardenability of Steel," *Comprehensive Materials Processing,* pp. 39-97, 2014.

[13] SSAB, "Data sheet 195 Armox 500T," 2017.

[14] S. Preston, "Influence of vanadium on the hardenability of a carburizing steel," *Journal of Heat Treating,* vol. 8, no. 2, pp. 93-99, 1990.

[15] G. Eldis and Y. Smith, "New Developments in Carburizing Steels," in *Metals Engineering Quarterly*, vol. 16, American Society for Metals, 2008, pp. 13-20.

[16] J. Agyapong, "Additive Manufacturing of Novel Cemented Carbides with Self Lubricating Properties," Toronto, 2019.

[17] "Behaviour of Heated and Naturally Cooled Steel Tubular Joints," in *FiRE2014At: IIT Roorkee*, 2014.

[18] L. Canale, J. Vatavuk and G. Totten, "Introduction to Steel Heat Treatment," in *Comprehensive Materials Processing*, Elsevier, 2014, pp. 3-37.

[19] G. Krauss, Steels: Heat Treatment and Processing Principles, Materials Park, OHIO: ASM International, 1990, p. 457.

[20] I. Barenyi, O. Hires and P. Liptak, "Changes in Mechanical Properties of Armoured UHSLA Steel ARMOX 500 After Over Tempering," in *Problems of Mechatronics Armament Aviation Safety Engineering*, 2013, pp. 7-14.

[21] I. Barényi, P. Lipták and S. Vojtovič, "Effect of over tempering at UHSLA Steel Armox 500," *Advanced Materials Research,* pp. 1324-1328, 2014.

[22] Cambridge University Engineering Department, "The Eutectoid Reaction," 2023. [Online]. Available: http://www-g.eng.cam.ac.uk/mmg/teaching/typd/addenda/eutectoidreaction1.html#:~:text=In%20the%20Fe%2DC%20system,temperature%20(723%C2%B0C)..

[23] I. Crouch, S. Cimpoeru, H. Li and D. Shanmugam, "Armour steels," in *The Science of Armour Materials*, 2017, pp. 55-115.

[24] J.-P. Brog, C.-L. Chanez, A. Crochet and K. M. Fromm, "Polymorphism, what it is and how to identify it: A systematic review," *RSC Advances,* vol. 3, no. 38, pp. 16905-16931, 2013.

[25] S. Whang, "Introduction," in *Nanostructured Metals and Alloys*, Woodhead Publishing Series in Metals and Surface Engineering, 2011, pp. xxi-xxxv.

[26] A. Rusinek, "Shear testing of a sheet steel at wide range of strain rates and a constitutive relation with strain-rate and temperature dependence of the flow stress," *International Journal of Plasticity,* vol. 17, no. 1, pp. 87-115, 2001.

[27] Y. Guo, Q. Ruan, S. Zhu, Q. Wei, H. Chen, J. Lu, B. Hu, X. Wu, Y. Li and D. Fang, "Temperature Rise Associated with Adiabatic Shear Band: Causality Clarified," *Physical Reiew Letters,* vol. 122, no. 1, 2019.

[28] T. Baxevanis, T. Katsaounis and A. Tzavaras, "Adaptive Finite Element Computations of Shear Band Formation," *Mathematical Models and Methods in Applied Sciences,* vol. 20, no. 3, pp. 423-448, 2010.

[29] G. Nazimuddin, "High strain rate studies of armor materials," Winnipeg, 2010.

[30] B. Mishra, P. Jena, B. Ramakrishna, V. Madhu, T. Bhat and N. Gupta, "Effect of tempering temperature, plate thickness and presence of holes on ballistic impact behavior and ASB formation of a high strength steel," *International Journal of Impact Engineering,* vol. 44, pp. 17-28, 2012.

[31] P. Longère, "Respective/combined roles of thermal softening and dynamic recrystallization in adiabatic shear banding initiation," *Mechanics of Materials,* vol. 117, pp. 81-90, 2018.

[32] D. Mateos, "Stress-State and Strain-Rate Dependent Multiscale Characterization of Armox 500T," Toronto, 2023.

[33] S. Cimpoeru, "The Mechanical Metallurgy of Armour Steels," 2016.

[34] M. C. Jo, "Understanding of adiabatic shear band evolution during high-strain-rate deformation in high-strength armor steel," *Journal of Alloys and Compounds,* vol. 845, 2020.

[35] A. Odeshi, S. Al-ameeri, S. Mirfakhraei, F. Yazdani and M. Bassim, "Deformation and failure mechanism in AISI 4340 steel under Ballistic Impact," *Theoretical and Applied Fracture Mechanics,* vol. 45, no. 1, 2006.

[36] A. Marchand and J. Duffy, "An experimental study of the formation process of adiabatic shear bands in a structural steel," *Journal of the Mechanics and Physics of Solids,* vol. 36, no. 3, pp. 251-283, 1988.

[37] D. Rittel and Z. Wang, "Thermo-mechanical aspects of adiabatic shear failure of AM50 and Ti6Al4V alloys," *Mechanics of Materials,* vol. 40, no. 8, pp. 629-635, 2008.

[38] J. Pelleg, "Fracture in AM and traditional manufactured components," *Additive and Traditionally Manufactured Components,* pp. 499-585, 2020.

[39] H. Feng and M. Bassim, "Finite element modeling of the formation of adiabatic shear bands in Aisi 4340 Steel.," vol. 266, no. 1-2, pp. 255-260, 1999.

[40] D. Rittel and S. Osovski, "Dynamic failure by adiabatic shear banding," *IUTAM Symposium on Dynamic Fracture and Fragmentation,* pp. 177-185, 2010.

[41] S. Boakye-Yiadom, "Microstructural Evolution of Adiabatic Shear Bands in Steel," Winnipeg, 2014.

[42] Government of Canada/Gouvernement du Canada, "Light Armoured Vehicle (LAV) 6.0," 10 02 2021. [Online]. Available: https://www.canada.ca/en/army/services/equipment/vehicles/light-armoured-vehicle-upgrade.html. [Accessed 01 11 2023].

[43] C. Zhang, "Effect of Tempering Temperature on Impact Wear Behavior of 30Cr3Mo2WNi Hot-Working Die Steel," *Structural Materials,* vol. 6, 2019.

[44] T. Mrotzek, A. Hoffmann and U. Martin, "Hardening mechanisms and recrystallization behaviour of several molybdenum alloys," *International Journal of Refractory Metals and Hard Materials,* vol. 24, no. 4, pp. 298-305, 2006.

[45] A. Saxena, A. Kumaraswamy, N. Kotkunde and K. Suresh, "Constitutive modeling of high-temperature flow stress of armor steel in ballistic applications: A comparative study," *Journal of Materials Engineering and Performance,* vol. 20, no. 10, pp. 6505-6513, 2019.

[46] H. Rogers, "Adiabatic plastic deformation," *Annual Review of Materials Science,* vol. 9, no. 1, pp. 283-311, 1979.

[47] B. Yildirim, "Modeling of high velocity impact of spherical particles," *Wear,* vol. 270, no. 9-10, pp. 703-713, 2011.

[48] G. Guruswami, "On the Conversion of Plastic Work into Heat During High Strain Rate Deformation, Shock Compression of Condensed Matter," in *AIP Conference Proceedings*, 2002.

[49] M. Ortiz and J. Molinari, *International Journal of Impact Engineering,* vol. 27, no. 4, pp. 347-358, 2002.

[50] M. Saleh, V. Luzin, M. Kariem and D. Ruan, "Analysis of the Residual Stress in ARMOX 500T Armour Steel and Numerical Study of the Resultant Ballistic Performance," in *Residual Stresses 2016: ICRS-10*, Sydney, 2016.

[51] C. Kang, F. Liu, Z. Jiang, H. Suo, X. Yu, H. Zhang and S. Ding, "Effect of cryogenic treatment on microstructure evolution and mechanical properties of high nitrogen plastic die steel," *Journal of Materials Research and Technology,* vol. 15, pp. 5128-5140, 2021.

[52] L. Han, Y. Wang, . S. Liu, Z. Zhang, . X. Song, Y. Li, . W. Liu, . Z. Yang and . M. Mu , "Effect of cryogenic treatment on the microstructure and mechanical properties of selected laser melted H13 steel," *Journal of Materials Research and Technology,* vol. 21, pp. 5056-5065, 2022.

CHAPTER 3

High Strain Rate Compression with Varying Temperatures on Armox 500T

3.1 Introduction

Armox 500T is a material subject to high strain rate loading including extreme loading conditions such as ballistic impact. A common byproduct of this loading is a high increase in thermal energy which may compromise the integrity of the material. The effects this has on the material and what causes Armox to reach failure are unknown. By taking a systematic loading approach with increasing strain rates at various temperatures and using microstructural analysis to identify damaged regions contributing to failure, the user could tailor the manufacturing and application of the material such that it is most effective and optimal in performance. Furthermore, stress and strain response from the material can aid in high-fidelity FEA and GISSMO modelling as well as material characterization. This method is a different approach than ballistic replicating tests which would give accurate direct performance information such as penetration and shrapnel. These tests lack material characterization and overall response due to limited sensors and sample recovery. For this reason, the Hopkinson Bar approach was chosen.

This study investigated the high temperature and high strain rate compression performance of Armox 500T based on ASTM E209 standards. Using a Direct Hopkinson Pressure Bar (DHPB), a systematic approach of increasing compressive strain rates was applied to cylindrical Electrical Discharge Machining (EDM) cut samples of Armox in various thermal conditions. A stress-strain and quantitative analysis was performed using the obtained data as well as optical and scan electron microscope imaging on the adiabatic shear band and crack propagation regions of the surface microstructure. Lastly, Vickers Hardness tests were performed on these regions of interest to confirm the presence of adiabatic shear bands and high dislocation areas.

3.2 Methodology

In this study, the Armox 500T performance was investigated. EDM cutting was used to create precision-cut cylindrical specimen and impact testing in the high strain rate range was performed using a direct Hopkinson pressure bar to induce localized stress regions. Furthermore, these conditions were amplified by coupling them with high-temperature exposure. Quantitative data was achieved through the use of a strain gauge, characterizing the material through stress-strain curves. The OM and SEM were used to examine and measure regions of interest including cracks, ASBs, and overall microstructural changes.

3.2.1 Compression Specimen

The bulk material which this sample was cut from was a 76 cm x 76 cm x 3 cm rolled slab of Armox 500T as shown in Figure 3-1. The specimen was cut from the face of the slab to maintain consistency. The cutting was performed using a non-conventional machining technique known as Electrical Discharge Machining which has the ability to machine any conductive material and is often used on hard materials [1] [2]. Higher geometrical tolerance can be achieved due to its non-contact interaction with the material and limited vibration. This process also results in a high-quality surface finish and minimal effects on the microstructure of the material [3].

The specimen size is adapted from several studies depicting a length-to-diameter ratio (aspect ratio) close to 1.1 [4] [5] [6]. The importance of a good aspect ratio is that the stress-strain curves produced are dependent on how the specimen deforms during uniaxial compression [4]. If the aspect ratio is high, it may buckle and cause inconsistent data or premature failure. If the aspect ratio is too low, the mechanical limit of the material may be reached without causing plastic deformation. The cylindrical specimen was designed with a 7.00 mm length by 6.33 mm diameter (shown in Figure 3-2) to reflect this. Other authors have used similar aspect ratios to study ASB

microstructural evolution and morphology [7] [8] [9] [10]. The specimen size was reduced by one-third due to the strength and high toughness in Armox, and the limitations of the DHPB which would not be able to fracture the Armox 500T specimen at full size.

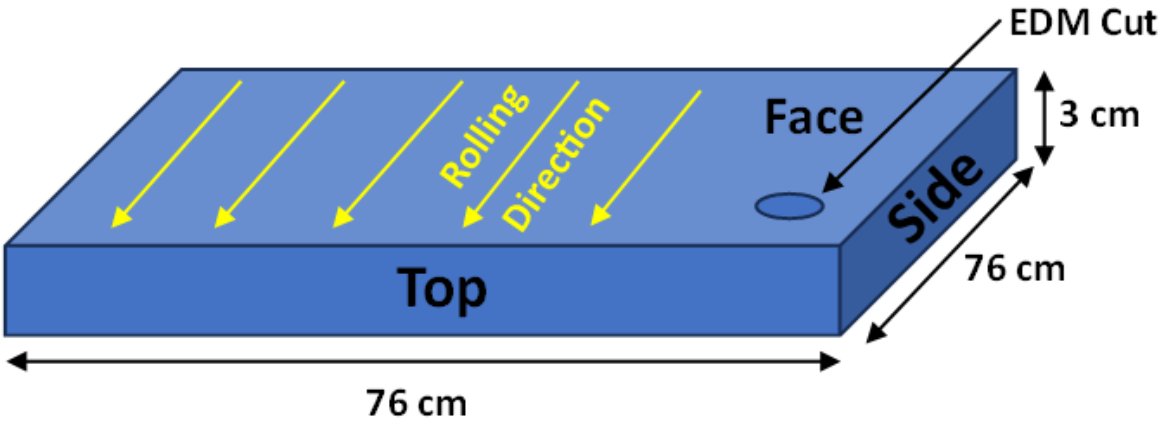

Figure 3-1: As received Armox 500T bulk material size, rolling direction, and EDM cutting surface for compression specimen

The cylindrical specimen shape seen in Figure 3-2 was chosen for several reasons including its uniformity in stress and strain distribution, and limited disruption of wave interactions between the incident, transmitted, and reflected wave data, therefore producing accurate and reliable results [11].

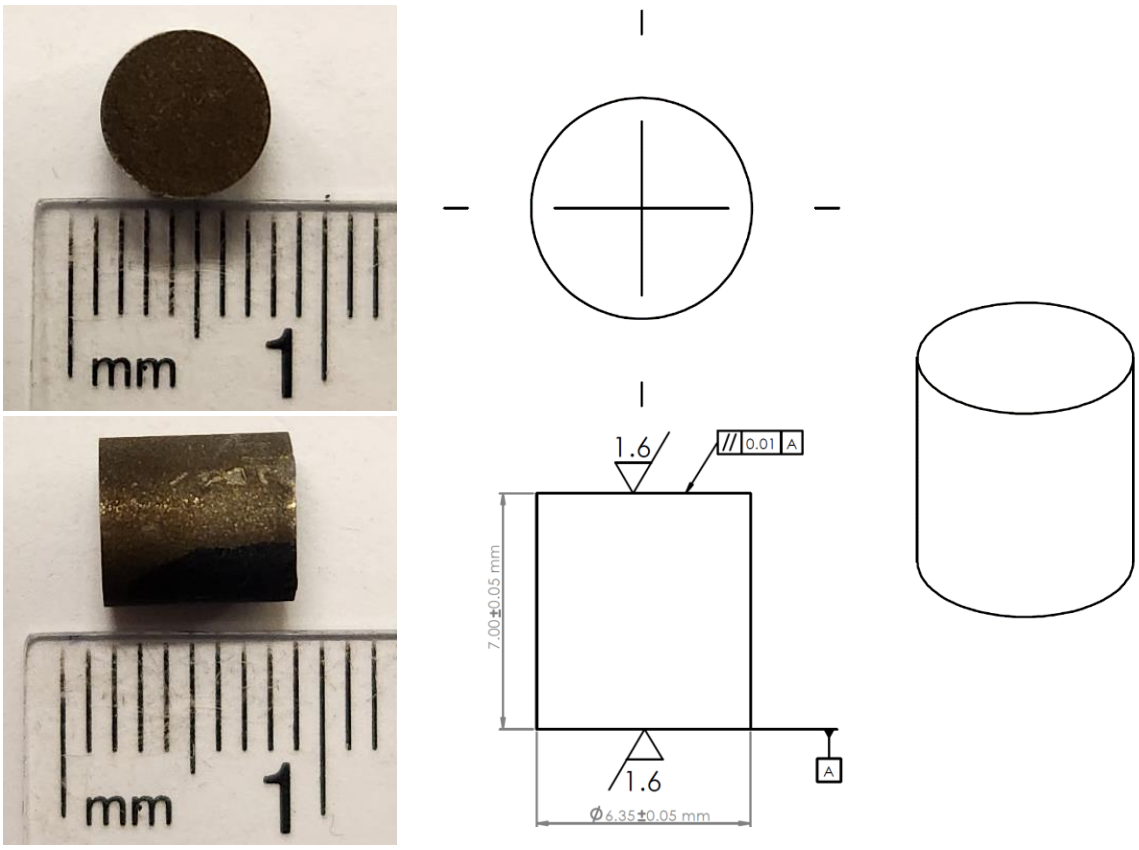

Figure 3-2: Armox Cylindrical Compression Specimen

3.2.2 High Strain-Rate Compression Testing

The rate at which stress is applied can have a significant impact on the material response and behaviour. In quasistatic strain rates, the material is subject to slow and steady loading in which the stresses can be evenly distributed throughout the entire specimen [12]. In high strain rate conditions these stresses can become highly concentrated in particular regions leading to stress collapse, adiabatic shear bands, crack propagation, and ultimately failure. In a controlled test environment, these are commonly induced through the use of a Direct Hopkinson Pressure Bar (DHPB).

3.2.2.1 Direct Hopkinson Pressure Bar

The Direct Hopkinson Pressure Bar (DHPB) is a modified form of the Split Hopkinson Pressure Bar and is used for high strain rate testing [13]. It uses a compressed nitrogen gas tank to release pressure into a pipe which accelerates an impact cylinder (input bar) into the specimen which is set on the transmitter bar with an impact velocity range of around 5-70 m/s [14]. This results in strain rates ranging from 10^3 s^{-1} to $10^4 s^{-1}$ in compression [13]. This piece of equipment is preferred for this series of tests as it produces impact velocities great enough to cause significant plastic deformation, ASBs, and fracture in high-strength materials such as steels.

Although the Hopkinson bar does not fully resemble a direct ballistic impact test, both are methods to study dynamic material response and behaviour. Ballistic impact testing is designed to replicate real-world failure mode, penetration, and deformation. The Hopkinson bar is used as a controlled laboratory apparatus to measure material strain, stress, deformation, and overall material properties which cannot be achieved during live round testing. However, the impact momentum of the projectile at the exit from the Hopkinson bar can be larger than the average 9mm bullet. By comparison, a 9mm ballistic round carries about 13 kg m/s of impact momentum, whereas, the projectile of the Hopkinson bar can reach well over 30 kg m/s due to its large mass being accelerated through a long barrel.

The DHPB is composed of several components including a compressed gas cylinder, incident bar (hollow barrel), projectile, transmitter bar, photodiode timing gates, strain gauge, controls system, and Data Acquisition System (DAQ) which has sampling rate of 125 MHz for 25 MHz data acquisition frequency. A schematic of the DHPB used for this experiment can be seen in Figure 3-3 and Figure 3-4. The initial input and control parameter in this equipment is the amount of pressure being released from the nitrogen gas tank which is controlled with a pressure regulator

and solenoid valve. The solenoid valve is opened when it is energized and is closed when de-energized using a spring which closes the valve [15]. The control system part of this equipment allows the user to dictate when pressure is released through the use of “power up” and “fire” switches. The first switch primes the system with energy, while the second signals the valve to open, respectively. Once the valve is open, the 1.36kg AISI 4340 steel projectile is accelerated a distance of 1.2 m through the hollow indecent bar towards the exit of the barrel. Two photodiode timing gates are placed at the exit of the barrel at a predetermined distance of 25 cm to measure the time it takes to pass each of the gates. Using the distance and time, the final velocity of the projectile before impact can be calculated. The projectile would then impact the sample placed on the face of the transmitter bar, plastically deforming the sample and producing elastic strain in the transmitter bar, which is measured by a strain gauge. The strain gauge produces voltage-time data and is amplified through the Wheatstone bridge and read by the DAQ linked to a computer.

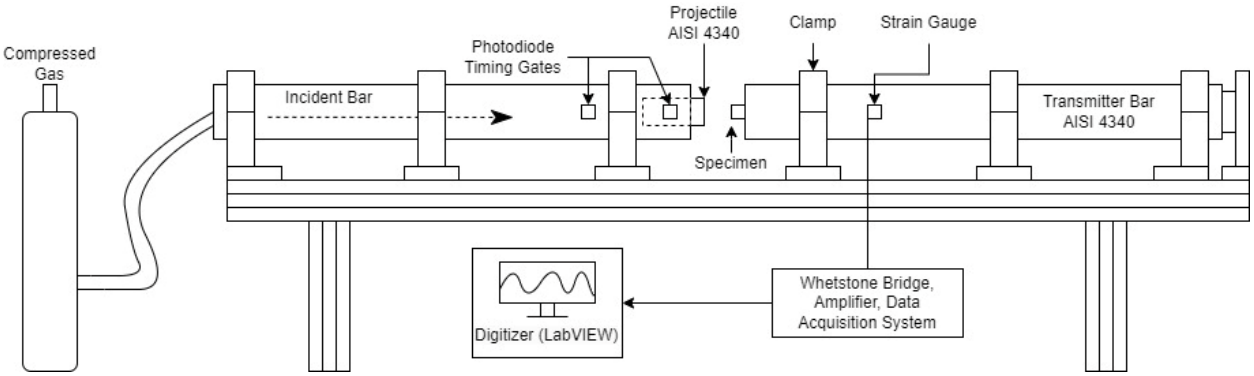

Figure 3-3: Direct Hopkinson Pressure Bar Diagram

Figure 3-4: Direct Hopkinson Pressure Bar setup

3.2.2.2 High Strain Rate Compression Test Procedure

The impact procedure first involves securing the specimen to the center of the face of the transmitter bar. This includes the use of a thin steel wire to assist the specimen in remaining in an upright position without falling as seen in Figure 3-5. It also includes the use of a viscous gel placed on each flat end of the specimen which reduces friction between the impact bar, specimen, and transmitter bar surfaces, ensuring a more uniform specimen deformation [16]. The use of the steel wire was strictly to hold the specimen upright and flat in the center of the bar. This was particularly necessary for high temperature testing which would melt off the viscous gel and cause it to fall. The hardness of the heat-treated projectile and transmitter bar were measured to be 59 Rockwell hardness (HRC) compared to the Armox which has a hardness of 55 HRC [17]. This prevents the projectile and transmitter bar from plastically deforming or having its surface damaged to produce inaccurate signals and data. This signal is produced when the gas pressure of 15 Psi (gage pressure) is released through the incident bar and the projectile is fired, impacting the specimen. This produces a compressive pulse in which elastic waves proceed through the specimen into the transmitter bar where a strain gauge is attached to measure this data. The impact procedure was repeated 2 more times, totalling 3 specimens. The input pressure was then increased by 2-5 Psi (gage pressure) and the process was repeated for the next set of specimens until failure was

consistently reached, indicating the limit of Armox to withstand the impact energy. The test matrix can be seen below in Table 3.2-1.

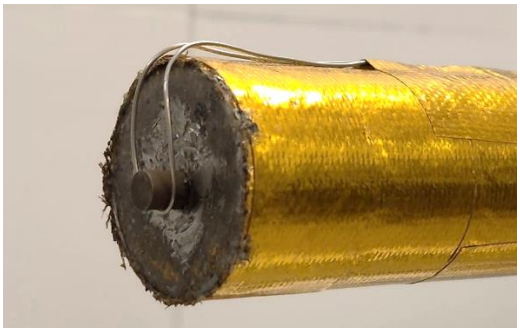

Figure 3-5: Thin steel wire assisting specimen position

Name of Specimen Name of Specimen Set (3 repeated tests per set)	Temperature at time of impact (°C)	Input pressure (Psi)
RT1-A-C	23°C	15
RT2-A-C	23°C	17
RT3-A-C	23°C	21
RT4-A-C	23°C	25
RT5-A-C	23°C	30
RT6-A-C	23°C	35
RT7-A-C	23°C	40
RT8-A-C	23°C	45
RT9-A-C	23°C	50
RT10-A-C	23°C	55

Table 3.2-1: High strain-rate compression room temperature testing matrix

3.2.2.3 Impact Data

The transmitter bar is fitted with strain gauges which enables the DAQ to read a voltage-time plot. This along with a calibration procedure, a force time plot can be created [18]. These values as well as specimen dimensions can be inputted into the following equations to create a stress strain curve using Equation 3.2-1 - Equation 3.2-3.

Under the assumption that there is a constant strain rate and a linear variation of displacement with time, the following formulations can be used derived from ASTM E209 [16]:

$$\sigma_t(t) = \left(\frac{f(t)}{A_0}\right)\left(\frac{l_i - (l_i - l_f)\left(\frac{t_i}{t_f}\right)}{l_i}\right) \qquad \textit{Equation 3.2-1}$$

$$\varepsilon_t = \ln\left(\frac{l_i}{l_i - (l_i - l_f)\left(\frac{t_i}{t_f}\right)}\right) \qquad \textit{Equation 3.2-2}$$

$$\dot{\varepsilon} = \frac{C}{2l}\varepsilon \qquad \textit{Equation 3.2-3}$$

Where:

σ_t = True stress

ε_t = True strain

t_i = Initial time

t_f = Final time

l_i = Initial length

l_f = Final length

A_0 = Cross-sectional area of the specimen

C = Longitudinal wave propagation velocity in transmitter bar for AISI 4340

L = Length of the striker bar

ε = Maximum strain

f(t) = Dynamic load as a function of time on the sample

3.2.3 High Strain-Rate High-Temperature Compression Testing

For high-temperature testing, a similar process was completed with the same series of input pressures. To ensure the specimen reached the implied temperature, the specimen was secured to the transmitter bar, soaked in the furnace air temperature for 150 seconds before being impacted, and removed from the environment. This procedure was carried out for 200°C, 300°C, and 400°C. The purpose of the 150-second heat soaking period is for two main reasons. Firstly, the specimen needs to heat up to the intended environmental temperature prior to being impacted. This time is

ensured to be true based on the calculations done in Equation 3.2-4 - Equation 3.2-7 below [19]. Secondly, even though the time required for the specimen to heat up to temperature may be short, the impact procedure to ensure a safe and repeatable impact takes longer. 150 seconds warrants enough time for this procedure to take place and have a consistent soaking temperature for every test.

Givens:

h_{air} = 80 W/m^{2}K [19]
$k_{\text{high carbon steel}}$ = 58 W/m-k [19]
$c_{\text{p Armox 500T}}$ = 455 Jkg^{-1} K^{-1} [20]
ρ_{Armox} = 7800 kg/m^3
T_i = 23°C
T_∞ = 100, 200, 300°C
T_0 = 0.95* T_∞
m_{Armox} = 0.0017 kg
$A_{\text{Surface (convection)}}$ = 0.0001692 m^2
$A_{\text{Surface (conduction)}}$ = 0.00003117 m^2
$L_{\text{(Length of Armox)}}$ = 0.007 m
$L_{c\text{ (Diameter of Armox)}}$ = 0.0004286 m
$r_{0\text{ (Radius of Armox)}}$ = 0.0032 m

$$\textbf{Biot Number} = \frac{hr_0}{k} \qquad \textit{Equation 3.2-4}$$

$$\textbf{Biot Number} = 0.0087$$

Therefore,

A_1 = 1.0025 [19]
λ_1 = 0.1412 [19]

The Biot number is defined as the ratio between external heat transfer resistance and internal heat transfer resistance and a ratio of less than 0.1 indicates that the internal conduction resistance is significantly smaller than the surface convection [21]. This is a method to prove that the system`s temperature gradient can be neglected due to its minor effect on the overall heat transfer. In this

case, it is a result of the specimen being small. Therefore, with a Biot number of 0.0087, it can be assumed that there is constant temperature from the surface throughout the entire material.

The predominant method of heat transfer to the specimen is convection, as illustrated in Figure 3-6. The energy from the furnace provides convective heat transfer to the surfaces of the specimen placed inside the heated system. This method of heat transfer was used to calculate the amount of time it takes for the specimen to reach the implied temperature seen in Equation 3.2-5 - Equation 3.2-7.

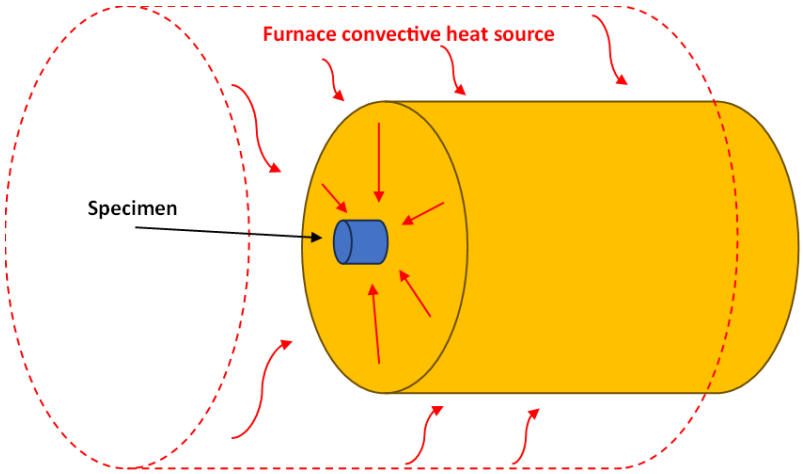

Figure 3-6: Heat transfer to specimen

$\alpha = \frac{k}{\rho * c_p}$	*Equation 3.2-5*	α = 1.634263*10^{-5}
$\frac{T_0 - T_\infty}{T_i - T_\infty} = A_1 e^{-\lambda_1^2 \tau}$	*Equation 3.2-6*	$\tau_{200°C}$ = 144.1292
		$\tau_{300°C}$ = 146.256
		$\tau_{400°C}$ = 147.2865
$\tau = \frac{\alpha * t}{r_0^2}$	*Equation 3.2-7*	**$t_{200°C}$ = 87.5087 seconds**
		$t_{300°C}$ = 88.8 seconds
		$t_{400°C}$ = 89.4256 seconds

In this testing apparatus, instruments and parts were added to have the ability to test under high-temperature conditions. The heating source mounted around the end of the bar was a 90 mm (inside diameter), 1200-watt, Jinbaihe Ceramic Band Heater capable of outputting temperatures of 800°C-1000°C as seen in Figure 3-7.

The furnace temperature was controlled, set, and measured by a Digi-Sense TC5000 Benchtop PID Temperature Controller receiving feedback from a Digi-Sense High-Temperature Wire Probes - Fiberglass Insulated thermocouple placed close to the specimen that was secured on the transmitter bar. Once calibrated, the set temperature fluctuated by ±5°C.

To protect the bar and instruments and prevent inaccurate readings, layers of reflective aluminum foil heat shield tape and fire-resistant thermal insulation (Geesic ceramic fibre blanket fireproof insulation baffle 1 inch thick) were used. This reduced the amount of heat exposure to the components as seen in Figure 3-7. This also reduced the natural convection air movement through the furnace, allowing the temperature to hold more consistently as well as allowing the temperature to be raised much higher.

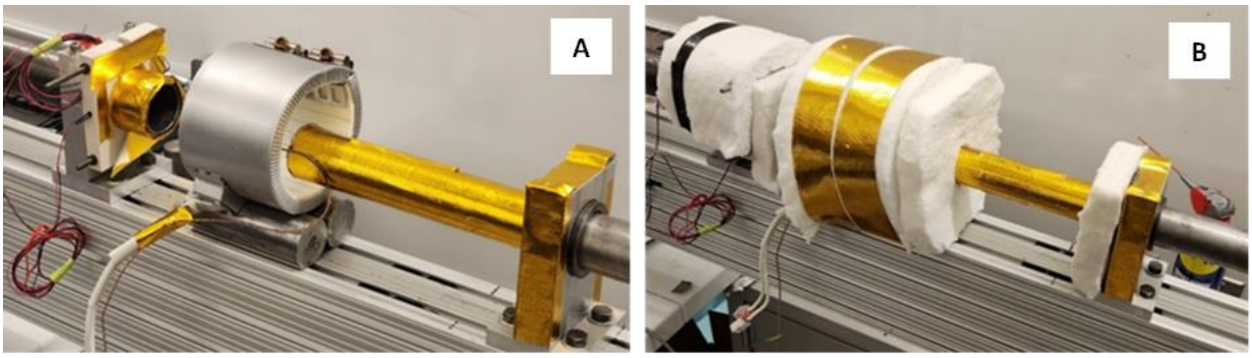

Figure 3-7: Uninsulated and unsecured furnace apparatus on Hopkinson Bar (A), Insulated furnace apparatus on Hopkinson Bar (B)

The test matrix for the higher temperature series is similar to the room temperature test procedure as three specimen were impacted at each input pressure, increasing until failure was consistently achieved. This same procedure was repeated for the 300°C and 400°C samples. This test matrix can be seen in detail below in Table 3.2-2.

Name of Specimen Set (3 repeated tests per set)	Temperature at time of impact	Specimen time in furnace before impact (s)	Input Pressure (Psi)
T200-A-C	200°C	150	15
T200-D-F	200°C	150	17
T200-G-I	200°C	150	21
T200-J-L	200°C	150	25
T200-M-O	200°C	150	30
T200-P-R	200°C	150	35
T200-S-U	200°C	150	40
T200-V-X	200°C	150	45
T200-Y-ZA	200°C	150	50
T200-ZB-ZD	200°C	150	55

Table 3.2-2: High strain-rate high-temperature compression testing matrix

3.3 Results and Discussion

120 Samples were tested under increasing strain rate and temperature conditions until complete failure was reached. These temperatures included room temperature, 200°C, 300°C, 400°C. The data received from the Hopkinson Bar was used to create stress-strain curves and various other comparative charts. Optical microscopic and scan electron microscope imaging were then used to complete a microstructural analysis of the surface of post-impacted samples with increasing strain rate and temperature exposures. Finally, microhardness tests were performed on these surfaces to distinguish unaffected regions and adiabatic shear band regions with high dislocation density.

3.3.1 High Strain-Rate Compression Stress-Strain Curves

A standardized method of measuring material behaviour is the use of a stress-strain curve. The curves demonstrate essential properties including the material`s elastic region, plastic region, toughness, and yield point.

For each of the temperature exposures, consistent results reflected the gradual increase in true strain, peak stress, and toughness as shown in Figure 3-8 - Figure 3-11. However, comparing each of the temperature ranges, it was seen that at 200°C, many of these properties were seen to be enhanced, whereas, at 300°C and 400°C, the peak stress response to each impact was 11.08% and 18.16% lower respectively. Overall, the peak stress was highest at 200°C along with the largest amount of strain without fracture (0.359 strain).

Evidence of nano-twinning within the ASB has been seen in other studies of Armox 500T, which would explain and justify many of the stress-strain curves having more than one maximum stress point [7]. Nano-twinning is a deformation mechanism in which the material forms twin boundaries within the crystal structure which is common among some metals and alloy materials under high strain rate deformation [22]. This can cause the material to undergo several phenomena including stress relaxation after the initial hardening period and a secondary hardening mechanism as the dislocation density increases.

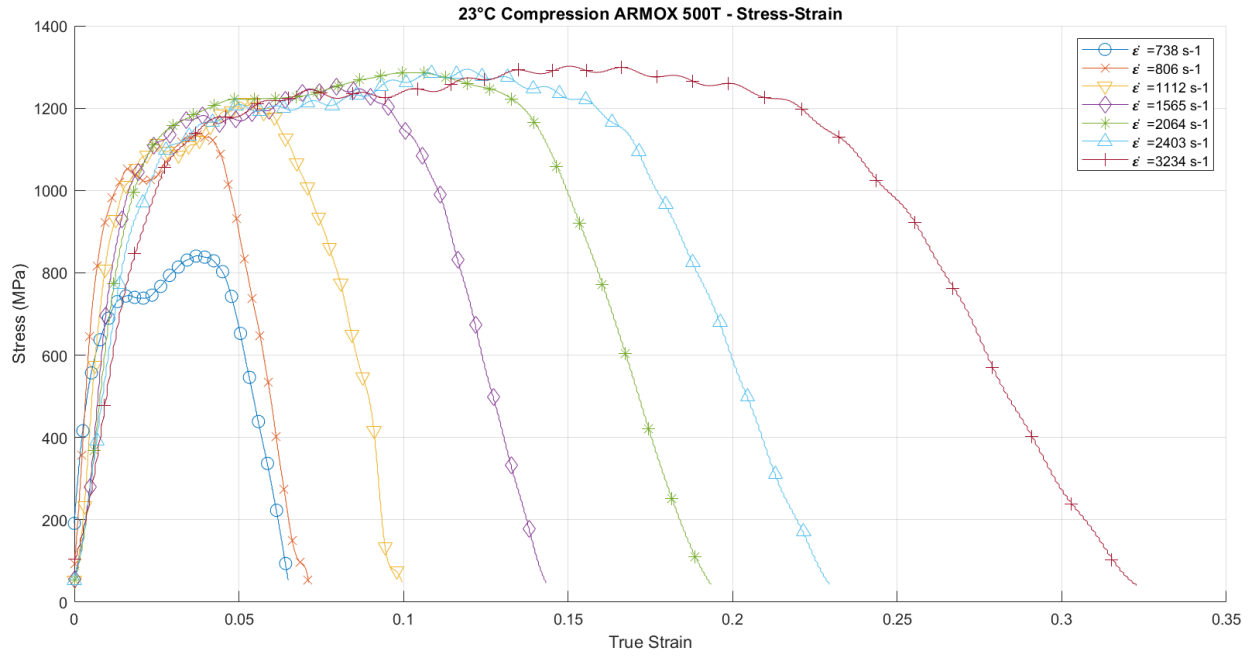

Figure 3-8: Room temperature impact stress-strain response for samples RT1-A, RT2-B, RT3-A, RT4-A, RT7-B, RT8-B, and RT9-B

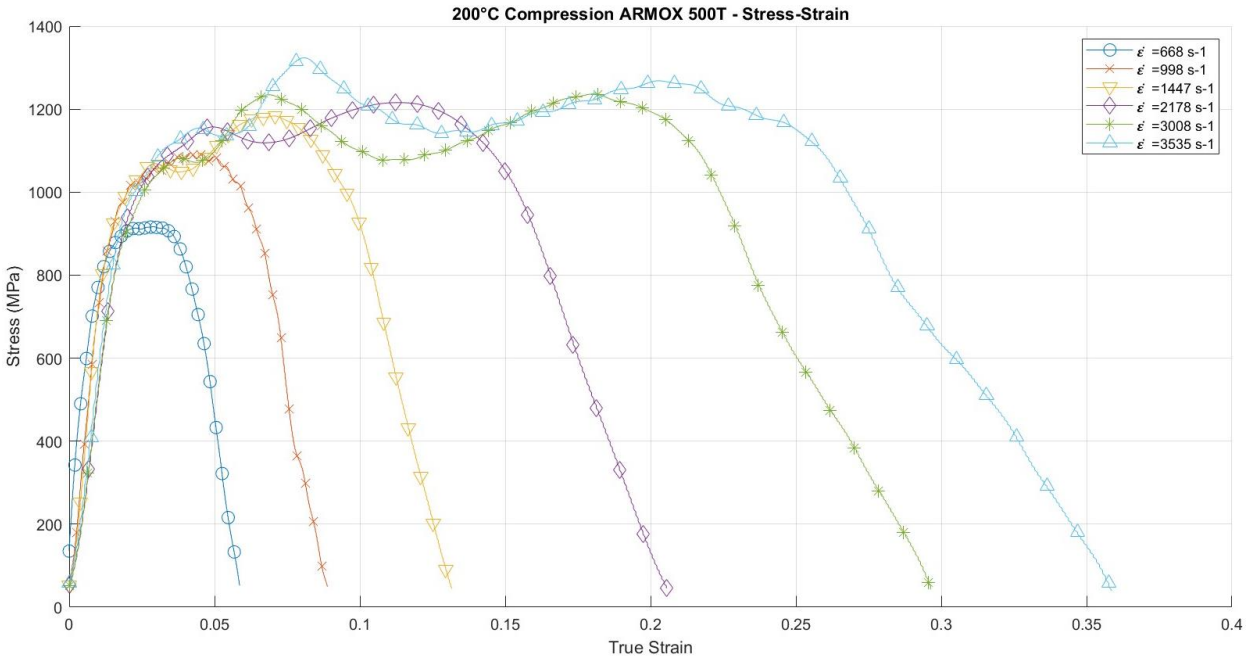

Figure 3-9: 200°C temperature impact stress-strain response for samples T200-A, T200-E, T200-K, T200-R, T200-W, and T200-ZC

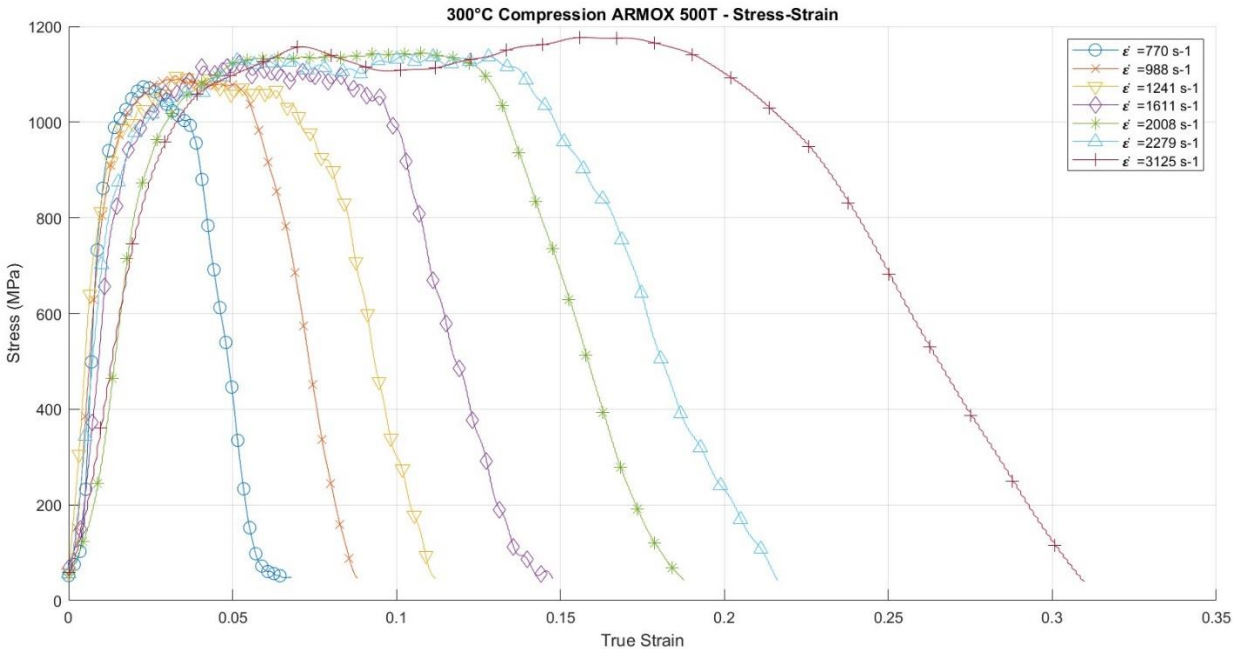

Figure 3-10: 300°C temperature impact stress-strain response for samples T300-B, T300-E, T300-G, T300-K, T300-M, T300-P, and T300-W

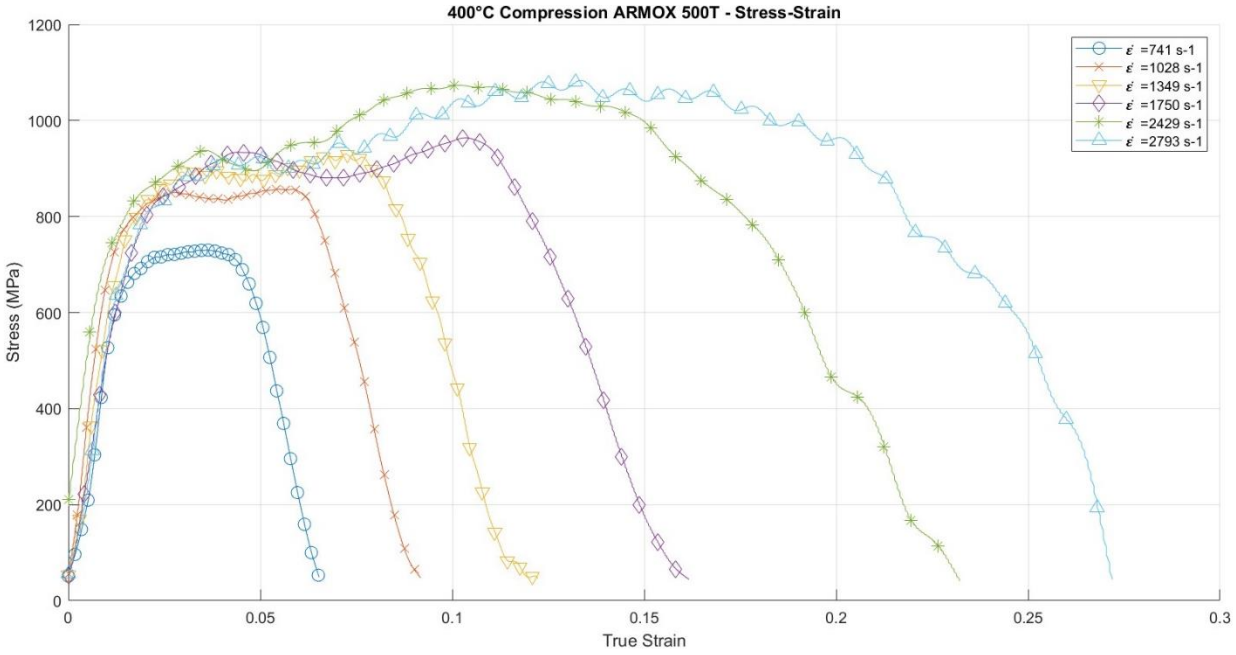

Figure 3-11: 400°C temperature impact stress-strain response for samples T400-A, T400-E, T400-F, T400-I, T400-S, and T400-U

Figure 3-12 and Table 3.3-1 demonstrate the repeatability of the testing conducted in this chapter. Three tests were conducted for each input pressure according to the test matrix. However, in the case of noisy, outlier, or equipment fault data, an additional test was conducted to replace it.

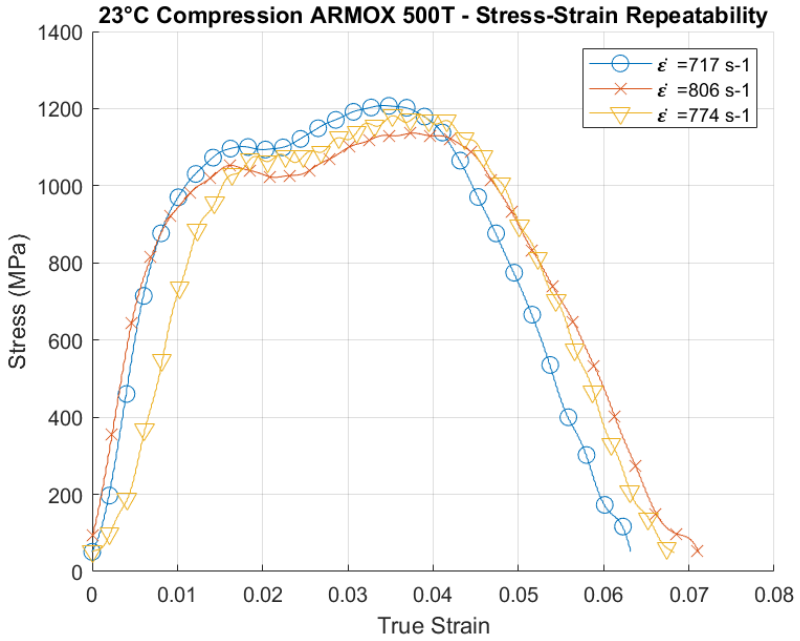

Figure 3-12: Stress-strain data for three repeated tests at room temperature 17 psi (samples RT2-A, RT2-B, and RT2-C)

Sample	Impact Momentum (kg m/s)	Axial Compression (mm)	Toughness (Jm^{-3})	Maximum Stress (MPa)	Maximum Strain	Strain at Ultimate Stress
RT2-A	11.83	0.43	54.24	1208.1	0.063	0.0342
RT2-B	12.24	0.48	57.89	1136.7	0.084	0.0377
RT2-C	12.18	0.46	54.12	1184.7	0.071	0.0384
Average	**12.08**	**0.457**	**55.42**	**1176.5**	**0.073**	**0.0368**
Standard Deviation	**0.179**	**0.021**	**1.75**	**29.72**	**0.008**	**0.0018**

Table 3.3-1: Average and standard deviation of data for three repeated tests at room temperature 17 psi (samples RT2-A, RT2-B, and RT2-C)

3.3.2 High Strain-Rate Compression Deformation Comparison

The following Figure 3-13 can be used as a reference to better understand the increasing compression deformation effects on the specimen shape and size. This displays a comparison of the compressive deformation for each input pressure. It was seen that at 200°C and higher, the specimen consistently sustained higher deformation than at room temperature. However, at 200°C, the sample was able to withstand a larger impact momentum and higher strain rate before resulting in fracture.

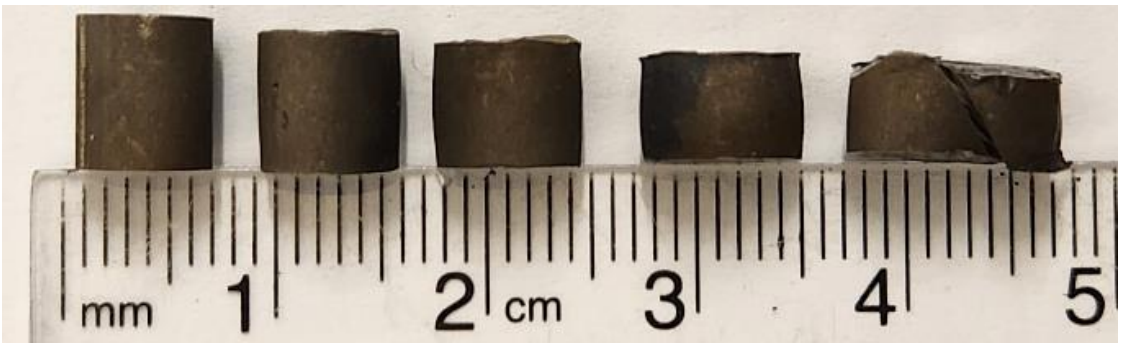

Figure 3-13: Room temperature sample strain progression (Samples: As-Received, RT1-A, RT5-A, RT9-B, and RT10-C respectively)

The following Figure 3-14 - Figure 3-17 demonstrate an overall performance comparison across the various temperatures and impacts. The 200°C samples were shown to be the most superior in all criteria. Figure 3-14 demonstrates the impact momentum and strain rate response from each test where the 200°C samples were able to withstand higher impact momentum and strain rates than the room temperature samples. The 300°C samples performed similarly to this trend, however, fractured at a lower impact momentum and strain rate than both the 200°C and room temperature samples. The 400°C samples responded with a very high strain rate response to the impacts and lower energy was required for failure to be reached, indicating thermal softening effects. Similar results were seen when comparing major axis strain in Figure 3-15 and toughness in Figure 3-16.

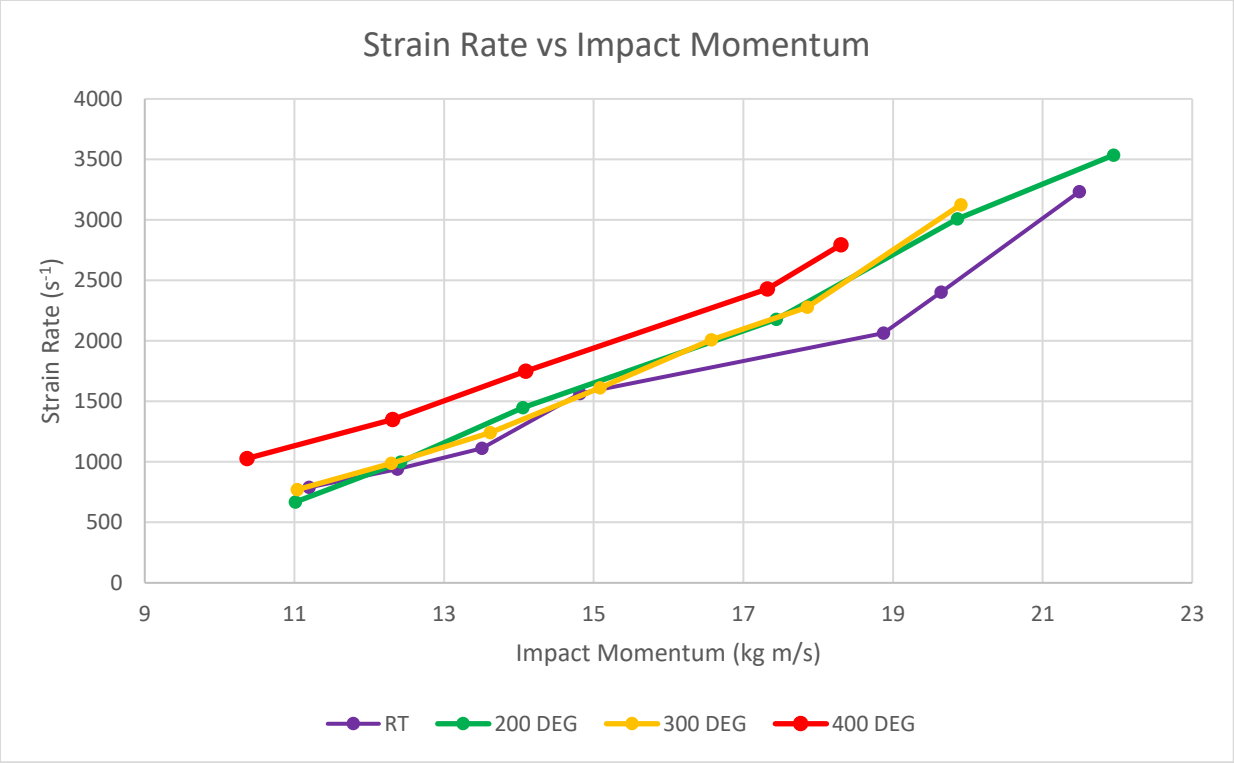

Figure 3-14: Strain rate vs impact momentum for room temperature, 200°C, 300°C, and 400°C samples

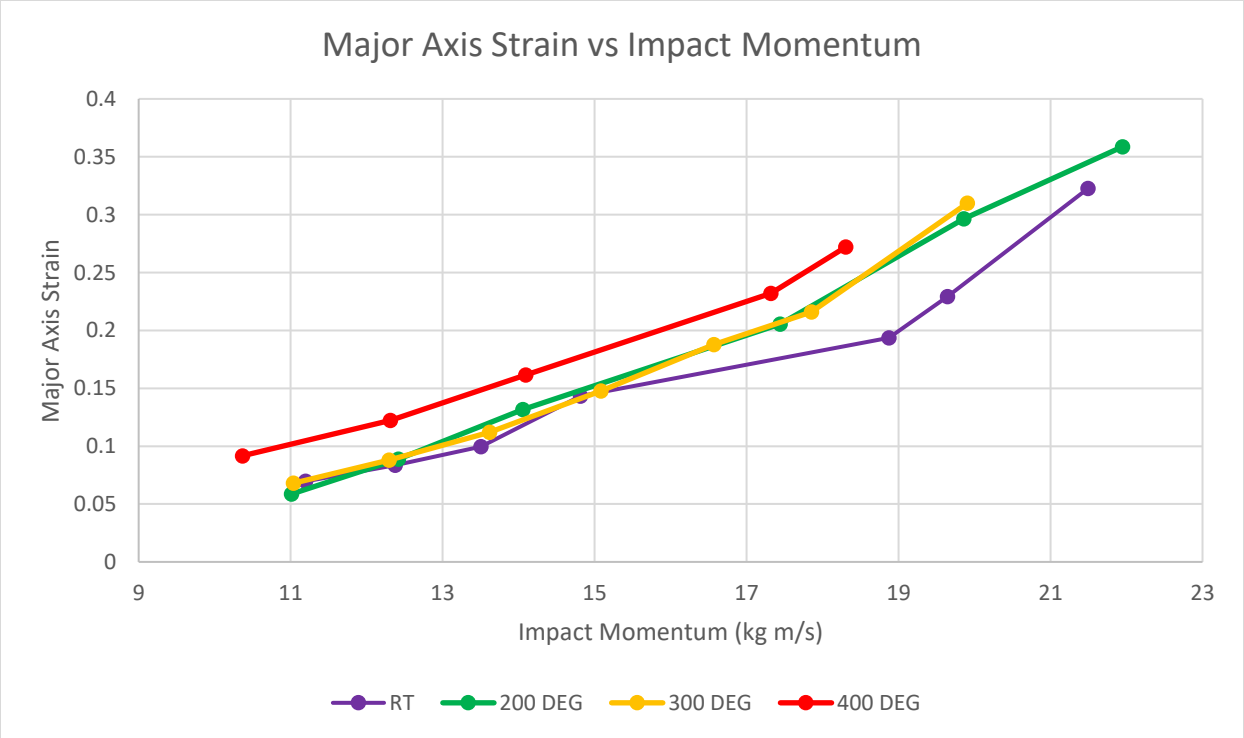

Figure 3-15: Major axis strain vs impact momentum for room temperature, 200°C, 300°C, and 400°C samples

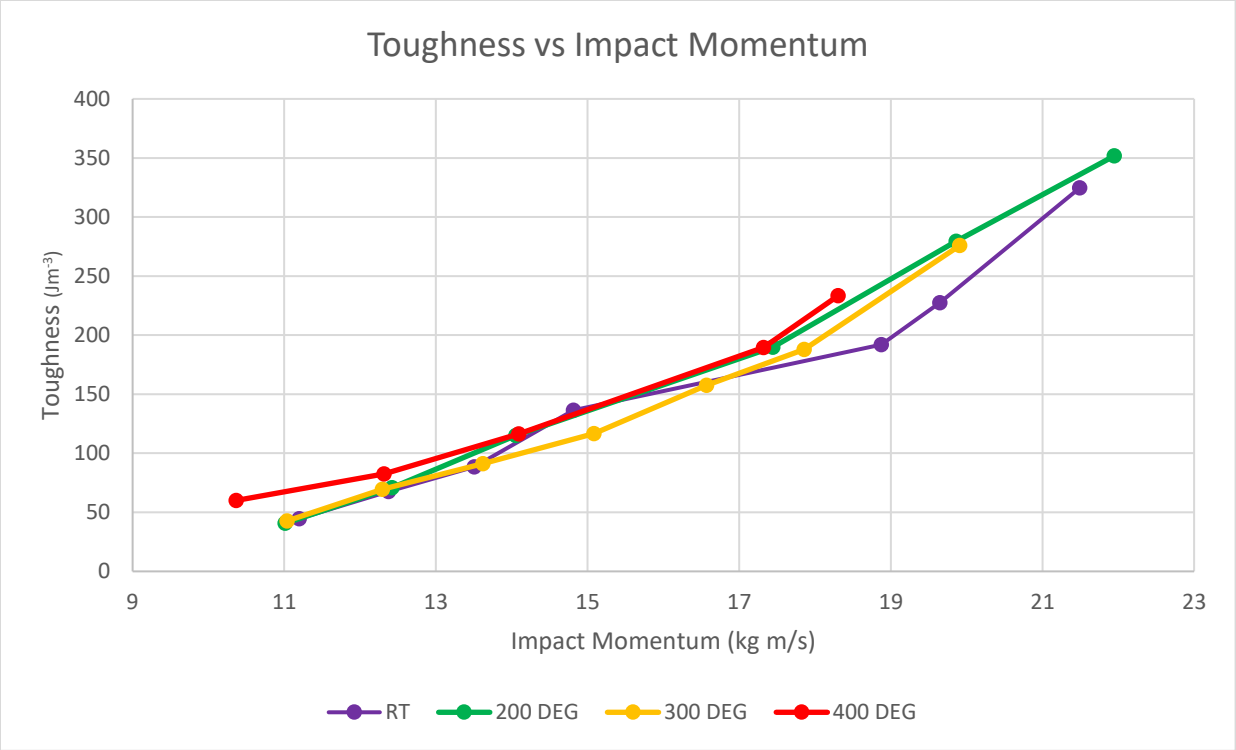

Figure 3-16: Toughness vs Impact Momentum for room temperature, 200°C, 300°C, and 400°C samples

As the impact momentum increases during high strain rate compression, the ultimate stress the material experiences can be significantly affected. This includes strain rate sensitivity due to the material's mechanical properties being exploited by means of strain hardening. By adding temperature into the study, the effects of thermal softening can be seen in contrast across various strain rates and temperatures in Figure 3-17. At room temperature and 200°C, the ultimate stress significantly rises as the impact momentum is increased, whereas, at 300°C and 400°C, it resulted in a linear trend. This is due to the hardenability and work hardening decreasing with elevated temperatures, confirming negative microstructural effects under these loading conditions.

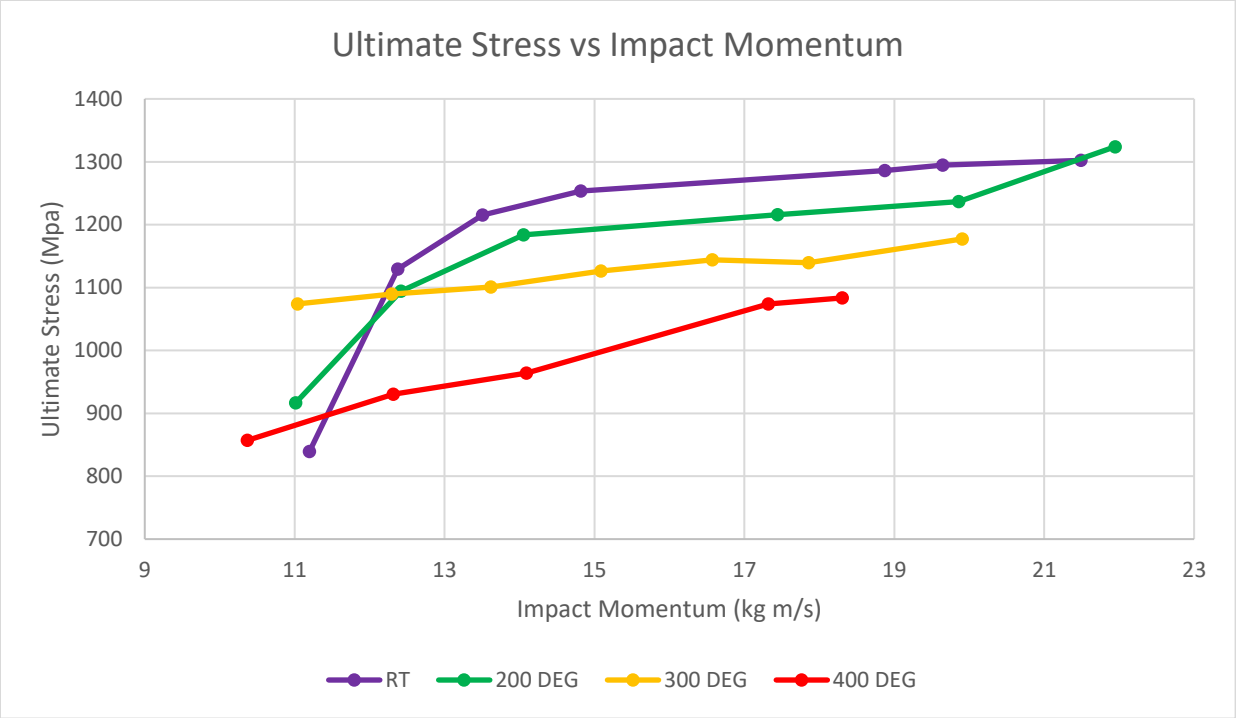

Figure 3-17: Ultimate Stress vs Impact Momentum for room temperature, 200°C, 300°C, and 400°C samples

3.3.3 Microscope Imaging

A standard optical microscope will help identify general adiabatic shear band regions and grain distortion areas using photons or light energy that can be further analyzed by deeper investigative methods if required. Deeper investigative methods include scan electron microscope imaging which will help provide information about the topography, grain structure, and other microstructural features of the material further than the optical microscope by using electrons which have a shorter wavelength and higher magnification.

3.3.3.1 Sample Preparation

Before these samples can be imaged for study, they must be prepared through the process of mounting, grinding, polishing, and etching. The mounting phase consisted of a cold mounted technique using Metlab Jetset Epoxy Resin and Hardener such that the impacted faces of the samples were exposed and mounted in Metlab 1.25-inch diameter reusable cylindrical plastic moulds as shown in Figure 3-18 and Figure 3-19. One sample from each set of input pressures was selected to be mounted including fractured samples and as-received, unimpacted samples. The fractured samples were mounted in such a way that the corner of the face where the fracture took place is exposed and visible as seen in Figure 3-20 and Figure 3-21.

The samples were then grinded down using Metlab 8-inch wet silicon carbide C weight abrasive grinding disks in a sequence of increasing grits including 400 grit, 600 grit, 800 grit, and 1200 grit. In the next stage, the samples were polished on a Metlab 8-inch short synthetic rayon fibre pad with a Metlab 0.05 µm Alumina suspension (Gamma B). The surfaces of these samples were then etched using 2% Nital etchant from ES Laboratory LLC. This increases the contrast in the surface microstructure of the specimen and identifies any changes. 1 ml of this etchant was applied to the surface of each sample using a dropper for 20 seconds before being washed with distilled water and dried with compressed air.

Figure 3-18: Images demonstrating which impacted surface was mounted for grinding, polishing, and imaging

Figure 3-19: Images demonstrating the impacted mounted surface for grinding, polishing, and imaging

3.3.3.2 Fractured Sample Preparation

Figure 3-20: Images demonstrating which fractured corners were mounted for grinding, polishing, and imaging

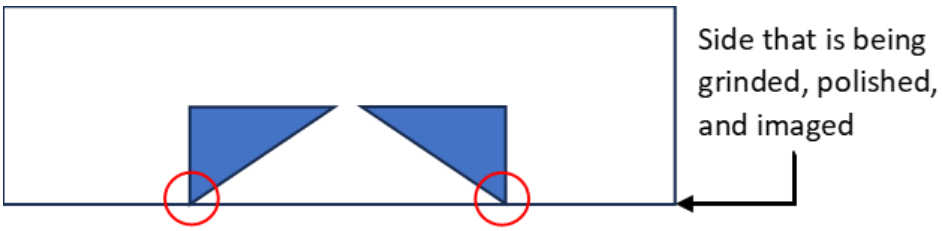

Figure 3-21: Images demonstrating how the fractured corners were mounted for grinding, polishing, and imaging

In preparation for the SEM images, these mounted samples were coated with pure platinum in an argon atmosphere. This aids in providing a highly conductive surface to allow to grounding of electrons and energy dissipation, ensuring higher-quality images. Additionally, carbon tape was connected to the surface of the material as redundancy to confirm quality contact with the grounding surface.

3.3.3.3 Optical Microscope Imaging: Original As-Received Armox

The optical microscope images of the stock manufactured Armox at 100x and 400x magnification as seen in Figure 3-22 reveal the well-balanced, quenched, annealed, martensitic, high-carbon steel structure with the appearance of a lathed microstructure. This represents the BCT structure resulting from the addition of carbon at high temperatures mixed proportionally throughout the material and quenching the material before the carbon and other elements would have enough time to diffuse out the material matrix. The lathes in this microstructure are grouped in what are called packets where a number of lathes are oriented parallel to each other overlapping with other packets of differing directions of lathes. In other steel or even aluminum microstructures, the grain boundaries are well-defined and targeted as areas susceptible to crack initiation and failure due to their low energy resistance. The randomized packet orientation with overlapping grain boundaries is what gives this particular material the unique characteristic of being heavily resistive to crack initiation in particular regions of the microstructure.

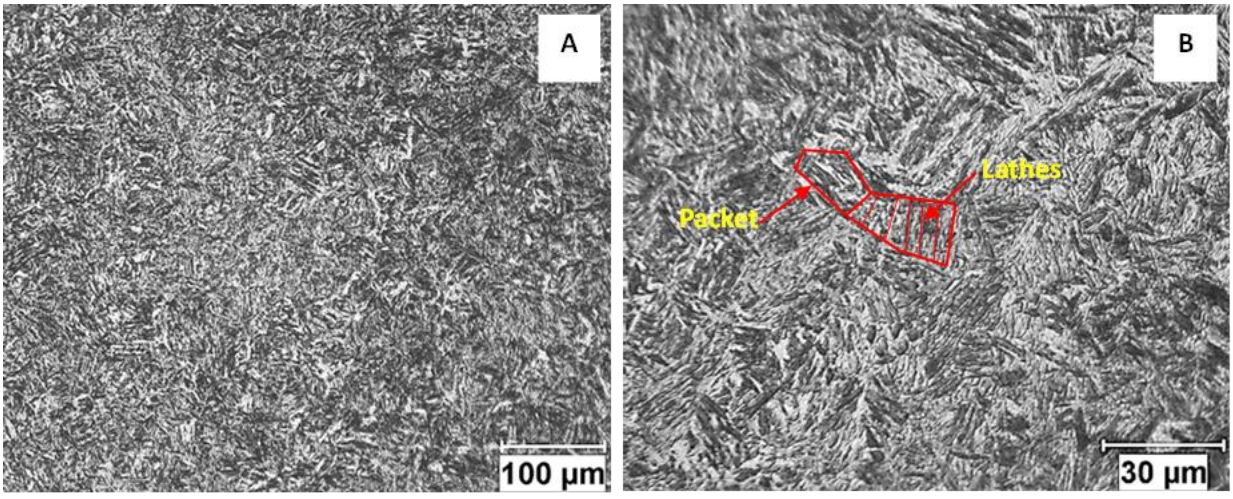

Figure 3-22: OM image of Armox as received 100x (A) and 400x (B) magnification

3.3.3.4 SEM Original As-Received Armox

In the figure below, the microstructure and packets of lathes formed in randomly oriented directions in the as-received sample can be observed much closer than the OM images. The microstructure still demonstrates distinct grains along with its boundaries roughly 10 µm in length. These images depict no impurities, defects, voids, precipitates, or any directional properties in the grain structure.

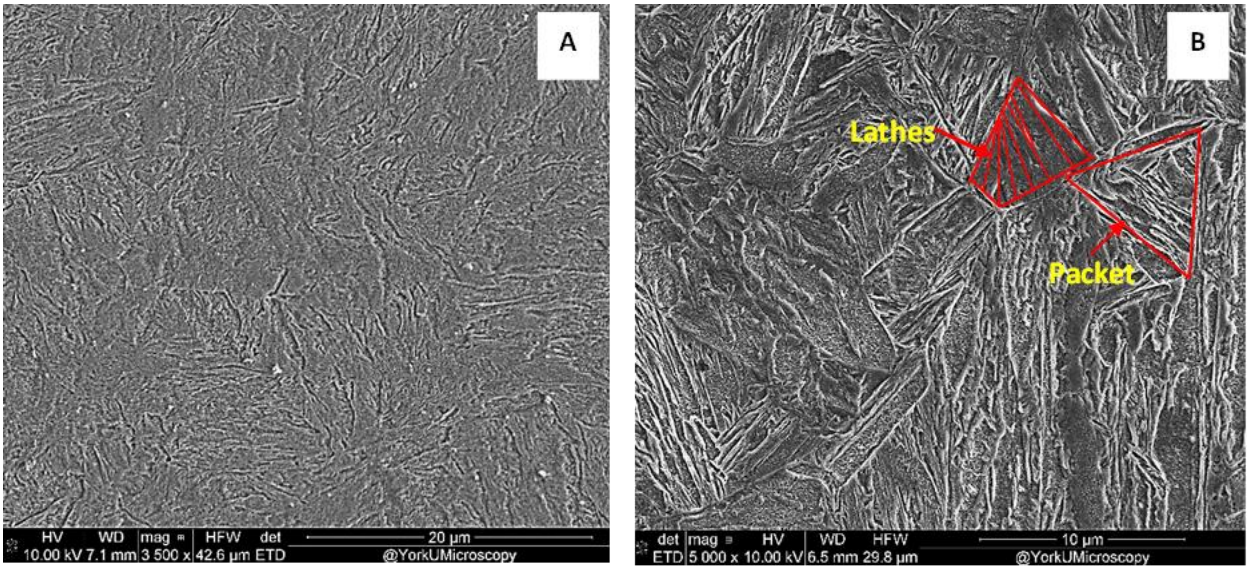

Figure 3-23: SEM imaging of the original as-received microstructure of Armox at 3500x (A) and 6500x (B) magnification

3.3.4 Impact Effects on Armox 500T

As the compression forces on a compression test specimen are increased, deformation, dislocations, and high-energy regions are produced commonly referred to as ASBs are created. This microstructural effect and production of ASBs as well as crack initiation leading up to failure can often be viewed from the impacted surface of the specimen.

3.3.4.1 Microscope Imaging: High Strain-Rate Compression Testing (Room Temperature)

In room temperature conditions, the microstructure of Armox is still in its tough high-strength state as it was received. This unique and uniform matrix of elements makes it difficult for forces to interrupt the microstructure and cause failure. The center of the specimen for all of the room temperature impacted specimen remained unaffected as the deformation of the material was closer to the edges of the sample.

Recognizable changes to the surface microstructure were not noticed until an impact momentum of 18.88 kg m/s was applied to the specimen. In the center of this sample, packets of lathes were observed similar to the as-received sample as an unaffected region under an optical microscope as seen in Figure 3-24. However, closer to the edge of the specimen, it was noticed that the size of these packets and lathes were enlarged. Figure 3-24 shows SEM imaging of the RT7-B sample and makes it apparent that the grain sizes are larger close to the edge of the sample. Comparing the two images of the surface both near the edge of the sample and away from the edge shown in Figure 3-24 (C) and Figure 3-24 (D) respectively, at 20000x magnification, the lathes in the deformed edge region are around 10 μm - 20 μm in length, whereas the lathes in the undeformed region are less than 10 μm in length. This demonstrates that the dislocation density, impact energy, and possible ASB regions will be present near the edge of the sample in higher impact momentum.

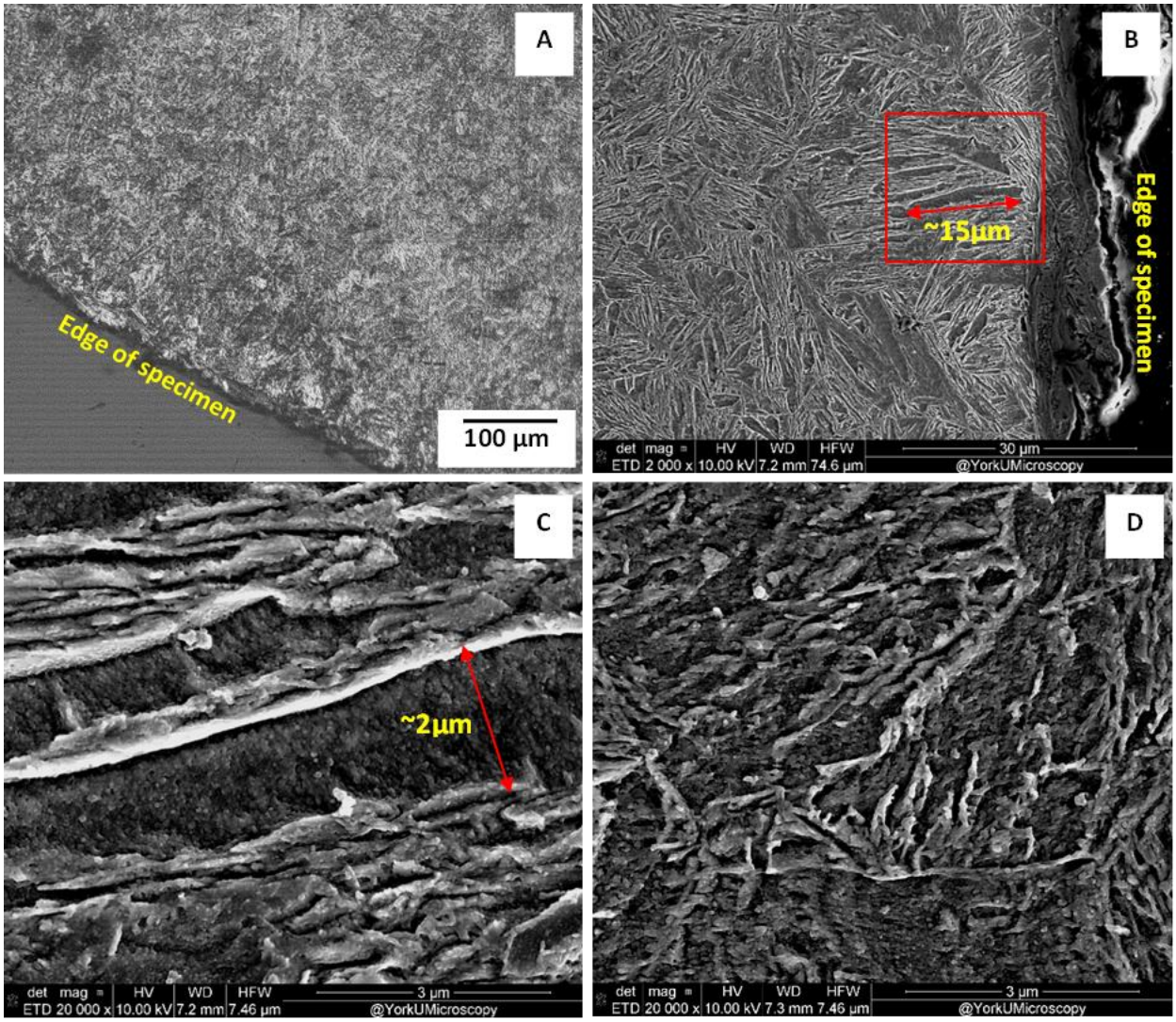

Figure 3-24: Sample RT7-B Room temperature with impact momentum 18.88 kg m/s OM image of sample edge at 100x (A), SEM image of sample edge at 5000x magnification (B), SEM image at 20000x magnification showing deformed grains near the edge of the sample (C), SEM image at 20000x magnification showing deformed grains away from the edge of the sample (D)

With higher-impact momentums being introduced, the specimen begins to show significant changes in the microstructure. In sample RT8-B at 19.64 kg m/s of impact momentum, the microstructure at 150-300 µm from the edge of the surface demonstrated concentrated stress regions with significant deformation, representing the presence of adiabatic shear bands seen in Figure 3-25.

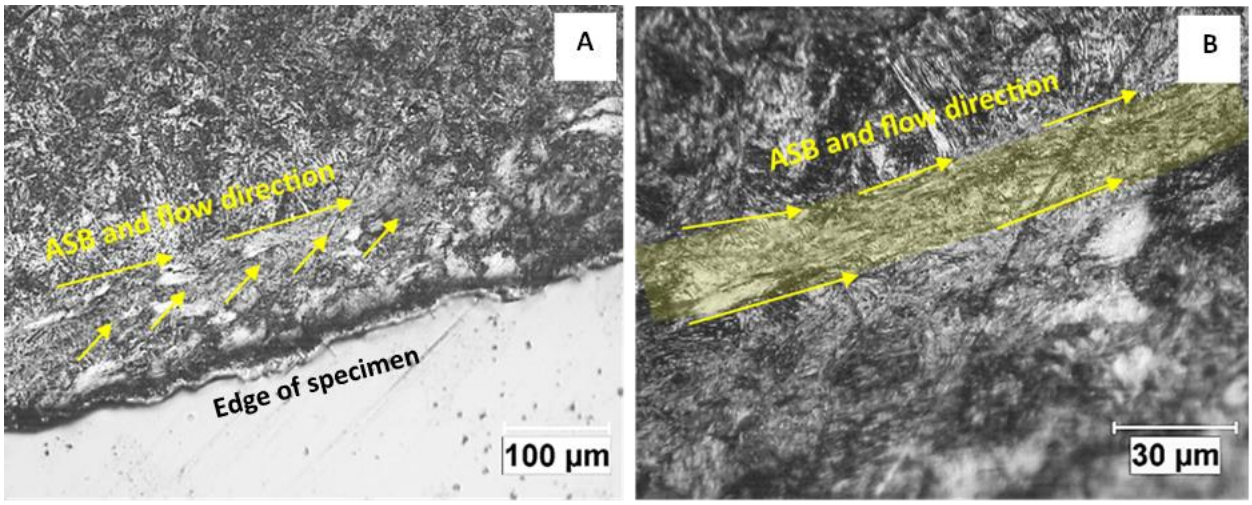

Figure 3-25: OM image of sample RT8-B: Room temperature with impact momentum 19.64 kg m/s 100x (A) and 400x (B) magnification

Under the SEM, sample RT8-B analysis is shown in Figure 3-26 with the presence of adiabatic shear bands. This is the first observable significant change to the microstructure and signifies the beginning of failure stages in the material. These are seen to be regions of the sample reflecting high energy intensity and stress concentration as seen in Figure 3-26 (A-C). This would include higher dislocation density, which would reflect in hardness tests on the surface of the shear band. This is irregular compared to its microstructure away from the ASB shown in Figure 3-26 (D). Both of these regions can be directly compared at 6500x magnification in Figure 3-26 (C) and Figure 3-26 (D) respectively. These abnormalities are also immersed in the region close to the edge of the surface where heavy deformation and enlarged lathes were seen in lower impact momentum sample RT7-B.

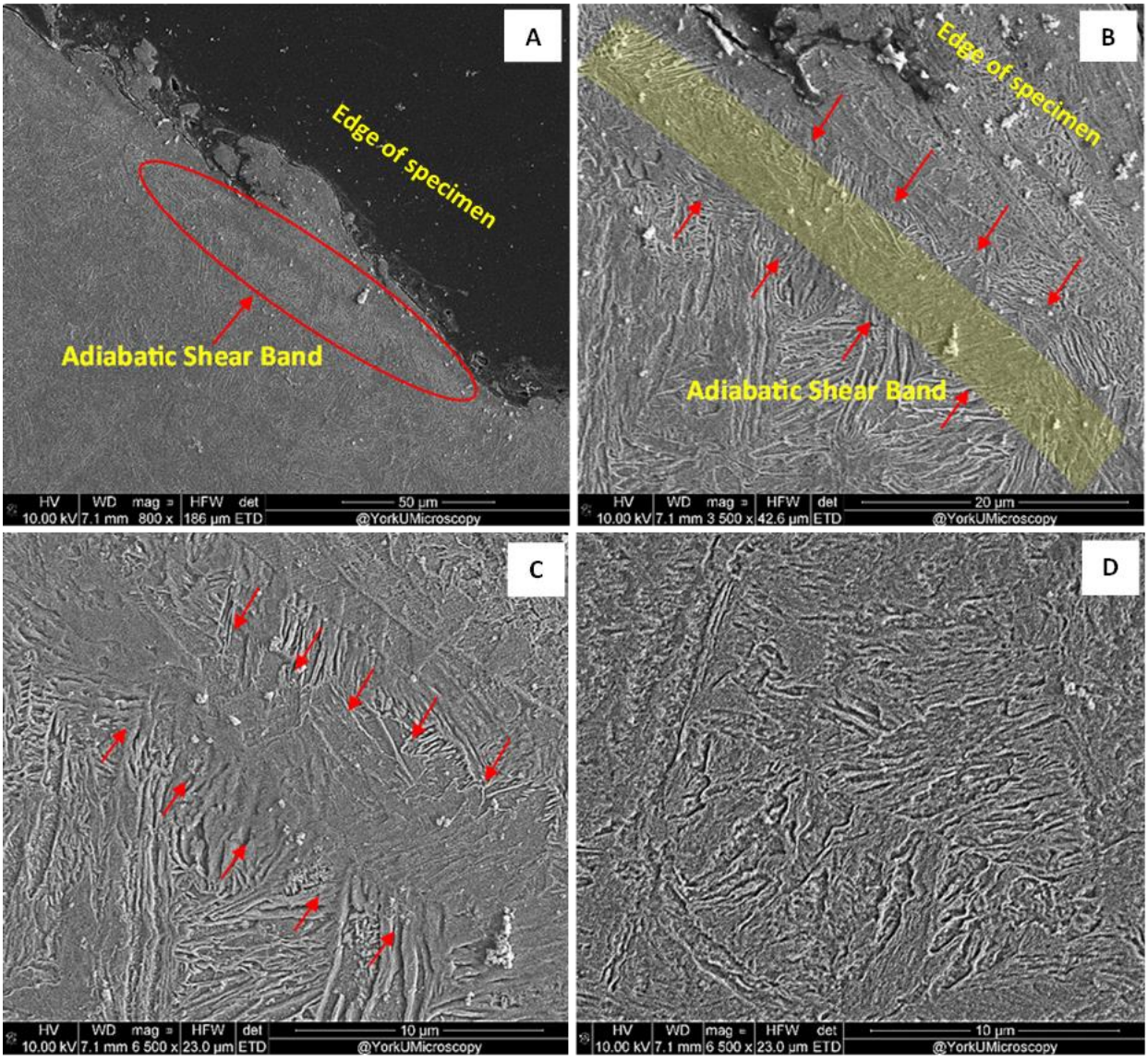

Figure 3-26: SEM images of sample RT8-B: Room temperature with impact momentum 19.64 kg m/s showing ASB at 800x magnification (A), ASB at 3500x magnification (B), ASB at 6500x magnification (C), and microstructure away from the ASB region at 6500x magnification (D)

The highest impact momentum in this series of samples that did not result in complete failure was 21.49 kg m/s (sample RT9-B). In this sample, Figure 3-27 shows an optical microscope image depicting multiple shear bands and microfractures within the ASB that were found extending from the edge of the surface along with heavy grain deformation surrounding these areas.

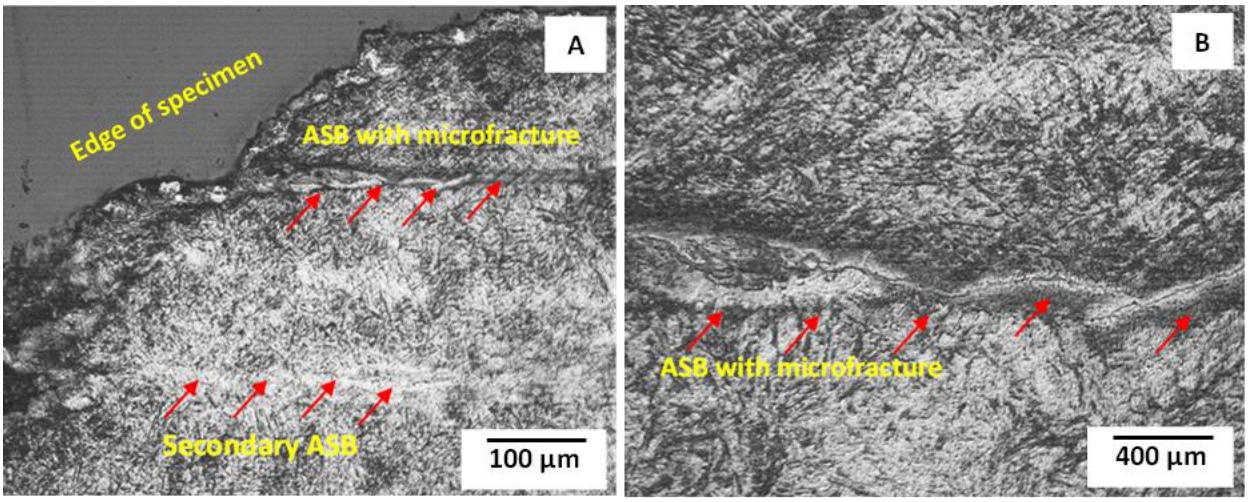

Figure 3-27: OM image of sample RT9-B: Room temperature with impact momentum 21.49 kg m/s 100x (A) and 400x (B) magnification

Looking further into this with the SEM in Figure 3-28, the ASB region near the edge of the sample is highly apparent. Voids and pits are observed within the ASB region with microcracks extending out from them. These microcracks are also seen connecting these voids, indicating a mode of failure when the impact momentum was increased beyond 21.50 kg m/s.

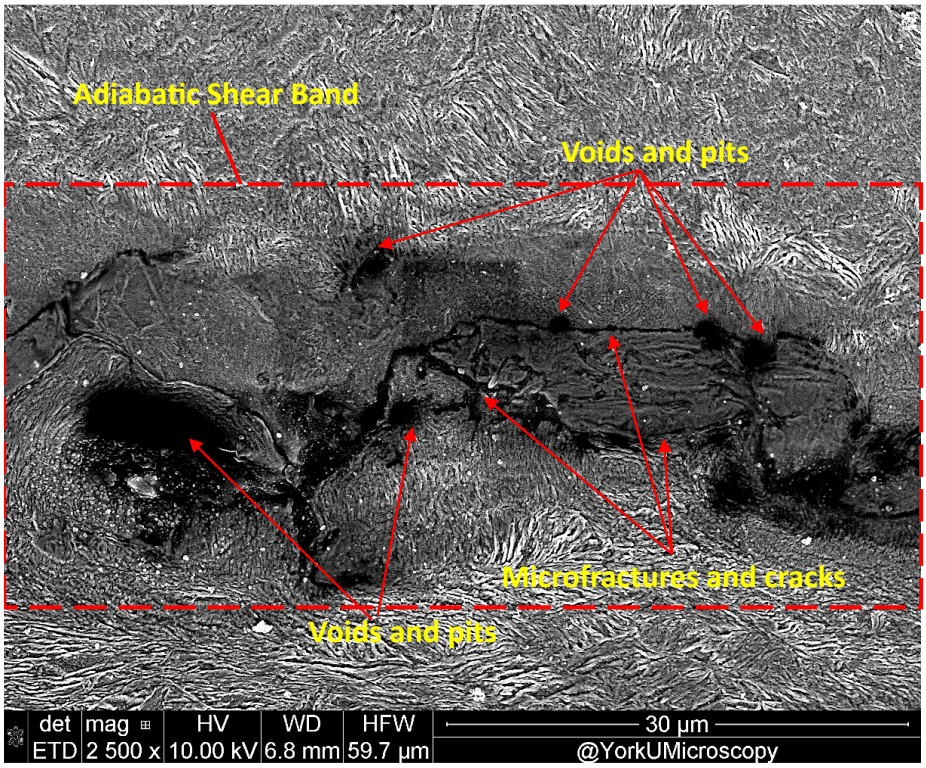

Figure 3-28: SEM image of sample RT9-B: Room temperature with impact momentum 21.49 kg m/s at 2500x magnification

3.3.4.1.1 Fractured Sample Analysis (Room Temperature)

Although the fractured samples could not produce stress-strain data, their fracture may give more information and evidence as to how the material failed. Figure 3-29 shows fractured sample RT10-A from a macroscopic view. Figure 3-30 shows OM images of the impacted surface failure. With failure already present in the material, the deformation in this sample is extreme and the ASBs in this sample are highly distinct transformed bands. These bands are present in multiple areas, indicating regions where failure originated from. This is seen as the fractures and cracks propagate from and are embedded within the adiabatic shear band. This shows a progression of deformation from the lower impact momentum samples and validates that the ASB is associated with this progression and failure. It is also important to note that the main region of failure is from the inside curvature of the sample as described in Figure 3-21 demonstrating that the stress concentrations are high close to the rim on the cylindrical surface, making it a primary location of failure. Note that the flat surface reveals the signs of ASBs, however the depth of the shear band runs through the entire specimen on sides. The failure that is seen in these tests demonstrate the most prevalent shear band that led to the crack propagation.

Figure 3-29: Image of sample RT10-A: Room temperature fracture with impact momentum 21.72 kg m/s showing failure

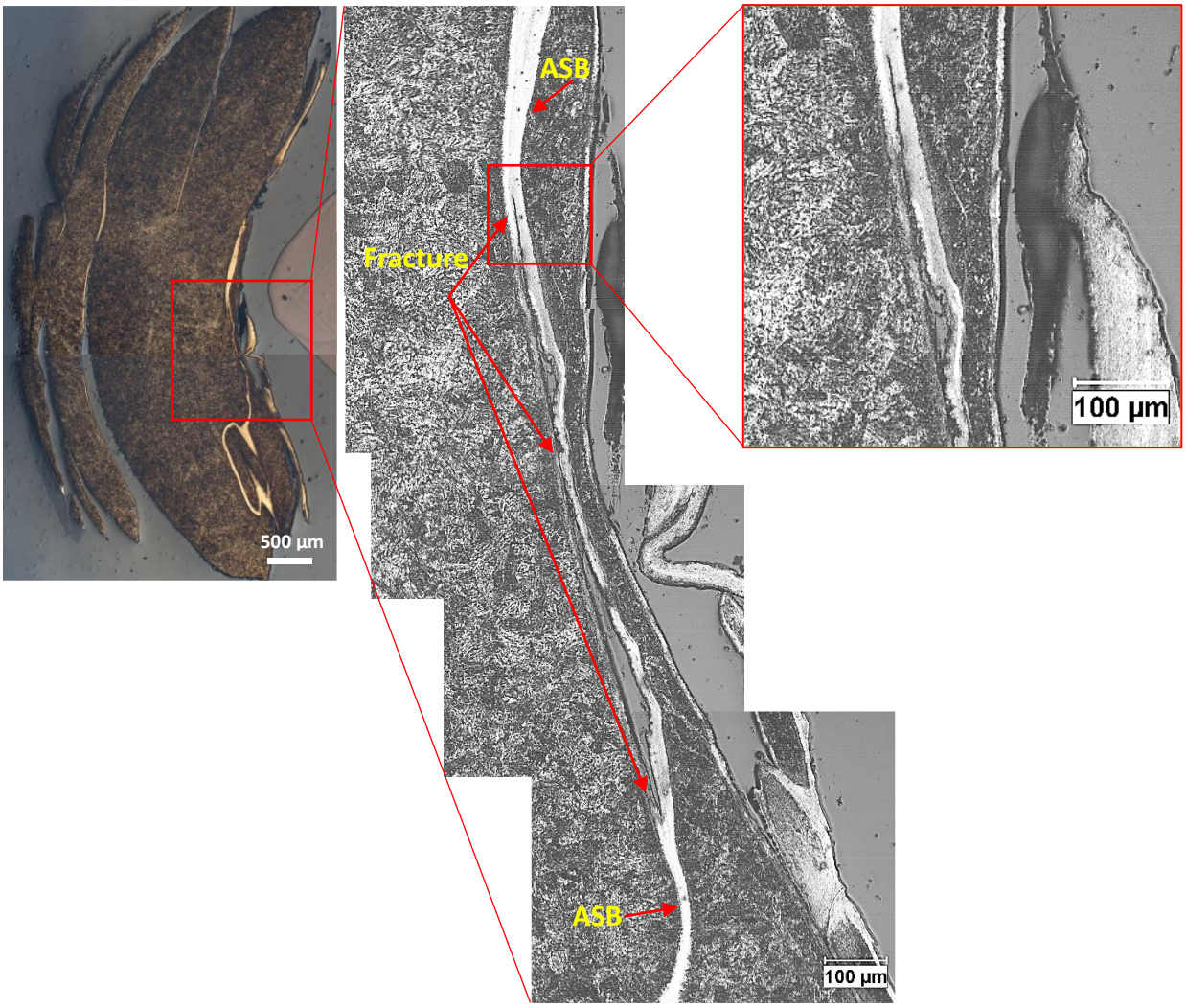

Figure 3-30: OM images of sample RT10-A with impact momentum 21.72 kg m/s showing adiabatic shear bands and crack propagation

3.3.4.2 Microscope Imaging: High Strain-Rate Compression Testing (200°C)

The impacted samples at 200°C revealed a slight change in overall microstructure where lathes and packets became less defined, however, still had a large presence. The appearance of ASBs were not visible in many of the 200°C impacted samples, nevertheless, at 20.82 kg m/s (sample T200-Y), there is an observed change in the microstructure in the form of shear flow in a narrow region depicting an ASB shown in Figure 3-31. In the 21.95 kg m/s sample (T200-ZC), heavy grain distortion close to the edge of the sample extending from the damaged edge of the sample

into a shear band was also seen in Figure 3-32, indicating the mode of failure as samples with greater impact momentum consistently fractured.

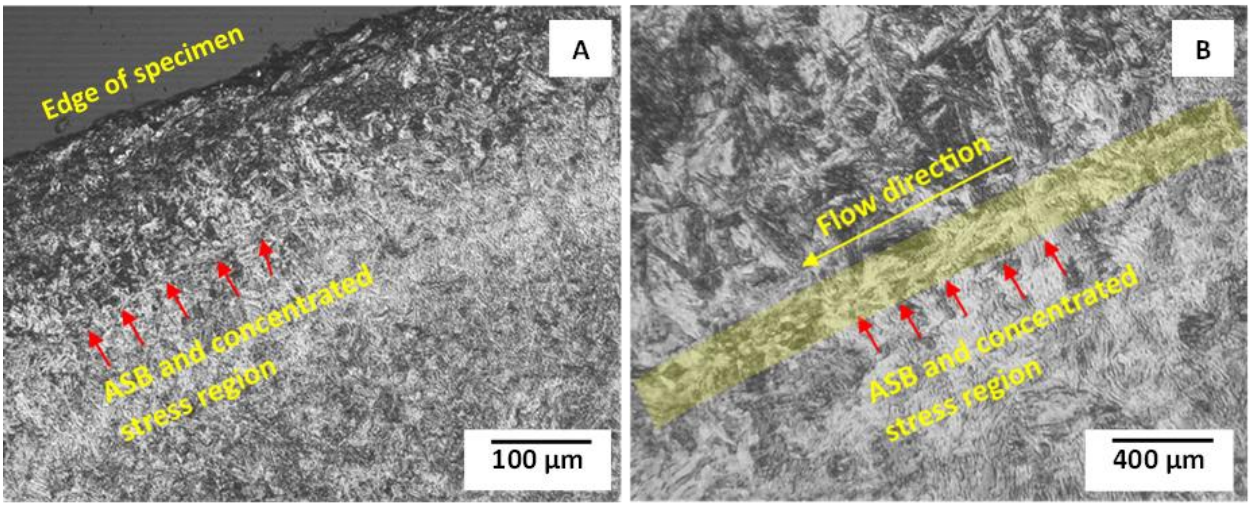

Figure 3-31: OM image of sample T200-Y: 200°C with impact momentum 20.82 kg m/s at 100x (A) and 400x (B) magnification

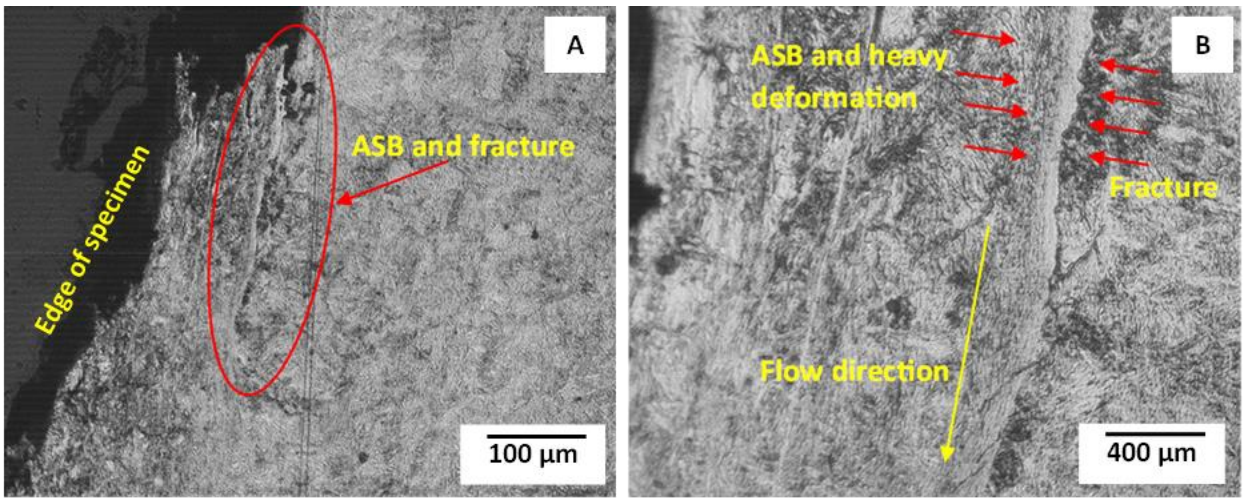

Figure 3-32: OM image of sample T200-ZC: 200°C with impact momentum 21.95 kg m/s at 100x (A) and 400x (B) magnification

The final impact momentum in which the sample did not fully fracture was at 21.95 kg m/s (sample T200-ZC). This sample was observed under the SEM for closer imaging as seen in Figure 3-33 below. Similar to the results seen at room temperature, voids and pits with connecting microcracks in the ASB region can be observed on the surface of the sample, confirming this mode of failure. These voids can also be seen within the main ASB, as well as a secondary ASB region.

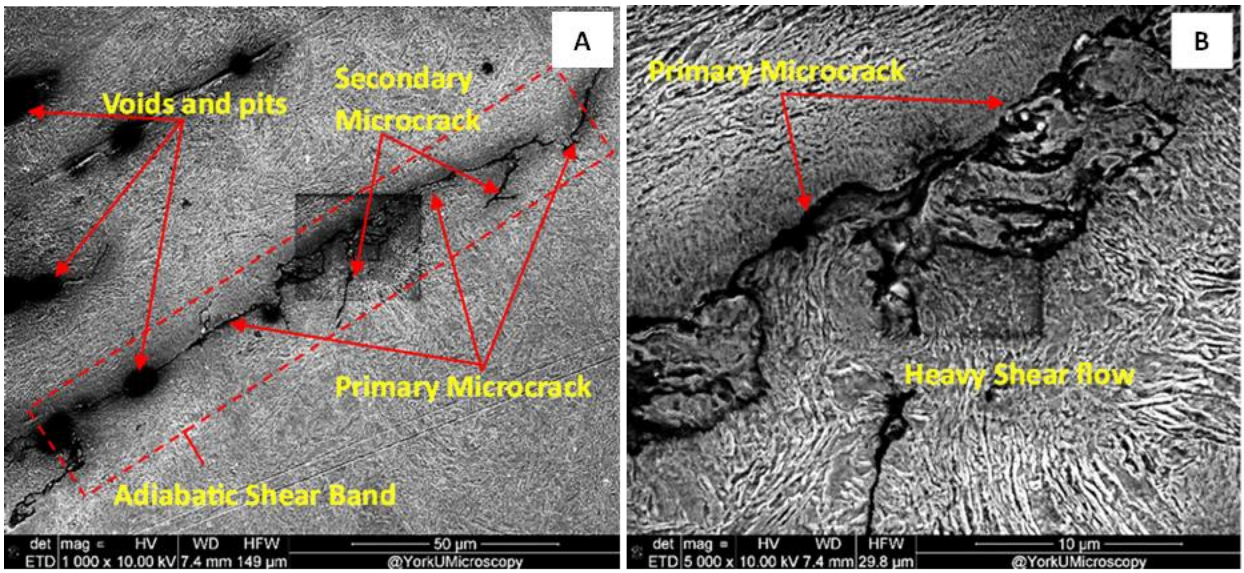

Figure 3-33: SEM image of sample T200-ZC: 200°C with impact momentum 21.95 kg m/s at 1000x (A) and 5000x (B) magnification

3.3.4.2.1 Fractured Sample Analysis (200°C)

The specimen fractured at 200°C when impacted at 21.99 kg m/s. This fractured sample can be seen in Figure 3-34. The brown pigment change in this post-impact image indicates a heavy oxidization and permanent thermal damage which occurs in metals exposed to elevated temperatures [23].

Figure 3-34: Images of sample T200-ZB: 200°C fracture with impact momentum 21.99 kg m/s showing failure and pigment change due to temperature exposure

Under optical microscope examination shown in Figure 3-35, the intense transformed shear band regions can be seen close to and at the edges of the fracture. At higher magnification, the primary and secondary ASB can be observed as well as a fracture extending through the primary shear band. At 400x magnification, the secondary ASB also shows a microcrack embedded within it. This demonstrates there is an evident correlation between the formation of ASBs and crack propagation leading to failure. This shows similarity to the other failed samples where the ASBs are an extension and part of the fractured and failed regions including at elevated temperatures.

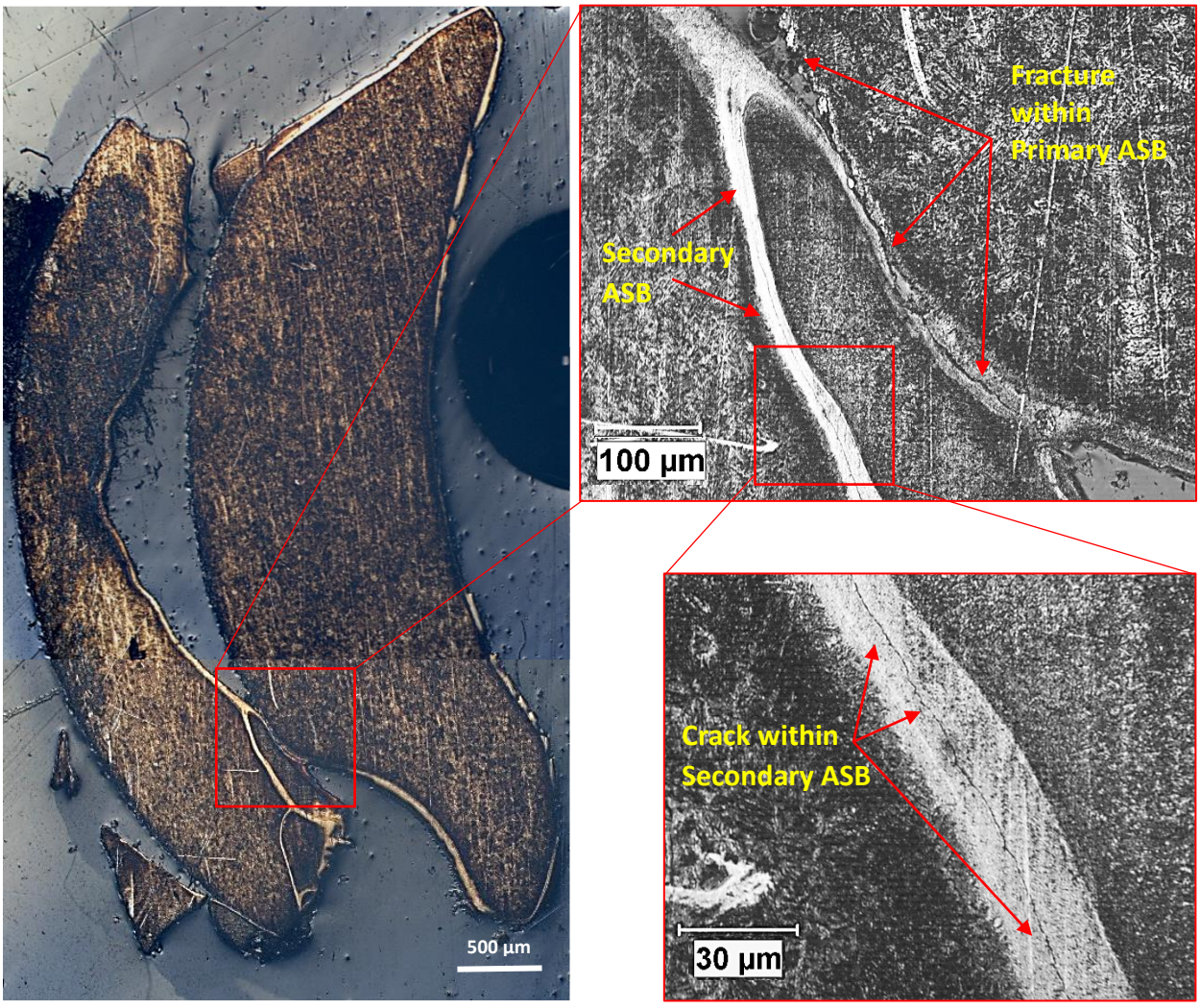

Figure 3-35: OM images of sample T200-ZB with impact momentum 21.99 kg m/s showing adiabatic shear bands and crack propagation

3.3.4.3 Microscope Imaging: High Strain-Rate Compression Testing (300°C and 400°C)

While ASBs and crack propagation are present in the room temperature and 200°C samples, at 300°C and 400°C these features were not visible. Some materials have strain rate and temperature sensitivity, indicating their mechanical behaviour changes with variations in strain rate and temperature [24]. In these cases, materials become more ductile or less prone to strain localization at elevated temperatures, which reduces the likelihood of ASB formation [25].

It is important to note that the microstructure of the 300°C sample at the highest impact momentum before achieving failure remained mostly intact after testing which can be seen in Figure 3-36. This explains its overall performance abilities seen in Figure 3-14 - Figure 3-17. Although Armox 500T is said to be affected by temperatures above 200°C, the effects of 300°C were not greatly seen likely because of its soaking time in the furnace being too short to have lasting annealing effects on the microstructure, yet still enough to affect its ability to perform slightly worse.

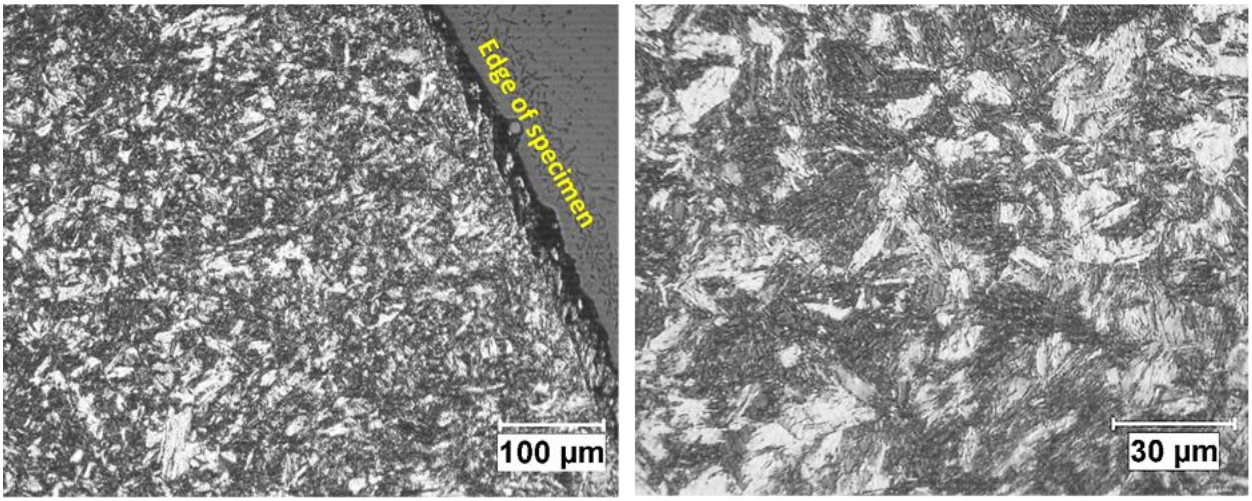

Figure 3-36: Sample T300- W: 300°C with impact momentum 19.91 kg m/s 100x (A) and 400x at edge (B)

At 400°C, even with a very short exposure to this heat, the Armox 500T sample lost its microstructure as seen in Figure 3-37 and Figure 3-38 for sample T400-U which had the highest impact without fracture at 18.30 kg m/s. The lathes and packets originally seen at room temperature

are no longer visible, there is a heavily refined grain structure and the rolling direction became visible. The performance at this temperature was extremely poor compared to other samples likely because of this microstructural property change.

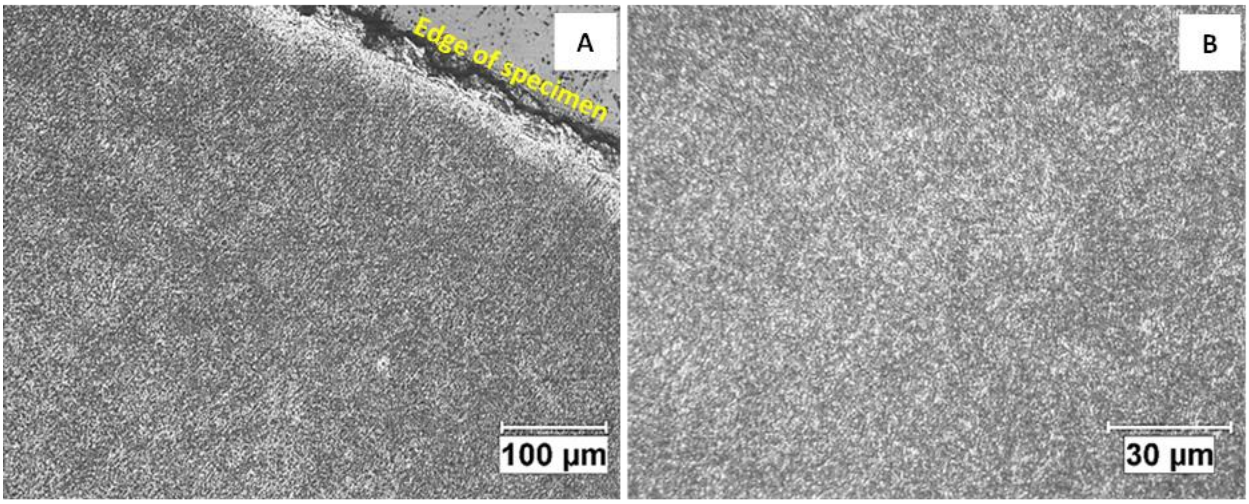

Figure 3-37: Sample T400-U: 400°C with impact momentum 18.30 kg m/s 100x and 400x at edge

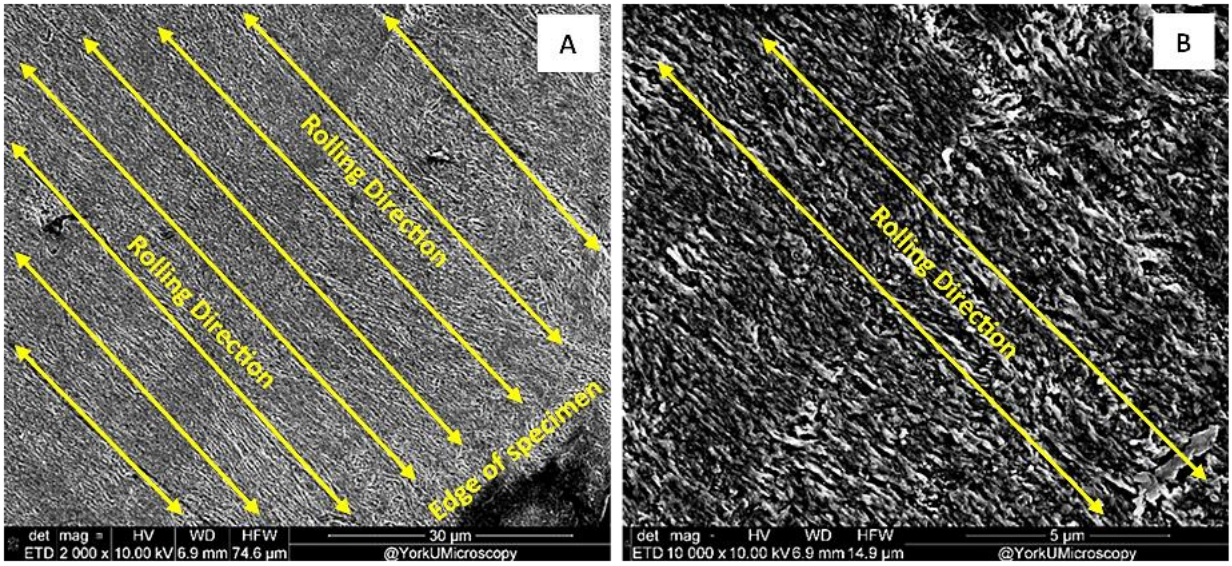

Figure 3-38: SEM image of sample T400-U: 400°C with impact momentum 18.30 kg m/s 2000x and 10000x magnification at edge

3.3.4.3.1 Fractured Sample Analysis (400°C)

The specimen fractured at 400°C when impacted at 19.67 kg m/s. Figure 3-39 shows that the fracture resulted in multiple failure points at the rim of the cylindrical sample. It is important to note the blue pigment change in this post-impact image indicating a heavy oxidization and permanent thermal damage which occurs in metals exposed to temperatures above 300°C [23].

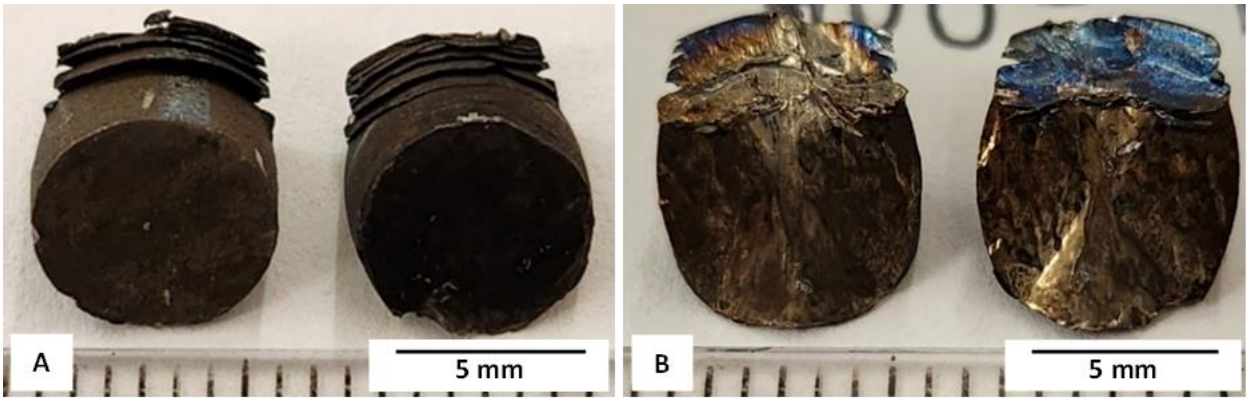

Figure 3-39: Images of sample T400-V: 400°C fracture with impact momentum 19.67 kg m/s showing multiple failure points (A) and pigment change due to temperature exposure (B)

Upon further optical microscope examination shown in Figure 3-40, it appears that each of the folded layers of failure has a shear band associated with it and secondary shear bands nearby. Furthermore, similar to the other failed samples, the ASBs are an extension and part of the fractured and failed regions, signifying that even at elevated temperatures, there are stress-concentrated regions that lead to failure, consistent with the lower temperature samples.

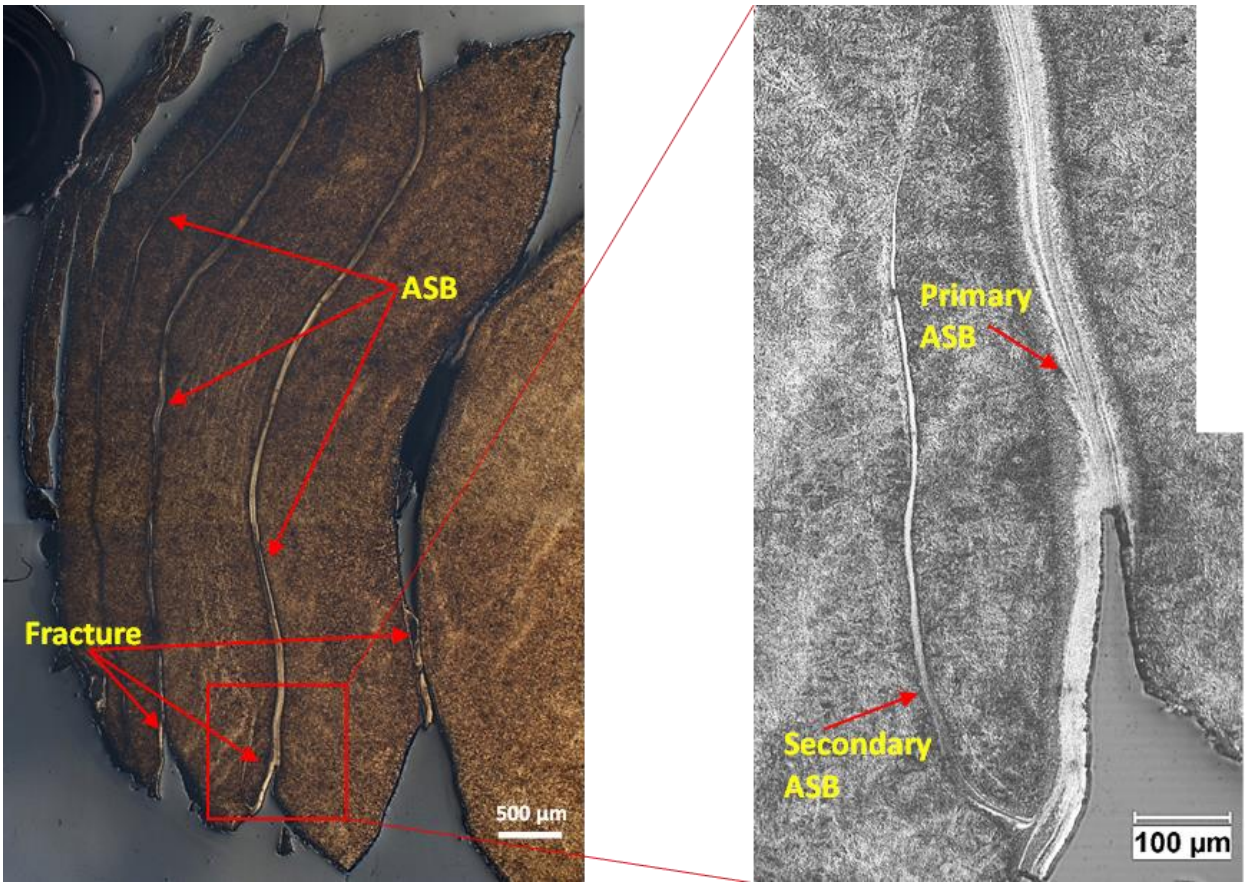

Figure 3-40: OM images of sample T400-V with impact momentum 19.67 kg m/s showing adiabatic shear bands and crack propagation

Comparing the macroscopic failure of the 400°C sample to the 200°C and room temperature failed samples, there are some significant differences. In Figure 3-39 (A), it is evident that there was more than one failure point as the specimen appears to have multiple folds. Upon further investigation, under the optical microscope, each of these folds showed evidence of multiple shear bands and secondary shear bands, indicating multiple areas of stress-concentrated regions. This demonstrated the effects of embrittlement rather than thermal softening. In the case of thermal softening, the material would have distributed this stress over a greater region, showing a lack of shear bands, whereas, in this case, the number of shear bands increased, as well as the number of failure points, in a non-ductile fracture appearance.

3.3.5 Vickers Microhardness Test

A Vickers microhardness test is a widely used method to assess the hardness of a material's surface [25]. It provides insight into the material`s mechanical properties and behaviour under different conditions. When applied to Armox 500T samples, it can help understand several important aspects. ASB regions of an impacted surface tend to have higher hardness than the rest of the surface due to its intense strain and heavy dislocation region. This information can also help determine impact severity based on more pronounced ASBs and deformation.

For this analysis, 10 indents were taken in each region of the sample within the suspected shear band region and away from the shear band using a 100 gf (0.98 N) and 15-second dwell time. The idents were spaced more than 200µm away from each other to prevent deformation from each indent from interfering with the next indent measurement. This ensures consistent and accurate results when averaged. A depiction of this can be seen in Figure 3-41 below.

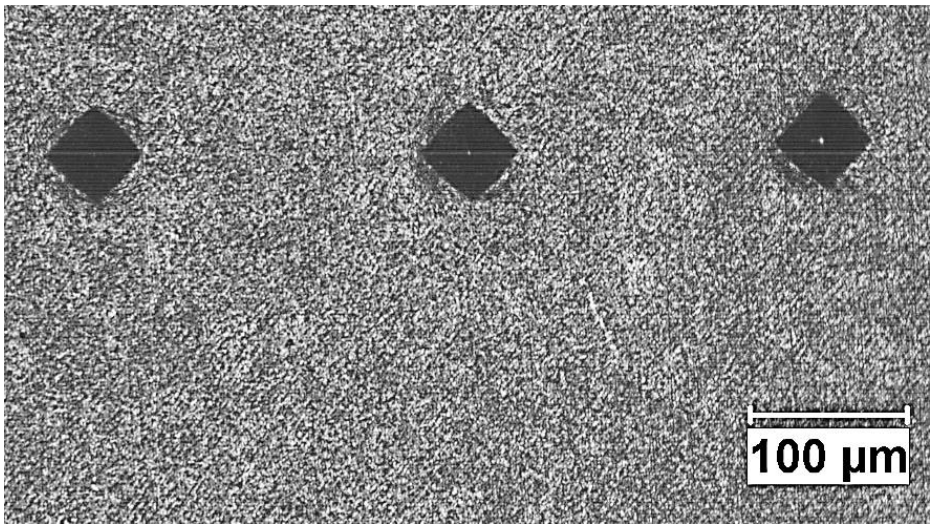

Figure 3-41: Vickers micro-hardness indents conducted on sample T400-U at 100x magnification

3.3.5.1 Impacted Samples and its Effects on Hardness

In the room temperature impacted samples, the ASBs begin to show presence on the surface of the sample after an impact momentum of 19.64 kg m/s is applied to it. Evidence to confirm these regions are ASBs is seen in Figure 3-42 where a micro-Vickers hardness comparison is conducted between the center region of the specimen and possible ASB regions near the edge of the surface. The ASB regions in samples RT8-B and RT9-B showed noticeable increases in hardness. RT9-B had a larger increase likely due to its greater dislocation density and brittleness resulting from a higher impact momentum.

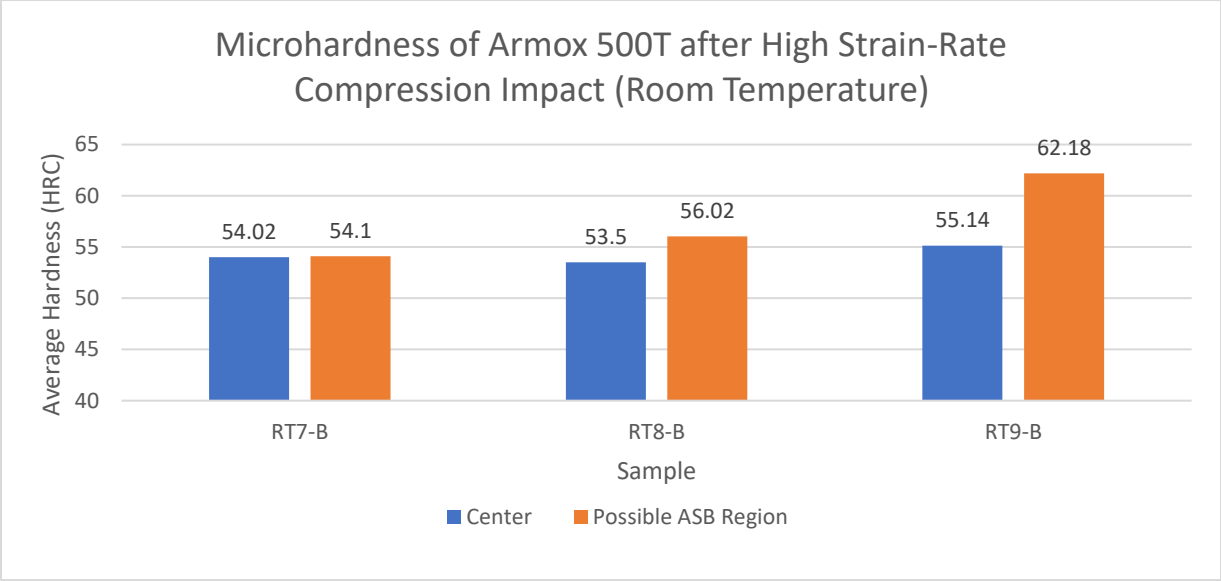

Figure 3-42: Microhardness of Armox 500T at room temperature post impact momentum of 18.87 kg m/s, 19.64 kg m/s, and 21.49 kg m/s respectively

At 200°C, the ASBs were not visibly present until an impact momentum of 20.82 kg m/s as seen in Figure 3-43. Similar to the room temperature samples, there was a significant difference in hardness between the center region of the sample and the ASB region. Furthermore, sample T200-ZC (which had a higher impact momentum) showed ASB regions to have higher hardness than the T200-Y sample, again indicating a greater dislocation density.

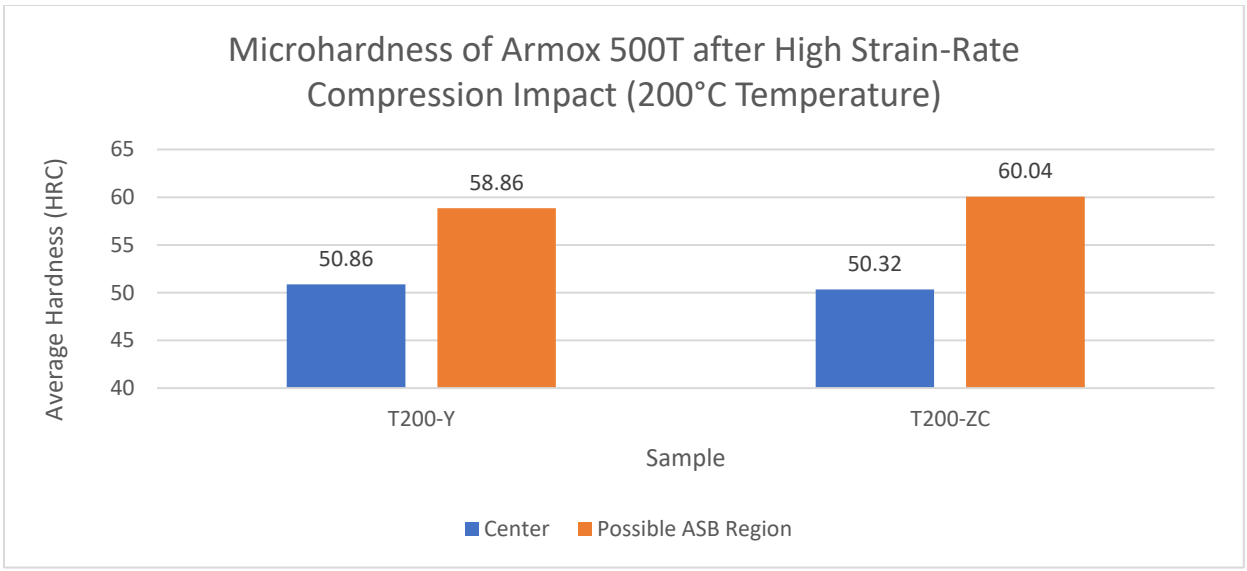

Figure 3-43: Microhardness of Armox 500T at 200°C post impact momentum of 20.82 kg m/s and 21.95 kg m/s respectively

At 300°C, the ASBs were not visibly present. A Vickers hardness test was completed on the highest impact momentum sample at this temperature (sample T300-W with an impact momentum of 19.91 kg m/s) as seen in Figure 3-44. There was no quantitative difference between the hardness at the center of the sample and the hardness of the region near the edge where the shear band was seen in other samples. This confirms with further evidence that an ASB is not present in samples exposed to temperatures of 300°C.

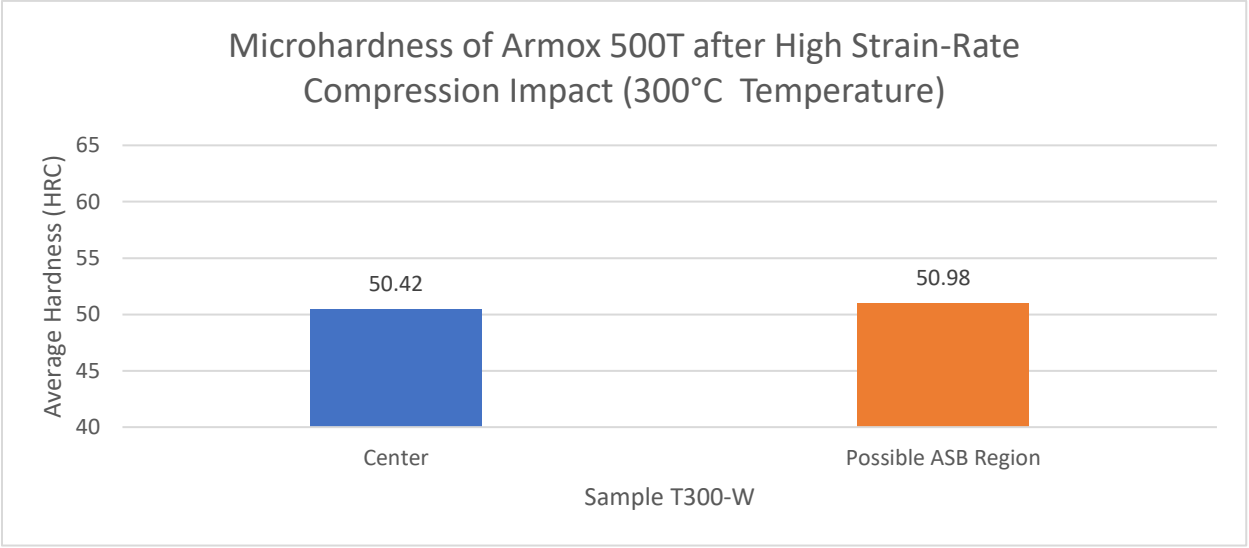

Figure 3-44: Microhardness of Armox 500T at 300°C post impact momentum of 19.91 kg m/s

At 400°C, the ASBs were not visibly present. A Vickers hardness test was completed on the highest impact momentum sample at this temperature (sample T400-U with an impact momentum of 18.30 kg m/s) as seen in Figure 3-45. Similar to the 300°C. There was no quantitative difference between the hardness at the center of the sample and the hardness of the region near the edge where the shear band was seen in other samples. This again confirms with further evidence that an ASB is not present in samples exposed to temperatures of 300°C and 400°C.

This relates to the iron-carbon phase diagram discussed in Chapter 2. When medium carbon steels are exposed to temperatures above 200°C and also below the eutectoid temperature of 723°C, the steel`s martensitic hard structure can become pearlite, ferrite, and cementite soft structures [26]. This reduces the overall hardness and strength of the material.

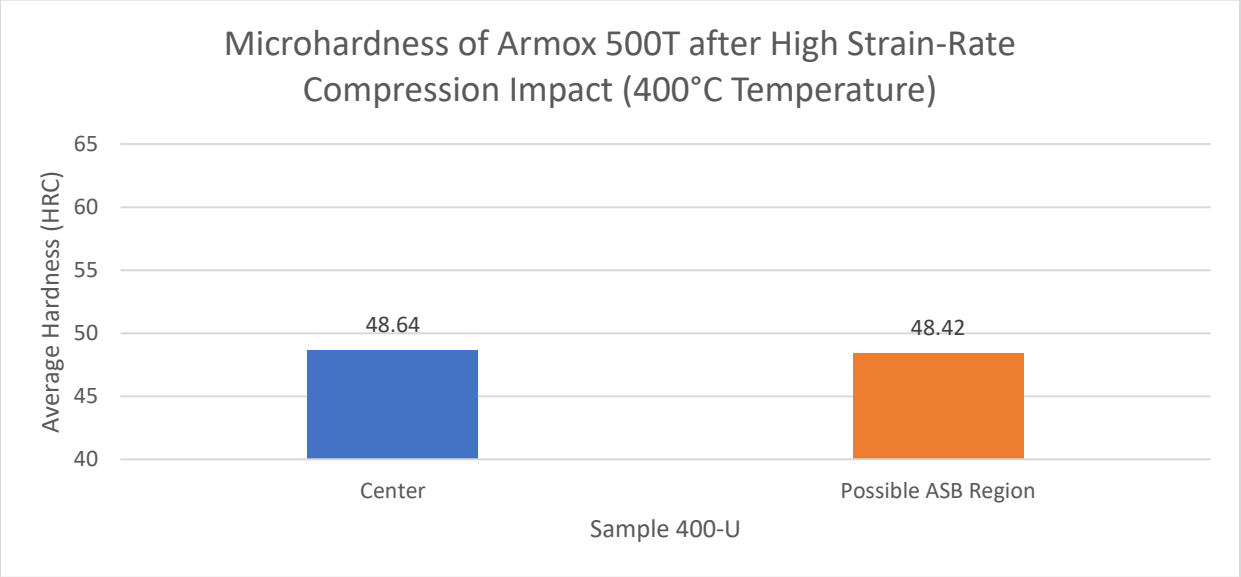

Figure 3-45: Microhardness of Armox 500T at 400°C post impact momentum of 18.30 kg m/s

3.4 Conclusion

It has been established that the initiation and formation of ASBs in Armox 500T is critically dependent on the microstructure and deformation mechanisms of the material. In order to better understand these mechanisms, it is important to develop a study involving the microstructure of Armox pre-impact, post-impact, and post-impact at elevated temperatures. It was observed that the Armox responds to increasing impact strain through the emergence of enlarged grains and grain refinement, which led to the development of ASBs and voids, eventually resulting in crack initiation and failure.

It was shown through testing that in high strain rates and increased temperature (coupled) compression conditions, the performance of Armox is significantly affected. At room temperature, the maximum impact momentum the specimen could withstand without fracturing was 21.49 kg m/s. At 200°C this increased to 21.95 kg m/s (2.0% more than room temperature), demonstrating it can withstand larger forces while maintaining its structural integrity and allowing 2.6% more compression. At 300°C and 400°C, these values were significantly reduced with a maximum of 19.91 kg m/s and 18.30 kg m/s respectively. This shows a trend of degradation in material properties at temperatures above 200°C regarding high strain rate compression conditions.

The adiabatic shear bands were visible under the OM and SEM for compression samples impacted beyond 19.60 kg m/s in room temperature conditions. Beginning with large deformed grains near the edge of the sample, the ASBs shortly followed with the appearance of a 20-50 μm wide strip along the edge of the sample with a refined grain structure different from the rest of the surface. There was a presence of voids and pits within these ASBs indicating significant damage and porosity at the surface. As the impact momentum was increased, cracks were seen originating from these voids and connecting them in a brittle fashion. These ASBs were confirmed with further

evidence of microhardness tests conducted over the surface of the specimen. This serves as evidence of the development of damage leading to the complete fracture and failure in the material. At 200°C, these ASBs were not visible until an impact momentum of 20.82 kg m/s, showing further evidence of increased performance at elevated temperatures. Beyond this temperature, the 300°C and 400°C impacted samples did not visibly show any presence of ASBs. This is likely due to the elevated temperature allowing for stress relieving, high ductility, and altered grain structure, all preventing the extreme localization of stresses during impact.

3.5 References

[1] A. Rashid and M. Jahan, "Microfabrication by electrical discharge machining-based hybrid processes," *Micro Electro-Fabrication,* pp. 33-62, 2021.

[2] H. Marashi, A. Sarhan, I. Maher and M. Sayuti, "Techniques to Improve EDM Capabilities: A Review," *Comprehensive Materials Finishing,* Vols. 171-202, 2017.

[3] D. Bańkowski and P. Młynarczyk, "Influence of EDM Process Parameters on the Surface Finish of Alnico Alloys," *Materials,* vol. 15, no. 20, p. 7277, 2022.

[4] A. Khan, J. Balzer, J. Wilgeroth and W. Proud, "Aspect ratio compression effects on metals and polymers," *Journal of Physics: Conference Series,* vol. 500, no. 18, 2014.

[5] A. Eliasu, S. H. Duntu, K. S. Hukpati, M. Y. Amegadzie, J. Agyapong, F. Tetteh, A. Czekanski and S. Boakye-Yiadom, "Effect of individual printing parameters on residual stress and tribological behaviour of 316L stainless steel fabricated with laser powder bed fusion (L-PBF)," *The International Journal of Advanced Manufacturing Technology,* vol. 119, p. 7041–7061.

[6] F. Tetteh, S. H. Duntu, J. Agyapong and S. Boakye-Yiadom, "Influence of precipitate distributions on adiabatic shear band formation and flow behavior of heat-treated 7050 aluminum alloy," *The International Journal of Advanced Manufacturing Technology,* vol. 126, pp. 5435-5456, 2023.

[7] D. Mateos, "Stress-State and Strain-Rate Dependent Multiscale Characterization of Armox 500T," Toronto, 2023.

[8] N. Bassima and S. Boakye-Yiadom, "Mechanism of grain refinement and its effect on Adiabatic Shear Bands in 4340 steel and pure copper during impact," in *DYMAT 2015 - 11th International Conference on the Mechanical and Physical Behaviour of Materials under Dynamic Loading*, 2015.

[9] S. Boakye-Yiadom, . A. Khan and . N. Bassim , "Deformation Mapping and the Role of Carbides on the Microstructure and Properties of Evolved Adiabatic Shear Bands," *Metallurgical and Materials Transactions A,* vol. 45, pp. 5379-5396, 2014.

[10] A. Odeshi, M. Bassim and S. Al-Ameeri, "Effect of heat treatment on adiabatic shear bands in a high-strength low alloy steel," *Materials Science and Engineering: A,* vol. 419, no. 1-2, pp. 69-75, 2006.

[11] A. Tyas and Z. Ozdemir, "On backward dispersion correction of Hopkinson pressure bar signals," *Philosophical transactions. Series A, Mathematical, physical, and engineering sciences,* 2014.

[12] J. Park, "Interpretation of dynamic tensile behavior by austenite stability in ferrite-austenite duplex lightweight steels," *Scientific Reports,* vol. 7, no. 1, 2017.

[13] C. Sato and S. Marzi, "High-rate loading and impact in adhesively bonding joints," *Adhesive Bonding,* pp. 257-293, 2021.

[14] "The use of the direct impact Hopkinson pressure bar technique to describe thermally activated and viscous regimes of metallic materials," *Philosophical Transactions of the Royal Society A: Mathematical, Physical and Engineering Sciences,* vol. 372, no. 2023, 2014.

[15] Magnatrol Valve Corporation, "BULLETIN 3020-A," 2023.

[16] S. Boakye-Yiadom, "Microstructural Evolution of Adiabatic Shear Bands in Steel," Winnipeg, 2014.

[17] SSAB, "Data sheet 195 Armox 500T," 2017.

[18] N. A. Safford, *High strain rate studies with the Direct Impact Hopkinson Bar,* Cambridge, 1988.

[19] Y. Cengel and A. Ghajar, Heat and Mass Transfer: Fundamentals and Applications, Sixth Edition ed., Stillwater, Oklahoma: McGraw-Hill Education , 2020.

[20] E. Yeter, "Damage resistance investigation of Armox 500T and Aluminum 7075 T6 plates subjected to drop-weight and ballistic impact loads," *Sakarya University Journal of Science,* vol. 23, no. 6, pp. 1080-1095, 2019.

[21] Y. Bai and Q. Bai, "Heat Transfer and Thermal Insulation," in *Subsea Engineering Handbook*, Second ed., 2019, pp. 363-408.

[22] C. Kwan, L. Wang, K. Xia and Z. Wang, "Curved nanotwinned structure in Ni induced by dynamic compression," *Journal of Materials Science,* vol. 52, 2017.

[23] P. Olaru, "Temper Colors For Steel," in *AGIR-SETEC 2020*, 2020.

[24] I. Barenyi, O. Hires and P. Liptak, "Changes in Mechanical Properties of Armoured UHSLA Steel ARMOX 500 After Over Tempering," in *Problems of Mechatronics Armament Aviation Safety Engineering*, 2013, pp. 7-14.

[25] M. Cheol, S. Kim, D. Kim, H. Park, S. Hong, H. Kim, H. Kim, S. Sohn and S. Lee, "Understanding of adiabatic shear band evolution during high-strain- rate deformation in high-strength armor steel," *Journal of Alloys and Compounds,* vol. 845, 2020.

[26] Cambridge University Engineering Department, "The Eutectoid Reaction," 2023. [Online]. Available: http://www-g.eng.cam.ac.uk/mmg/teaching/typd/addenda/eutectoidreaction1.html#:~:text=In%20the%20Fe%2DC%20system,temperature%20(723%C2%B0C)..

CHAPTER 4

Quasistatic Tensile Loading with Varying Temperatures on Armox 500T

4.1 Introduction

In addition to the high strain rate and high temperature coupled compression testing, a quasistatic variable temperature test procedure was completed. This test covers a range of temperatures from low to high temperatures (0°C-300°C) based on ASTM E8/E8M standards. This would allow a much greater understanding of the material behaviour under lower stress conditions at high temperatures, relating to general hot forming in the process of manufacturing. The low temperature nature of this testing allows for a new understanding of this material behaviour in low-temperature environments. It also offers insights into the material's response during manufacturing with cold-forming techniques.

In literature, most published journal articles are focused on the raw data captured from tensile tests; however, there are a limited number of studies that analyze the failure mechanism or fracture surface to understand the true nature of the material [1] [2] [3] [4].

4.2 Methodology

In this study, the Armox 500T performance under variable temperature tensile loading was investigated. EDM cutting was used to create precision-cut tensile specimen and tensile testing in the low strain rate range was performed using a Mechanical Testing System (MTS) to induce failure. Furthermore, these conditions were amplified by coupling them with both high and low-temperature exposure. Quantitative data was achieved through the use of a load cell, characterizing the material through stress-strain curves. OM and SEM imaging were used to examine the fracture surface to understand the nature of the failure.

4.2.1 Tensile Sample

The specimen was obtained from a large piece measuring 76 cm x 76 cm x 3 cm, specifically from an Armox 500T hot rolled slab. For consistency, all specimen were extracted from the slab's surface using EDM. EDM is notable for its capability to shape conductive materials, especially useful for materials with harder properties [1] [2]. Its non-contact nature allows for high geometric precision and minimal vibration making it beneficial for achieving a high-quality surface texture while preserving the material's microstructure [3]. A depiction of the cutting surfaces and dimensions can be seen in Figure 4-1.

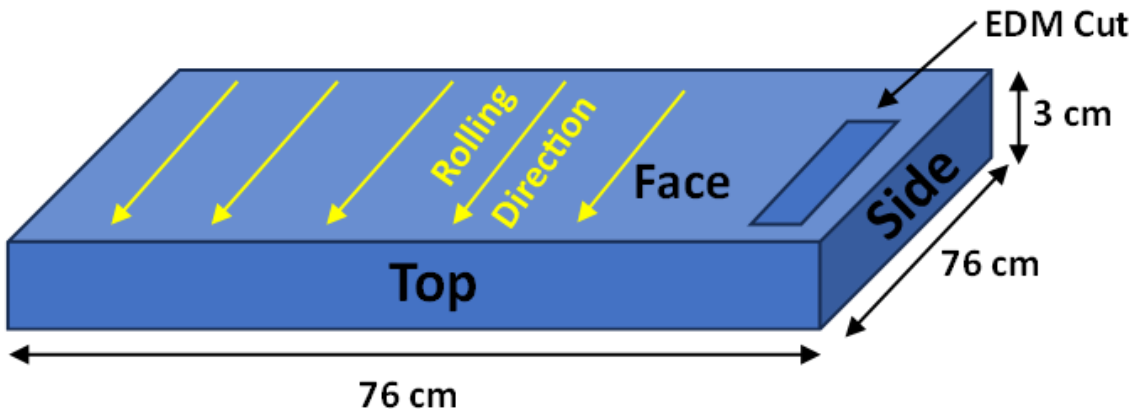

Figure 4-1: As received Armox 500T bulk material size, rolling direction, and EDM cutting surface for tensile specimen

The tensile specimen is based on the American Society for Testing and Materials (ASTM) standard E8/E8M [2]. The size of the specimen was reduced by 50% due to the strength of the material and the maximum 30KN load of the MTS machine. The exact schematic of the tensile sample can be seen in Figure 4-2.

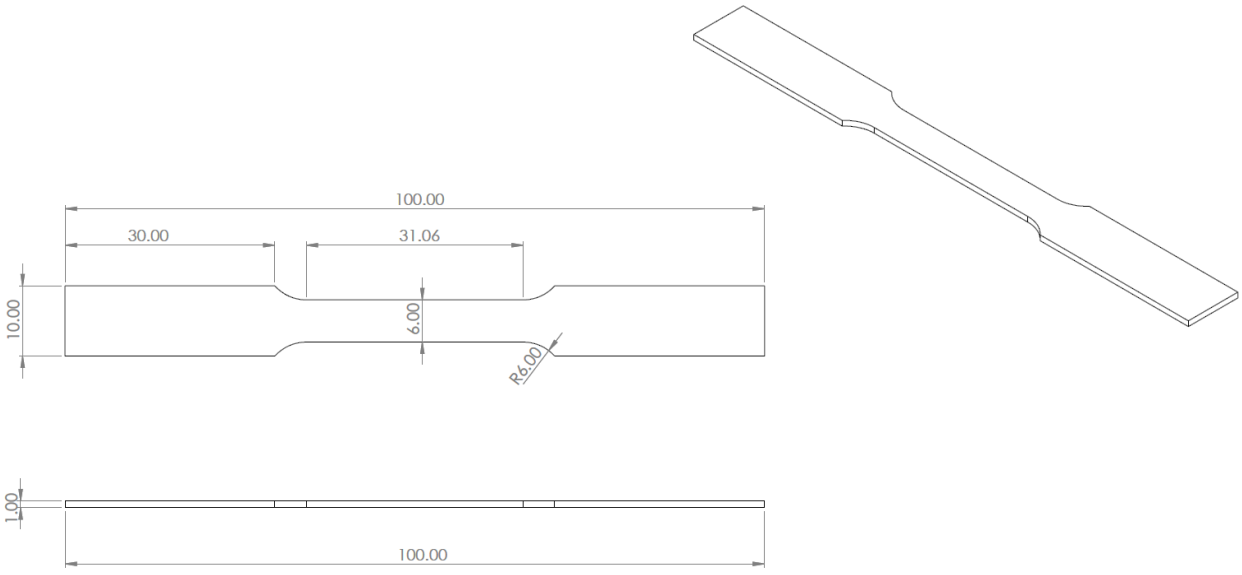

Figure 4-2: Armox 500T quasistatic tensile specimen

4.3 Variable Temperature Quasistatic Tensile Testing

4.3.1 Material Test Systems Machine

The MTS Criterion Series 40 Electromechanical Universal Test System (Model 43) is a well-suited piece of equipment for the purposes of quasistatic tensile testing. Its size allows for the use of an insulated 3119-600 series environmental chamber to be added which prevents significant changes in temperature during the varying temperature testing, and therefore, better temperature consistency during each test. A Digi-Sense TC5000 Benchtop PID Temperature Controller was used to control, set, and measure temperatures within the environment, receiving feedback from a (Digi-Sense High-Temperature Wire Probes - Fiberglass Insulated) thermocouple which measured temperature fluctuation to be within ±5°C.

Another feature of this particular MTS model is the fact that its clamps are smaller than those of the larger MTS models, allowing for the high-temperature furnace to be fitted around the specimen. Specifically, a 1200-watt, Jinbaihe Ceramic Band Heater capable of outputting temperatures up to

1000°C was the heating source mounted around the clamps. A schematic can be seen in Figure 4-3.

To achieve low-temperature environments, the chamber was filled with cold air sourced from the Temptronic ATS-545-M Thermostream Cycling System. This machine is capable of producing temperatures as low as -80°C.

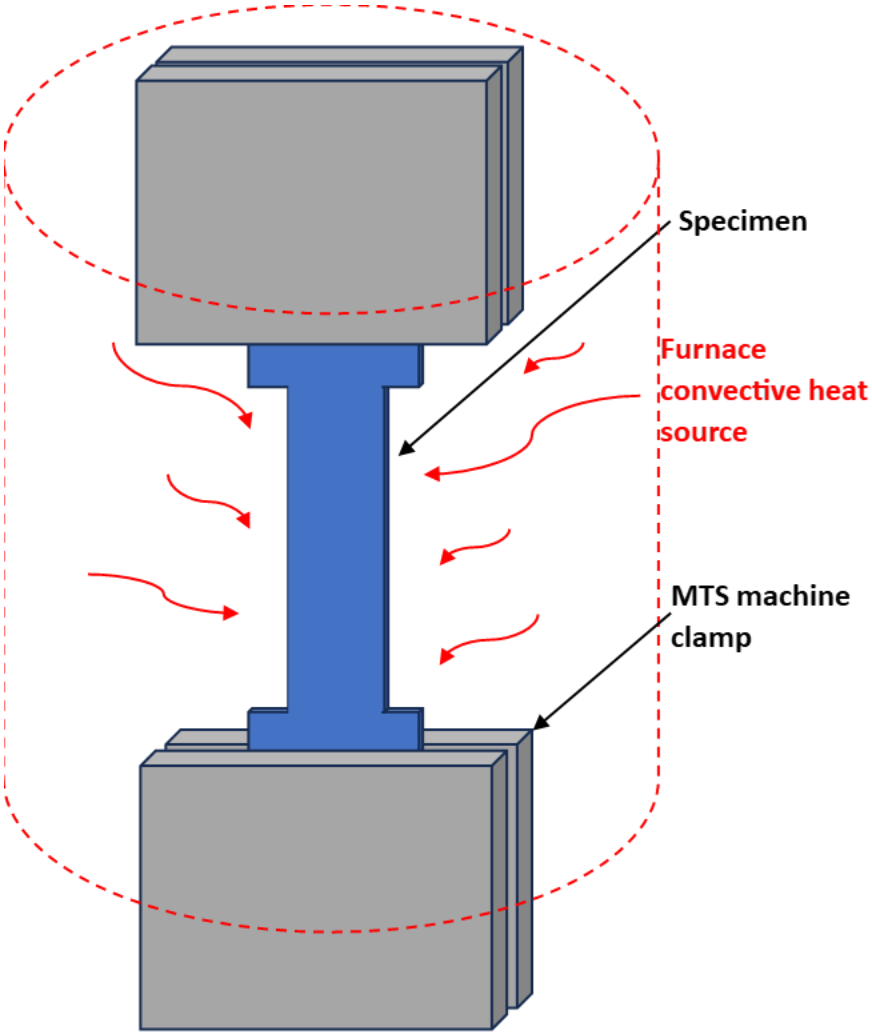

Figure 4-3: Heat transfer to tensile specimen

Heat calculations:

h_{air} = 25 W/m^{2}K [3]

$k_{\text{high carbon steel}}$ = 58 W/m-k [4]

$c_{\text{p Armox 500T}}$ = 455 Jkg^{-1} K^{-1} [5]

ρ_{Armox} = 7800 kg/m^3 [6]

T_i = 23°C

T_∞ = 100, 200, 300°C

T_0 = 0.95* T_∞

m_{Armox} = 0.0017 kg

$A_{\text{Surface (convection)}}$ = 0.0001692 m^2

$A_{\text{Surface (conduction)}}$ = 0.00003117 m^2

$L_{c\ (\text{Thickness of Armox})}$ = 0.001 m

$r_{0\ (\text{Radius of Armox})}$ = 0.0005 m

With a Biot number below 0.1, it is reasonable to consider that the resistance to internal heat conduction is considerably lower than the convection at the surface [12]. This principle is used to validate the assumption that temperature gradients within the system are negligible and have a minimal impact on overall heat transfer. The small size of the specimen in this case is a contributing factor. Given that the Biot number is 0.0087, it is reasonable to infer that there is constant temperature from the surface throughout the entire material.

There is one method of heat transfer to the specimen in this testing procedure. The energy from the furnace provides convective heat transfer to all four sides of the specimen placed inside the heated system. This heat transfer method must be taken into account when calculating the amount of time it takes for the specimen to reach the implied temperature seen below in Equation 4.3-1 - Equation 4.3-4.

$\boldsymbol{Biot\ Number = \frac{hr_0}{k}}$	*Equation 4.3-1*	$\boldsymbol{Biot\ Number = 0.0087}$ Therefore, $A_1 = 1.0025$ [4] $\lambda_1 = 0.1412$ [4]
$\boldsymbol{\alpha = \frac{k}{\rho * c_p}}$	*Equation 4.3-2*	$\alpha = 1.634263*10^{-5}$
$\boldsymbol{\frac{T_0 - T_\infty}{T_i - T_\infty} = A_1 e^{-\lambda_1^2 \tau}}$	*Equation 4.3-3*	$\tau_{0°C} = 309.658$ $\tau_{100°C} = 137.1475$ $\tau_{200°C} = 144.1292$ $\tau_{300°C} = 146.256$
$\boldsymbol{\tau = \frac{\alpha * t}{r_0^2}}$	*Equation 4.3-4*	**$t_{0°C}$ = 4.737 seconds** **$t_{100°C}$ = 2.098 seconds** **$t_{200°C}$ = 2.2048 seconds** **$t_{300°C}$ = 2.2373 seconds**

4.3.2 Test Matrix

The test procedure for room temperature testing involves setting the specimen in the center of the bottom clamp and securing it such that it is vertical. The top clamp is then secured on the other end of the specimen with a crosshead of 50mm, making sure that it is centred between both clamps. Through the MTS software, the strain rate was set to 0.03 s^{-1} based on the cross-sectional area and gauge length of the specimen [7] [8]. This is based on the loading rate of 1 mm/s in tension. The test was then executed until tensile failure occurred, at which point, the specimen was released from the clamp.

For testing at elevated temperatures, similar steps were followed with minor changes. Once the bottom clamp was secured the to vertical specimen, the ceramic heater was placed over it before clamping the top end of the specimen. The purpose of this was to secure the specimen in a safe manner and prevent extensive thermal exposure to the clamps, load cell, and surrounding instruments. The timer for the high-temperature exposure is started from this point. The initial crosshead distance remained the same and the rest of the test was conducted with the MTS software at the 90-second exposure time. The time was based on calculations completed in Equation 3.2-4 - Equation 4.3-4 [4]. This ensures the specimen reached the required temperature at the time of the test.

For testing at lower temperatures, an air-sourced cooling system was used to reduce the temperature in the environmental chamber. In this instance, the clamping procedure, and distances remained the same. The environmental chamber was then filled with the correct air temperature. Once this air temperature was reached, a soaking time of 90 seconds was used before executing the remainder of the test procedure. The test matrix can be seen in Table 4.3-1.

Name of Specimen	Temperature at the time of the test	Specimen time in the environment before the test	Strain Rate
Q0-A	0°C	90s	0.03 s^{-1}
Q0-B	0°C	90s	0.03 s^{-1}
Q0-C	0°C	90s	0.03 s^{-1}
QRT-A	23°C	-	0.03 s^{-1}
QRT-B	23°C	-	0.03 s^{-1}
QRT-C	23°C	-	0.03 s^{-1}
Q100-A	100°C	90s	0.03 s^{-1}
Q100-B	100°C	90s	0.03 s^{-1}
Q100-C	100°C	90s	0.03 s^{-1}
Q200-A	200°C	90s	0.03 s^{-1}
Q200-B	200°C	90s	0.03 s^{-1}
Q200-C	200°C	90s	0.03 s^{-1}
Q300-A	300°C	90s	0.03 s^{-1}
Q300-B	300°C	90s	0.03 s^{-1}
Q300-C	300°C	90s	0.03 s^{-1}

Table 4.3-1: Test matrix for variable temperature quasistatic tensile testing

4.3.2.1 Tensile Data

The MTS retrieves data as a function of crosshead (mm), load (Newtons), and time (seconds). Using this information, the following formulas can be used to calculate the stress and engineering strain in each measurement after the test.

$$\varepsilon = \frac{\Delta L}{L} \qquad \textit{Equation 4.3-5}$$

$$\sigma = \frac{F}{A} \qquad \textit{Equation 4.3-6}$$

Where:

σ = Engineering stress

ε = Engineering strain

L = Initial gauge length

ΔL = Change in length

F = Applied force

A = Cross-sectional area of specimen

4.4 Results and Discussion

4.4.1 Quasistatic Tensile Testing Stress-Strain Curves

This test displays the stress-strain curve of the room temperature tensile test that was performed. It is key to note the ultimate strength of this curve was measured at 1600 MPa. This curve serves as a reference in the comparison that will be seen between high and lower temperature tests. Figure 4-4 represents the general material properties drawn from a stress-strain curve. Each of these items can help to analyze and understand the material's response under different tensile stress conditions.

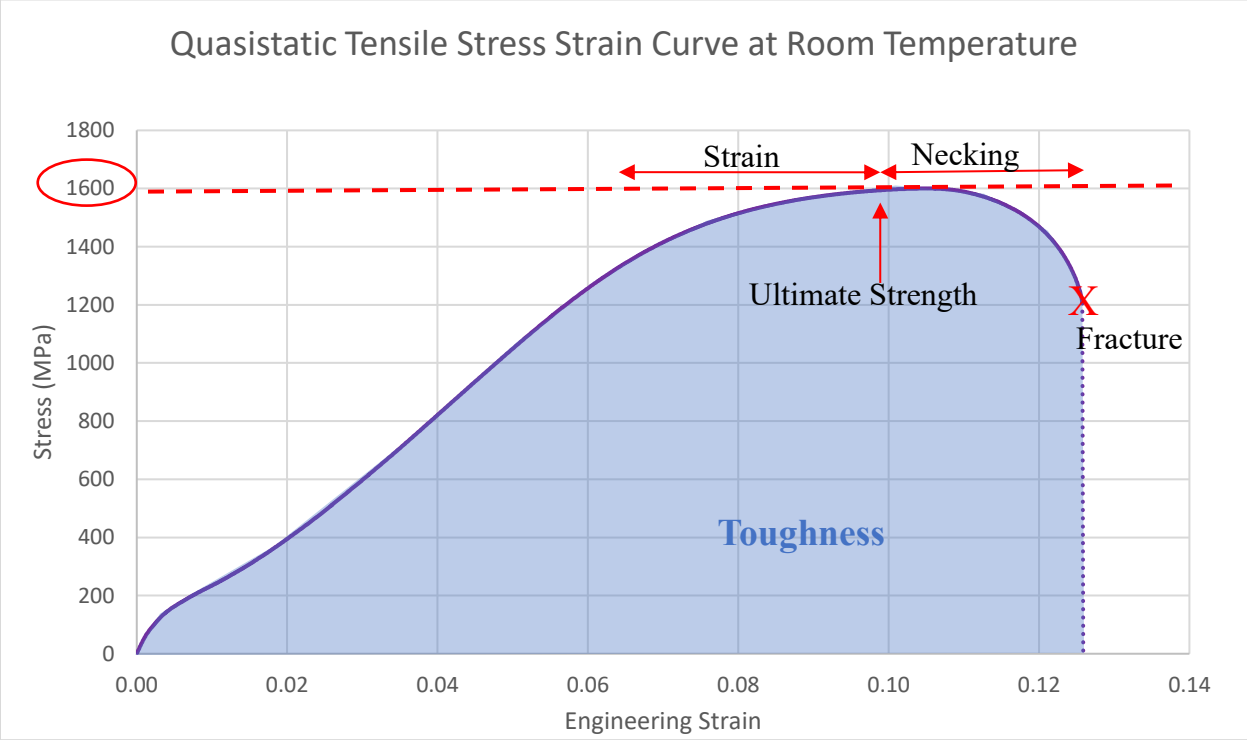

Figure 4-4: Quasistatic Tensile Stress-Strain Curve at Room Temperature (sample Q100-C)

Looking at Figure 4-5, it is seen that there are several distinct observations as the temperature of the material increased. At 100°C engineering strain in the material is significantly increased as seen in most materials under heated conditions. The ultimate tensile strength, however, remains the same as it did at room temperature. This condition is also seen with the 200°C temperature test which exceeds the 100°C sample in strain, yet has similar ultimate strength. The reason for this

increase in performance can be explained by several factors. Mechanisms such as dislocations and mobility of atoms are thermally activated allowing for more efficient motion. Similarly, the grain boundaries are less restrictive, reducing the likelihood of crack initiation and propagation reducing the risk of embrittlement leading to a higher capacity to absorb energy before fracture and better performance under tensile stresses. Furthermore, it has been stated in several studies that the thermal effects on Armox are not significant under 200°C and the martensitic microstructure of the material is still present due to the temperature not being high enough to trigger the diffusion of alloying elements which is why the ultimate strength was not reduced in the 100°C and 200°C tests.

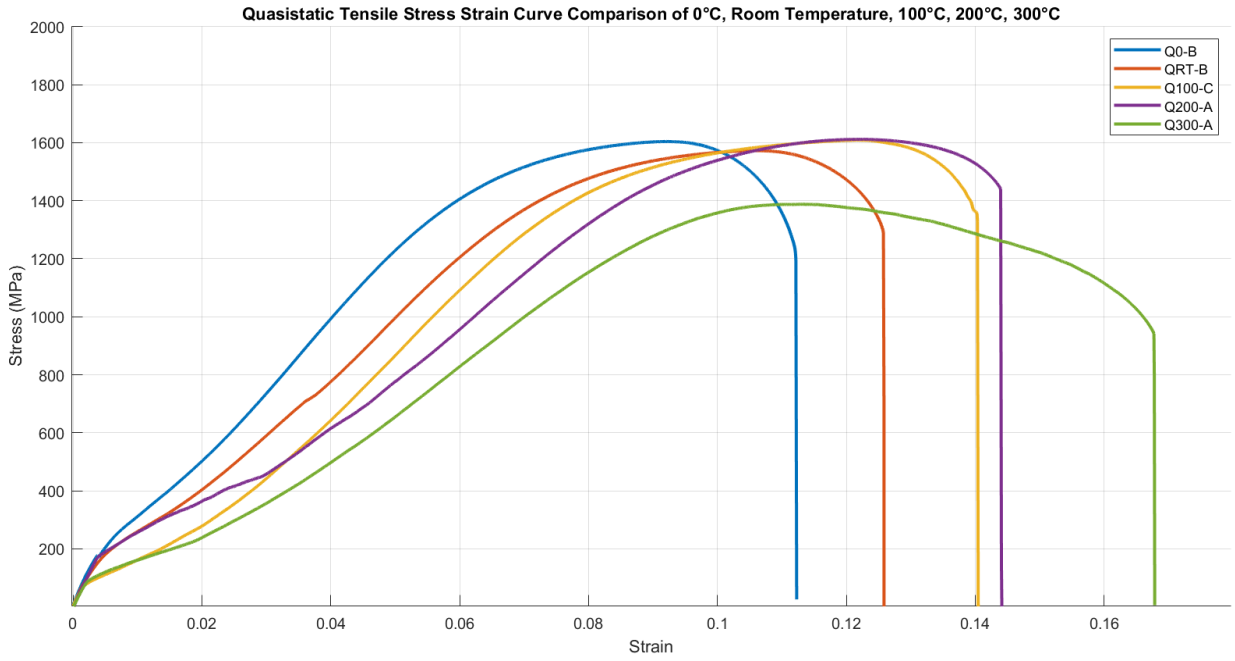

Figure 4-5: Quasistatic Tensile Stress-Strain Curve Comparison of 0°C, Room Temperature, 100°C, 200°C, and 300°C in samples Q0-B, QRT-C, Q100-C, Q200-A, and Q300-A respectively

Once the material undergoes exposure to 300°C, the material was able to be strained significantly more, particularly in its necking phase indicating high ductility features in the sample. Similar to the 100°C and 200°C tests, the increased ductility is a result of thermally activated mechanisms and resulted in higher toughness. The ultimate strength, however, is significantly reduced,

demonstrating signs of microstructural changes affecting the performance of the material. This includes the recrystallization in the microstructure leading to the diffusion of alloying elements such as carbon which gives the material its strength and hardness properties. Without the presence of the quenched, martensitic features in the Armox, the performance of the material is significantly reduced in its overall performance in quasistatic testing conditions. It is important to note that only one successful test was conducted for the 300°C criteria due to concerns regarding damage to the equipment and general safety.

From Figure 4-6, it is seen that the performance is reduced when exposed to colder temperatures. The ultimate strength remains similar; however, the strain hardening became more pronounced, leading to a rapid increase in material hardness and reduced ductility which is why the necking period is slightly shorter and the fracture occurs at a much lower strain. This is possible due to the fact that at low temperatures, grain boundaries may act as barriers to dislocation motion, leading to localized stress concentrations and crack initiation. This resulted in a reduced average toughness of 11.8% compared to room temperature.

Both Figure 4-6 and Table 4.4-1 demonstrate the repeatability of the testing conducted in this chapter. Three tests were conducted for each temperature according to the test matrix. This figure and the averaged data show general consistency and reliability in the testing results.

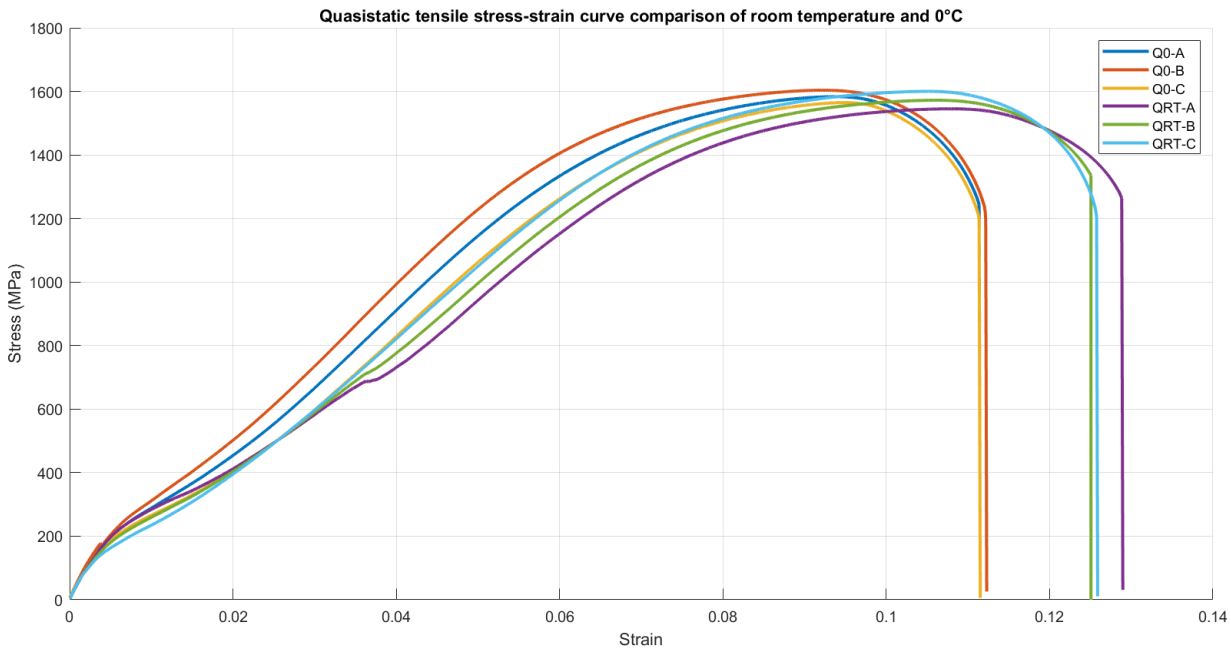

Figure 4-6: Quasistatic tensile stress-strain curve comparison of room temperature and 0°C with samples Q0-A, Q0-B, Q0-C, QRT-A, QRT-B, and QRT-C respectively

Temperature (°C)	**Strain rate (s^{-1})**	**Ultimate Strength (MPa) (Average ± STD)**	**Toughness (J/m^3) (Average ± STD)**	**Engineering strain (Average ± STD)**
0	0.03	1584.1 ± 15.94	119.06 ± 4.7	0.1118 ± 0.00037
23	0.03	1572.6 ± 22.45	134.60 ± 1.5	0.1266 ± 0.0017
100	0.03	1637.21 ± 23.46	149.43 ± 1.2	0.1390 ± 0.0011
200	0.03	1611.82 ± 0.607	155.89 ± 6.8	0.1457 ± 0.0031
300	0.03	1387.75 ± 0	155.60 ± 0	0.1679 ± 0

Table 4.4-1: Variable temperature quasistatic tensile testing results average summary

Comparing toughness across all temperatures, it was shown that the toughness progressively increased as the temperature was raised as shown in Figure 4-7. It is important to note that that although the toughness is very high for 300°C, the maximum stress of the material was compromised and was lower than all other samples which can be seen in Figure 4-8. It was also seen that both the maximum stress and toughness were higher at 100°C and 200°C. This is an indicator of increased performance and material properties.

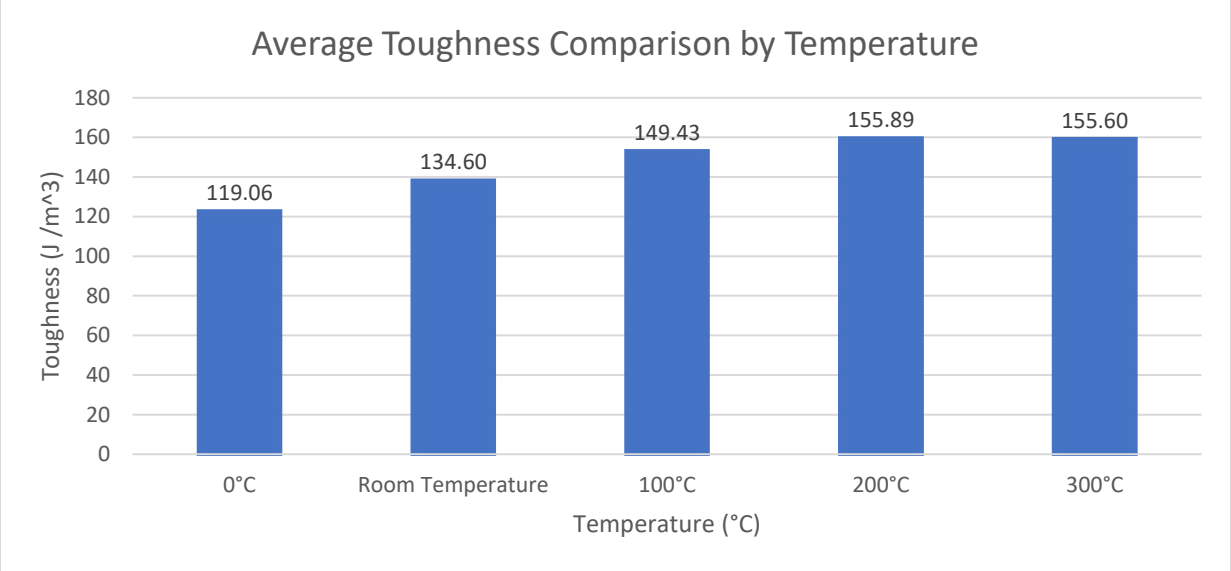

Figure 4-7: Toughness comparison by temperature

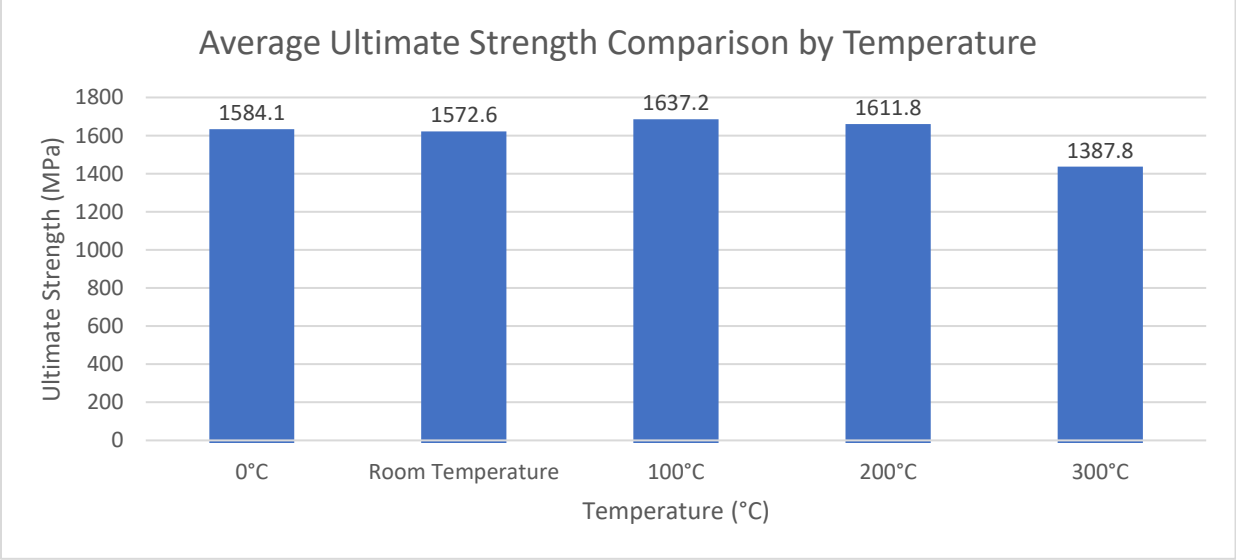

Figure 4-8: Maximum stress comparison by temperature

4.4.2 Quasistatic Tensile Testing Macroscopic Imaging

The tensile deformation that takes place in each of the temperature conditions demonstrated distinct material characteristics. At 0°C the fracture occurs at lower strain and depicts high brittleness in Figure 4-9. The necking is minimal and the fracture surface of the material is very blunt. At room temperature and 100°C (shown in Figure 4-10 and Figure 4-11 respectively), there was an increase in strain and the necking region is larger. The fracture surface of the material also shows greater elongation and ductile features. This trend would continue at 200°C where the material becomes significantly more ductile with a very large fracture surface area and heavy elongation as seen in Figure 4-12. At 300°C, the fracture region has a very heavy localized necking and irregular plugging (cup and cone) shape seen in Figure 4-13. This indicates extreme levels of ductility and a change in the material`s fracture mechanism compared to other temperatures. These results were averaged for each temperature and summarized in Table 4.4-1 below.

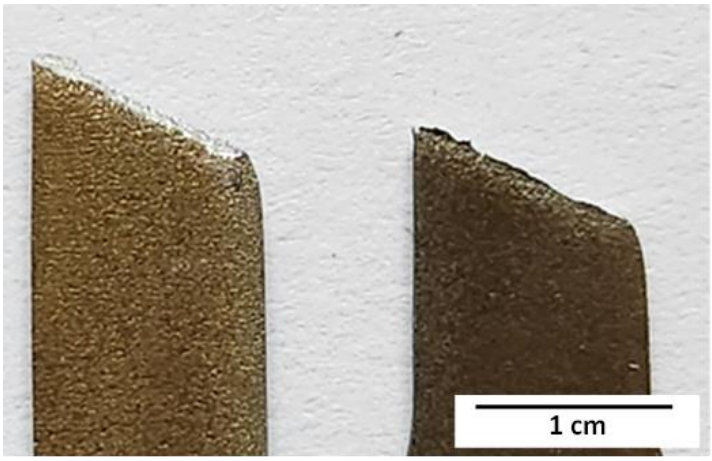

Figure 4-9: Quasistatic tensile test 0°C fracture sample Q0-A

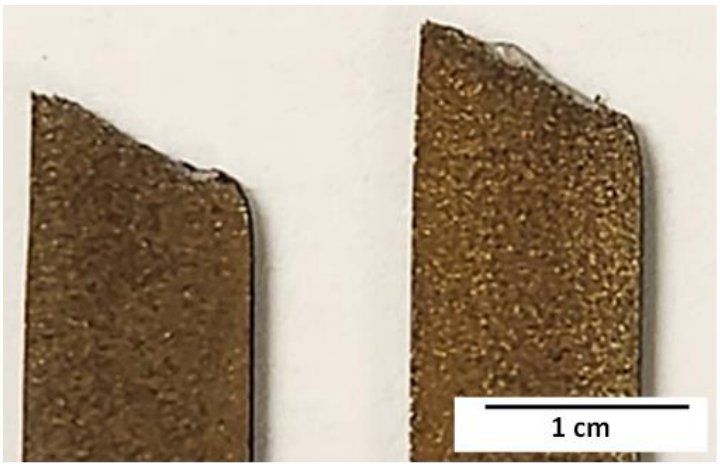

Figure 4-10: Quasistatic tensile test 23°C fracture sample QRT-C

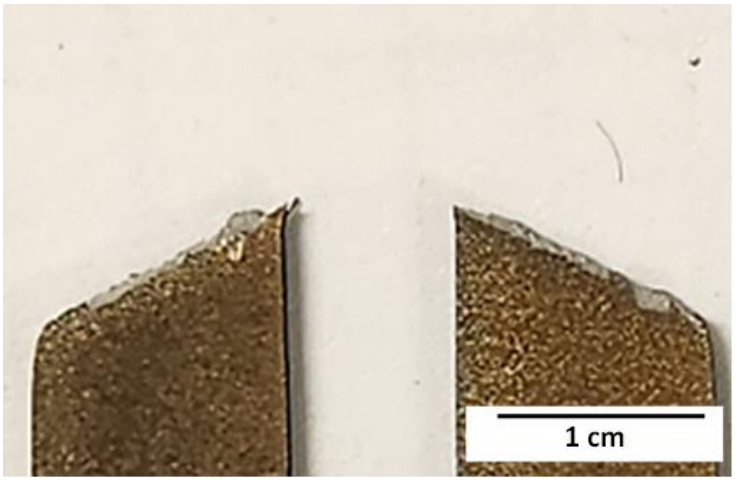

Figure 4-11: Quasistatic tensile test 100°C fracture sample Q100-B

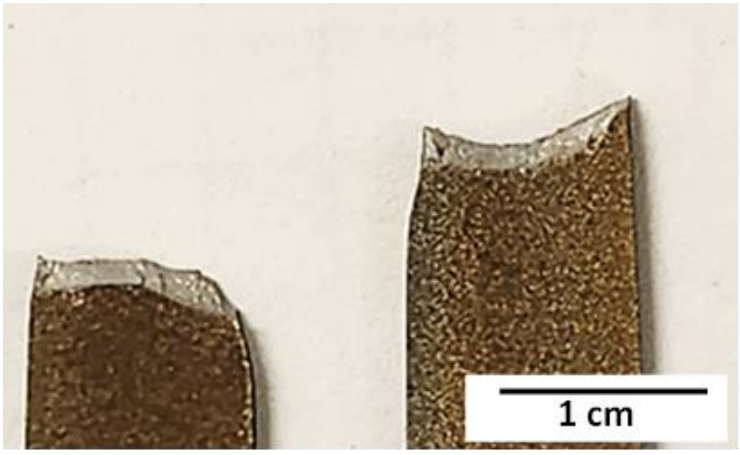

Figure 4-12: Quasistatic tensile test 200°C fracture sample Q200-A

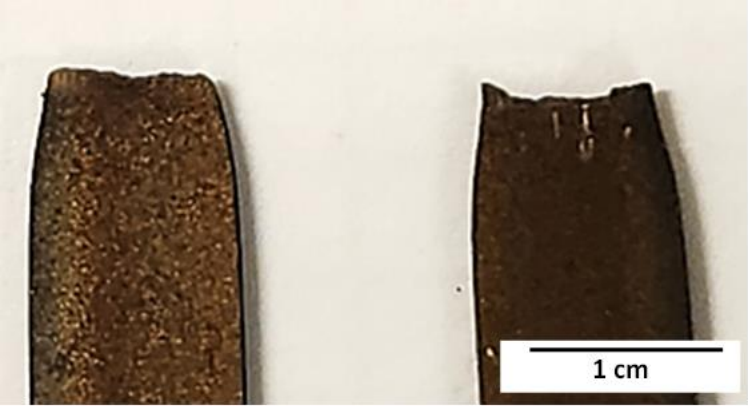

Figure 4-13: Quasistatic tensile test 300°C fracture sample Q300-A

Macroscopic images of each sample were taken and the fracture angles were analyzed using a software called ImageJ. It was observed that many of the samples fractured on a large angle. The reason that tensile samples fracture in this manner is because the resolved shear stress is at its maximum at roughly a 45° angle [9]. Microstructurally, the ductility of the steel allows for it to undergo plastic deformation, and therefore, slip. Slip occurs in the crystallographic planes where the shear stress is highest. Necking of the material can have a significant effect on this angle due to an increased stress region being introduced, thus, shortening the thickness or path of resistance in the material [10]. This phenomenon can be explained using the following Equation 4.4-1 based on the diagram in Figure 4-15 [9]. This was reflected in the fracturing nature of the samples as the highly tough steel at room temperature failed in a 65° orientation across its width with some localized necking. At lowered temperature, there was little necking seen at all through the thickness of the specimen. Once the temperature was increased to 100°C, necking at a 65° angle was seen indicating higher ductility properties in the material. As this temperature increased to 200°C, this angle became smaller and the deformation more severe, again indicating greater ductility. At 300°C the Armox 500T showed extreme ductility in the form of symmetrical plugging, reflecting high levels of softening.

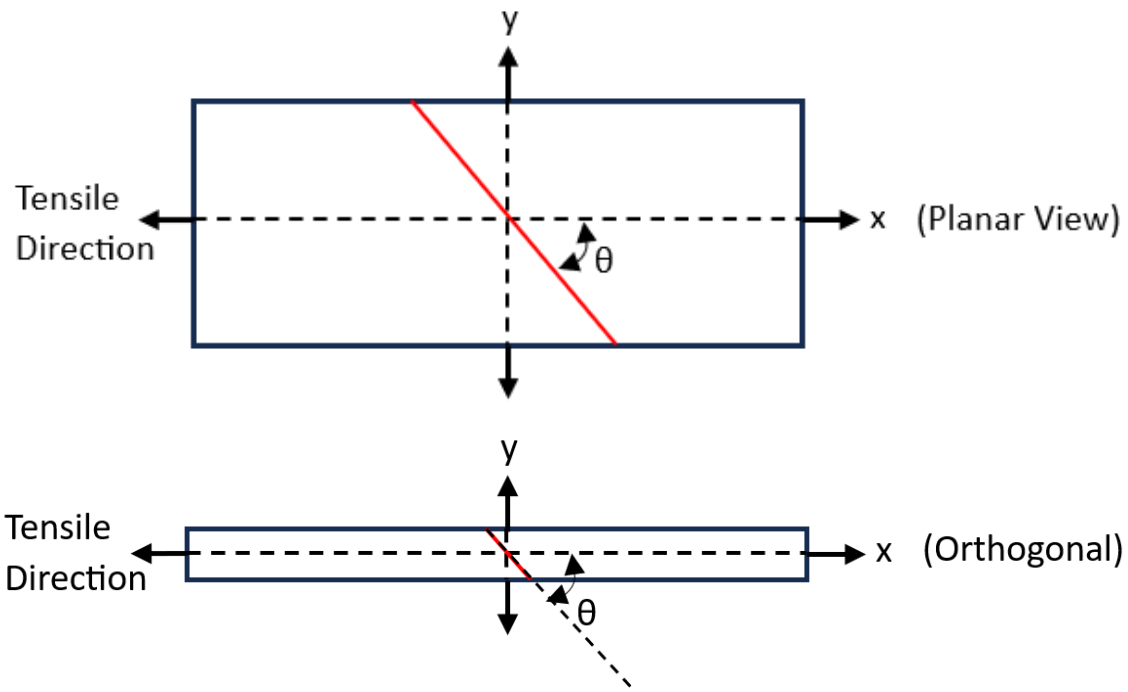

Figure 4-14: Schematic of gauge section of fractured quasistatic tensile specimen [11]

Samples	Fracture Orientation		Symmetry (xyz plane)
	Across width	Through thickness	
Q0	Θ_1 ~ 60-65°	Very little necking	xy Plane
QRT	Θ_1 ~ 60-65°	Localized necking	None
Q100	Θ_1 ~ 60-65°	Θ_2 ~65-75°	None
Q200	Θ_1 ~ 80-85° with U-shape	Θ_2 ~35-45°	None
Q300	Θ_1 ~ 90° localized necking	Irregular plugging	xz plane

Table 4.4-2: Quasistatic tensile test fracture characteristics

$$\tau_{\max in-plane} = \sqrt{\left(\frac{\sigma_x + \sigma_y}{2}\right)^2 + \tau_{xy}^2} \qquad \textit{Equation 4.4-1}$$

Where:

T = maximum in-plane shear stress

σ_x = Stress in x direction

σ_y = Stress in y direction

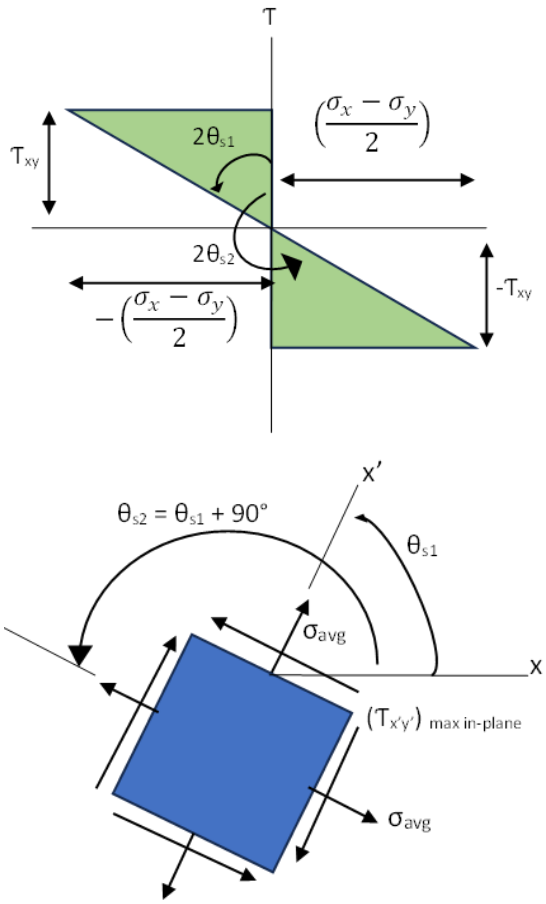

Figure 4-15: Maximum in-plane shear stresses [9]

4.4.3 Fractography Microscopic Images

Several SEM images were taken of the fractured surface of these tensile specimen at different temperatures. Key geographical features to note are dimples and cleavages. Dimples generally represent ductile failure modes and appear to be round and have heavy deformation after failure. This is a result of microscopic voids which form during tensile loading and as the load increases, these voids grow until the ductile limit is reached and the specimen fails by means of separation.

Cleavages generally represent more brittle failures, having a much more flat, sharp, crystalline-like, and jagged appearance. The minimal energy absorption from the material causes a sudden fracture without prior deformation.

Looking at the fracture surface of the 0°C sample (Sample Q0-B) from the SEM imaging in Figure 4-16, specific features in the microstructure were seen. It was apparent that there were several cleavage regions within the microstructure, with a small presence of dimples, indicating there were some ductile mechanisms involved while having a significant accompanying brittle failure.

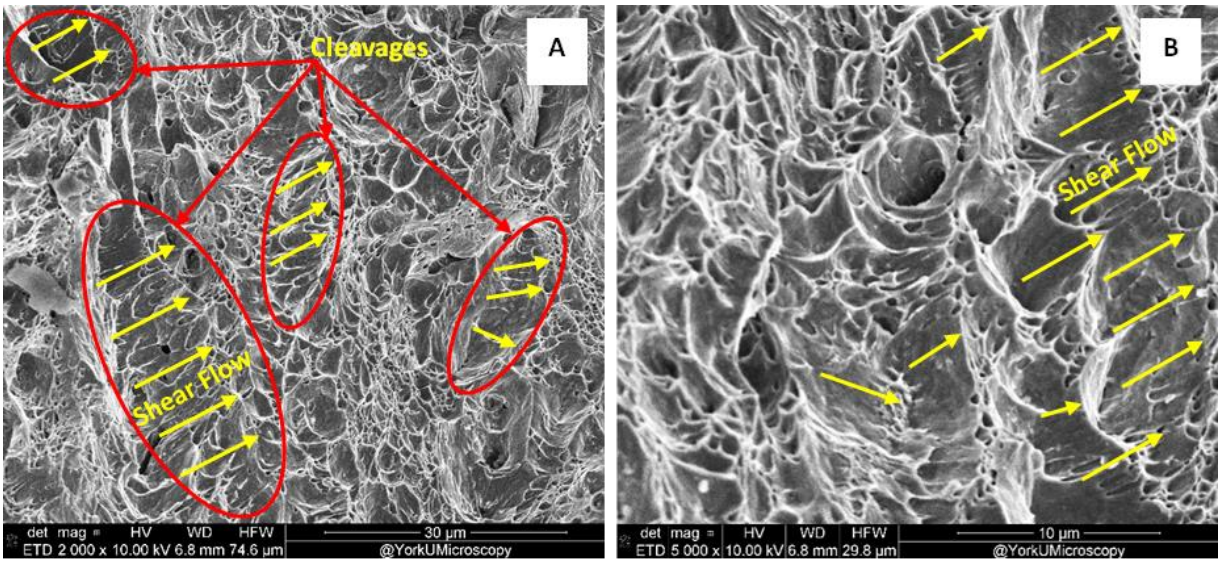

Figure 4-16: SEM images of sample Q0-B: 0°C temperature fracture surface showing cleavages at 2000x magnification (A) and 5000x magnification (B)

Compared to the room temperature sample (QRT-C) in Figure 4-17, it was seen that the presence of dimples was increased while still having some remaining presence of cleavages.

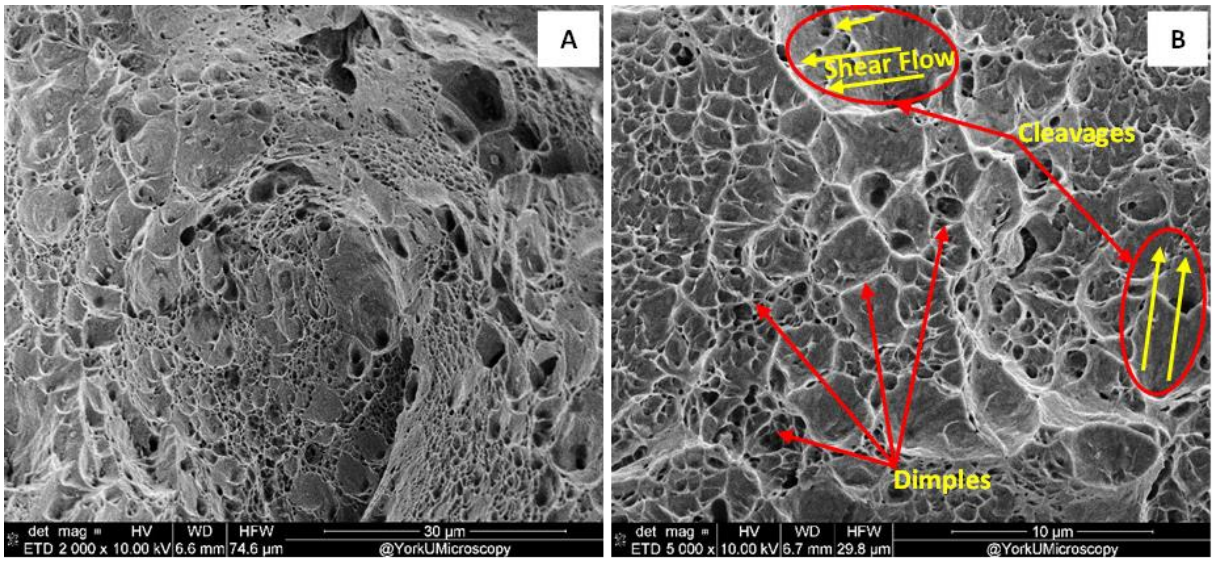

Figure 4-17: SEM images of sample QRT-C: Room temperature fracture surface showing cleavages and dimples at 2000x magnification (A) and 5000x magnification (B)

However, looking at the elevated temperature samples, there was almost no evidence of cleavage regions visible and a very high presence of dimples. Furthermore, it was seen that the size of these dimples increased as the operating temperature of the specimen was increased, indicating grain growth, and ultimately higher ductility movement in the fracture surface. This can be seen in the 100°C sample (Q100-B) in Figure 4-18 where there were both large and small groups of dimples. Figure 4-19 shows the 200°C and 300°C samples (Q200-A and Q300-A respectively), these dimples appear to be larger and more evenly distributed, demonstrating a more uniform stress distribution.

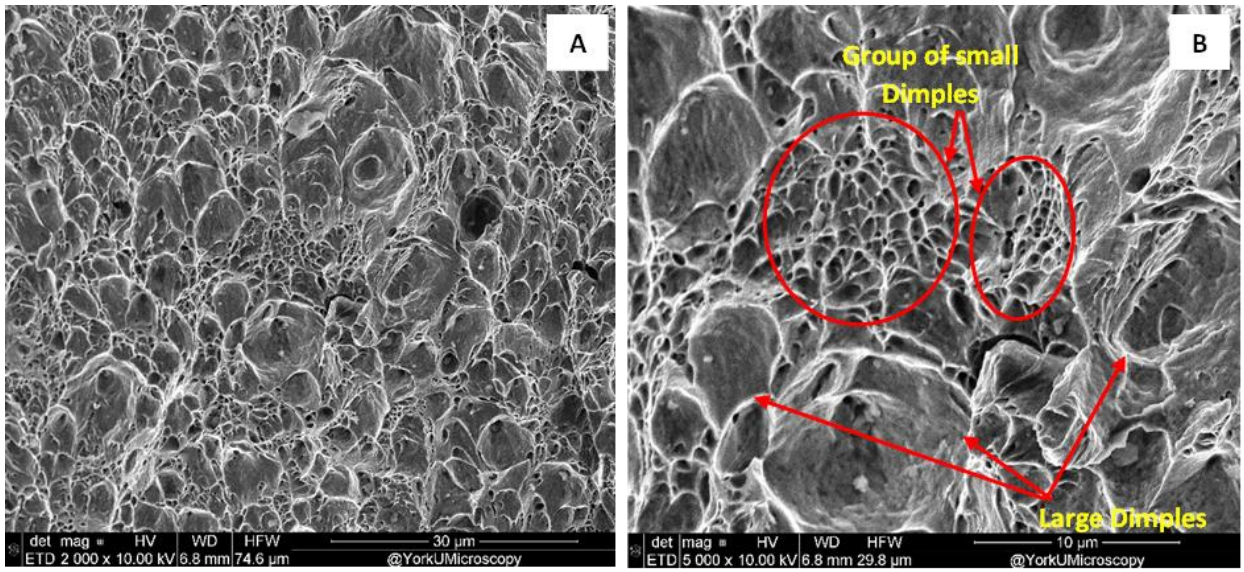

Figure 4-18: SEM images of sample Q100-B: 100°C temperature fracture surface showing clusters of small and large dimples at 2000x magnification (A) and 5000x magnification (B)

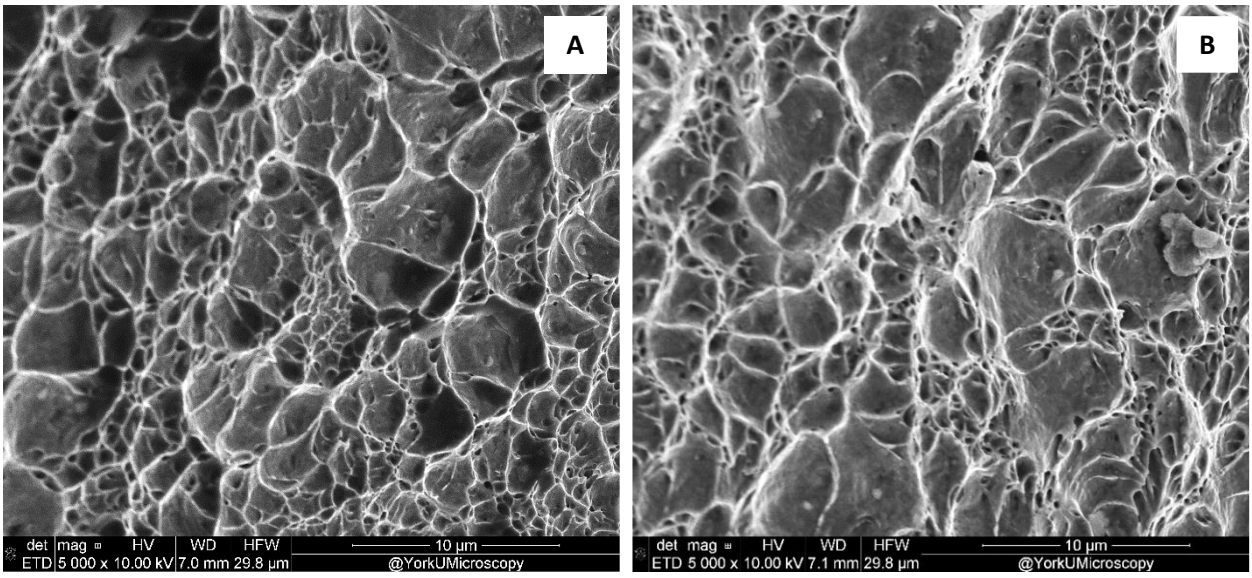

Figure 4-19: SEM images of sample Q200-A (A) (200°C) and Q300-A (B) (300°C) fracture surface showing larger dimples at 5000x magnification

4.5 Conclusion

The performance of Armox in low strain rate tensile conditions is significantly dependent on temperature. An increase in performance was seen at 100°C and 200°C where the toughness of the material increases without compromise, resulting in a 9.7% and 13.4% increase in toughness respectively and approximately a 4% increase in ultimate strength for both. However, once the temperature reaches 300°C, the performance decreases as the ultimate strength was reduced by 11.7%. Even with its large necking and ability to withstand large strains, the initial material properties are compromised and no longer hold its original intended features at this temperature. These features were also reflected in the macroscopic imaging analysis where the higher-temperature samples demonstrated greater necking and deformation. Below room temperature conditions, it was seen that the performance of this material was reduced. At 0°C, the temperature did not affect its ultimate strength significantly, however, it did affect its yield strength, strain hardening, and necking to be much smaller, leading to an earlier and more brittle fracture at a lower

strain. Its overall performance at reduced temperatures was severely affected, specifically in the toughness of Armox 500T, reducing it by 11.8%.

Fractography confirms what is reflected in the data and graphs. The 0°C sample demonstrates a more brittle nature of failure, which explains the premature fracture compared to the room temperature testing. When increased to 100°C and 200°C, a more ductile nature of fracture was seen from the fracture surface, enough to allow for the material to be strained more without compromising the strength. At 300°C however, the extreme softness and ductility features compromised the material strength and resulted in lower performance. Naturally, the environmental temperature exposure of this material would not reach above 200°C, however, in arctic or cold weather conditions, this material would prove to be less effective and have decreased performance.

4.6 References

[1] H. Yu, K. Tieu, C. Lu, X. Liu, Y. Lou, A. Godbole and C. Kong, "Tensile fracture of ultrafine grained aluminum 6061 sheets by asymmetric cryorolling for microforming," *International Journal of Damage Mechanics,* vol. 23, no. 8, pp. 1077-1095, 2014.

[2] A. Popławski, . P. Kędzierski and A. Morka, "Identification of Armox 500T steel failure properties in the modeling of perforation problems," *Materials & Design,* vol. 190, 2020.

[3] A. Saxena, "Experimental and Numerical Investigation of Quasi-Static (10−3 s−1) Fracture Behavior of Armor Steel," *Arabian Journal for Science and Engineering,* vol. 45, no. 7, 2020.

[4] Y. Göçmen, "A numerical ballistic performance investigation of Armox 500T steel through ductile damage models," *Engineering Fracture Mechanics,* 2023.

[5] ASTM International, "E8/E8M − 22: Standard Test Methods for Tension Testing of Metallic Materials," 2022.

[6] P. Kosky, R. Balmer, W. Keat and G. Wise, "Chapter 14 - Mechanical Engineering," in *Exploring engineering: An introduction to engineering and Design*, 5 ed., Elsevier, Academic Press, 2021, pp. 317-340.

[7] Y. Cengel and A. Ghajar, Heat and Mass Transfer: Fundamentals and Applications, Sixth Edition ed., Stillwater, Oklahoma: McGraw-Hill Education , 2020.

[8] E. Yeter, "Damage resistance investigation of Armox 500T and Aluminum 7075 T6 plates subjected to drop-weight and ballistic impact loads," *Sakarya University Journal of Science,* vol. 23, no. 6, pp. 1080-1095, 2019.

[9] G. o. Sweden, "Constitutive model for Armox 500T and Armox 600T at low and medium strain rates," 2003.

[10] A. Kundu and . P. C. Chakraborti, "Effect of strain rate on quasistatic tensile flow behaviour of solution annealed 304 austenitic stainless steel at room temperature," *Journal of Materials Science,* vol. 45, pp. 5482-5489, 2010.

[11] "Strain rate dependent tensile behavior of advanced high strength steels: Experiment and constitutive modeling," *Materials Science and Engineering: A,* vol. 559, pp. 222-231, 2013.

[12] R. Hibbeler, Mechanics of Materials, 10th ed., Pearson Education, 2017.

[13] D. Mateos, "Stress-State and Strain-Rate Dependent Multiscale Characterization of Armox 500T," Toronto, 2023.

[14] B. Hance and T. Link, "Effects of fracture area measurement method and tension test specimen type on fracture strain values of 980 class AHSS," in *International Deep Drawing Research Group 38th Annual Conference*, Troy, 2019.

CHAPTER 5
High Strain Rate Torsion Loading on Armox 500T

5.1 Introduction

Ballistic armours such as Armox 500T are stressed in both high and low strain rate conditions. These conditions are not limited to tensile and compressive forces. In ballistic performance, most guns are prepared with rifled barrels or may have helical tread bullets. This allows the bullets to travel with less drag, resulting in high velocities and distances. It also produces heavy rotation on the projectile reaching 36000-216000 rpm for bullets with 300-800 m/s in linear velocity [1]. For this reason. It is important that this material is able to withstand torsional forces.

By taking a systematic loading approach with increasing strain rates, a stress-strain analysis can be used to determine previously unknown characteristics of Armox 500T in terms of strength, toughness, and ability to absorb energy without compromise. These high strain rates were used to mimic more realistic conditions that low stain rates cannot achieve. This data can then be used for manufacturing and application of the material for ideal performance including high-fidelity FEA, GISSMO modelling, and material characterization.

This Torsional Kolsky Bar testing apparatus was designed and built according to American Society for Metals (ASM) Handbook Torsional Kolsky Bar Testing [2]. This testing procedure has not been conducted on Armox 500T in the past, and thus, serves as preliminary testing to understand the material response under high strain rate torsional forces.

5.2 Methodology

5.2.1 Torsion Specimen

The specimen was obtained from a large piece measuring 76 cm x 76 cm x 3 cm, specifically from an Armox 500T rolled slab. For consistency, all specimen were extracted from the slab's surface using a lathe and a 5-axis cutting Computer Numerical Control (CNC) machine.

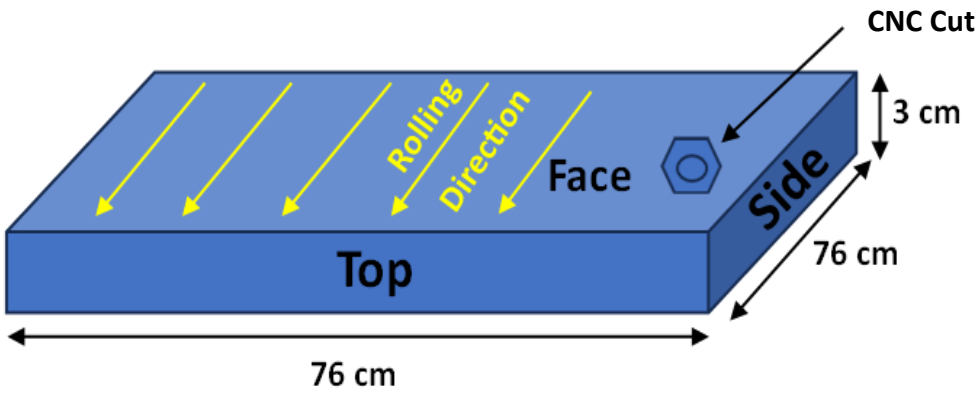

Figure 5-1: As received Armox 500T bulk material size, rolling direction, and CNC cutting surface for torsion specimen

This specimen is based on the American Society for Metals (ASM) Handbook Torsional Kolsky Bar Testing specimen shape [2]. The exact dimensions are based on several other studies using similar apparatus and high-strength steel materials [3] [4].

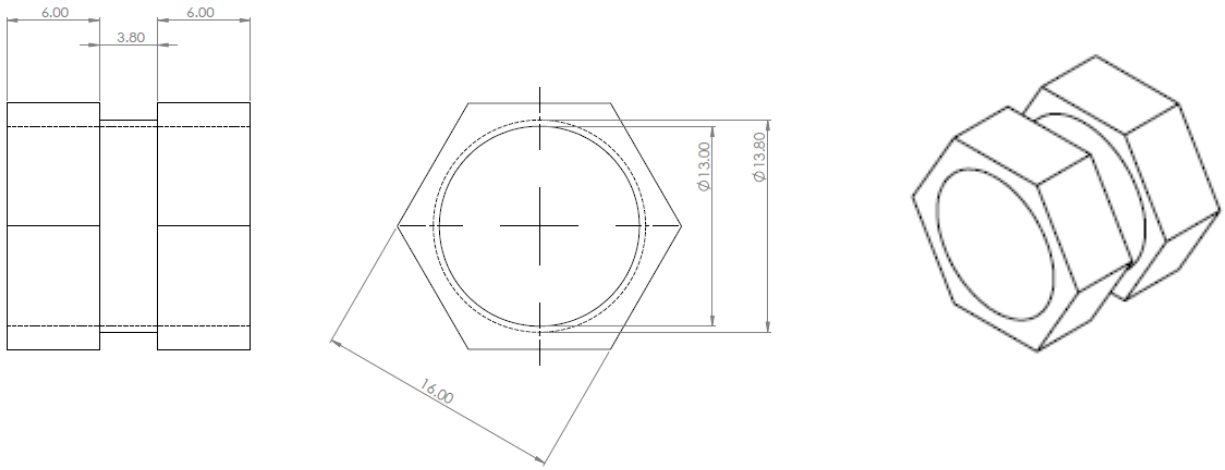

Figure 5-2: Torsion test specimen

5.3 High Strain Rate Torsional Testing

The high strain rate torsional testing was performed using a Torsional Kolsky Bar testing apparatus. This is a well-known reliable technique for testing materials in the range of 10^2 to 10^4 s^{-1} strain rate [5]. By reading the wave propagation through the specimen and the bars, a stress-strain curve can be produced and analyzed to help characterize the material`s features.

A schematic of the Torsional Kolsky Bar can be seen in Figure 5-3. It operates by using two 6 ft long Aluminum 6061 cylindrical bars; the incident and the transmitter bar, both upheld by Teflon bushings to minimize friction during rotation. The specimen (seen in Figure 5-2) used for testing is a thin-walled tube with hexagonal flanges used to secure it between the two bars which have a hexagonal socket on the end faces. A clamp is used to immobilize a section of the transmitter bar. The clamping force is drawn from a forced failure snapping pin secured with an M12-size nut on each end. These nuts are secured with a force of 30 foot-pounds using a torque wrench. This creates enough force to prevent the clamped bar from slipping and prevents the snapping pin from necking or failing. A hydraulic press is then used to crank a lever attached to the transmitter bar, applying torque to the clamped length of the bar (4 ft in length) measured in degrees of twist by a Digi-Pas DWL-200 angle gauge accurate to ±0.1° [6]. To ensure a rapid release of the transmitter bar, the snapping pin with threaded ends has a sharp forced necking region in the center to ensure rapid tensile failure and therefore, rapid release of the clamp on the bar shown in Figure 5-4. To release, the nut is rotated with a torque wrench beyond 30 foot-pounds, applying greater tensile stress on the pin, and forcing it to fracture, resulting in a rapid release of the torqued transmitter bar. This release of torsion generates elastic waves that travel through the specimen and incident bar. The strain gauge on the transmitter bar captures the transmitted waves through the specimen, while the strain gauge on the incident bar captures the incidence and reflected waves.

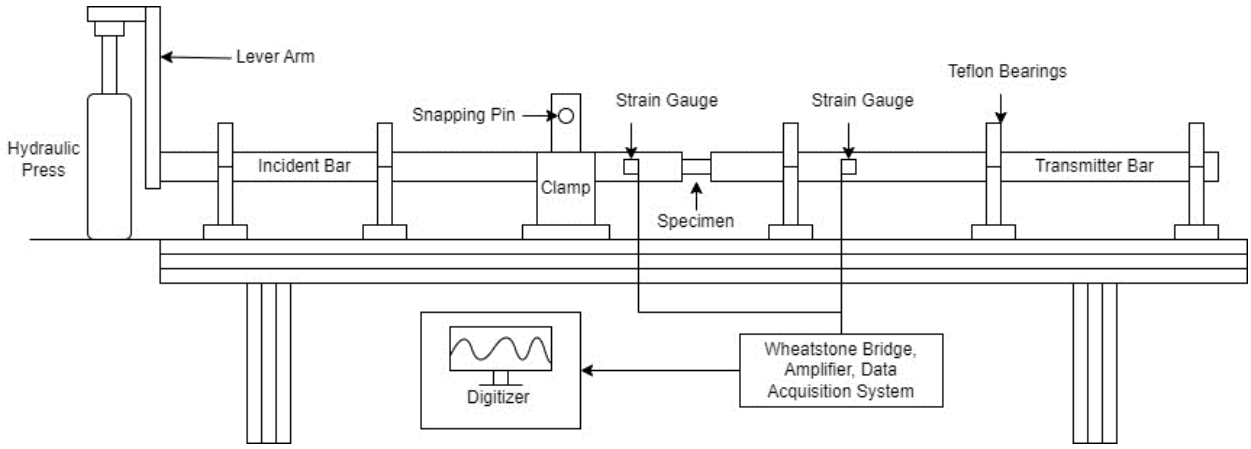

Figure 5-3: Torsional Kolsky Bar testing apparatus diagram

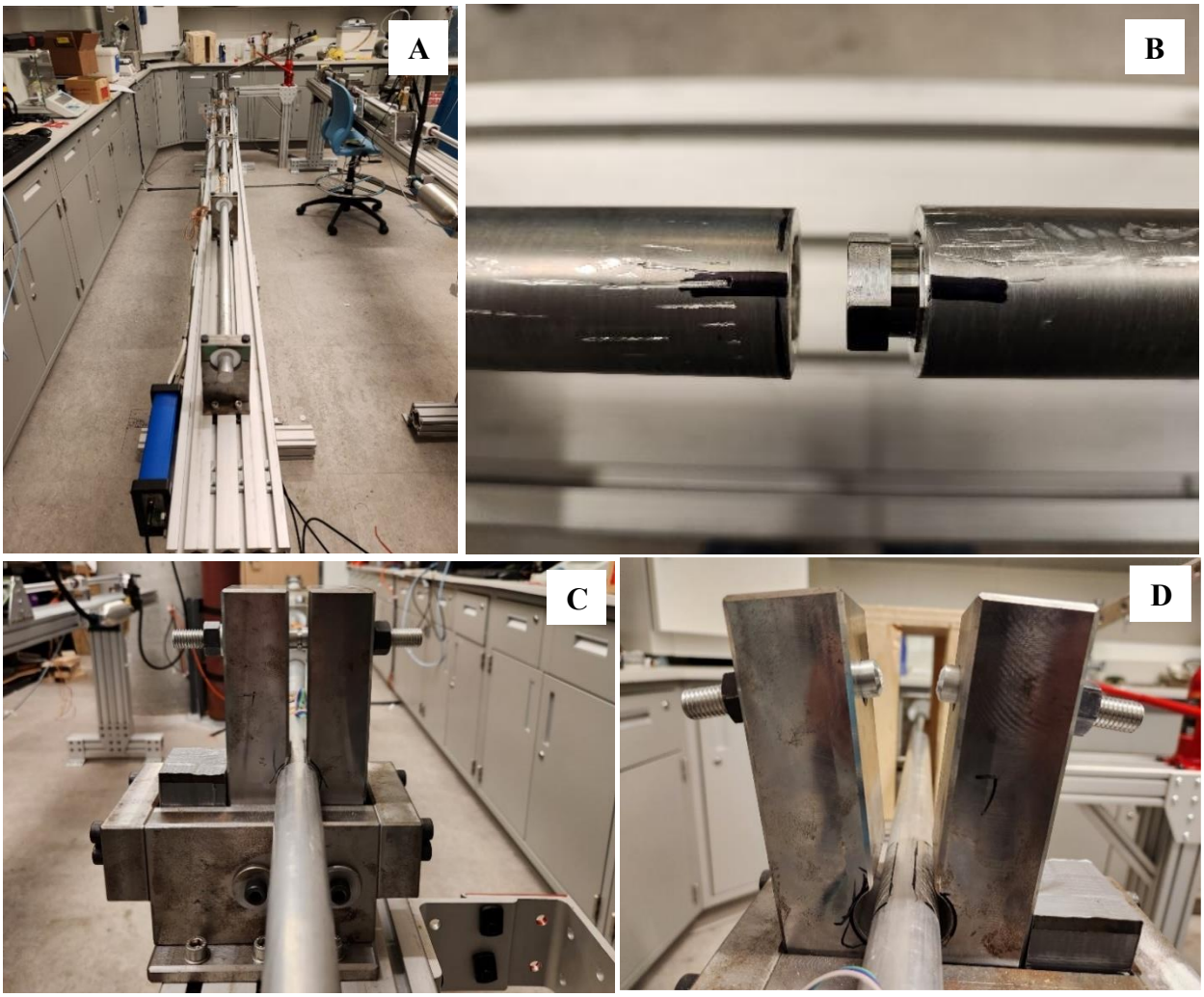

Figure 5-4: Torsional Kolsky Bar setup (A), specimen fitting on the incident bar (B), secured clamp and snapping pin (C), post-test fractured snapping pin (D)

5.3.1 Torsional Data

5.3.1.1 Calibration Procedure

The calibration of the torsion bar was completed by placing a solid hexagonal blank, the same length and width as the specimen, between the incident and the transmitter bar as seen in Figure 5-5. This blank was composed of 6061 Aluminum, which is the same material as the incident and transmitter bars. The transmitter bar is fixed on one end and both bars are loaded under torsion with increasing angles of twist from the other end [3]. The strain gauges set on each bar record the voltage measurements. Using this data, a mathematical relation can be made in the form of a linear plot between shear strain and strength of signal voltage through the following Equation 5.3-1 [3] [7] [8].

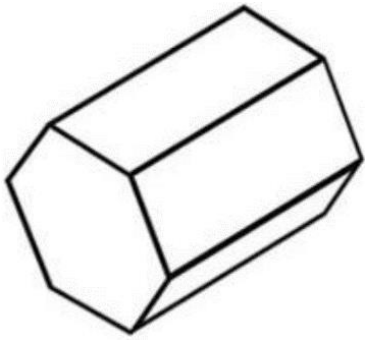

Figure 5-5: Hexagonal blank

$$\gamma_s = \frac{\theta D_b}{2L} \qquad \textit{Equation 5.3-1}$$

θ: Angle of twist in Radians

Db: Diameter of the bar

L: Combined length of the bars

γs: Shear strain

From this, a linear relationship between shear strain and voltage values can be established where the slope of the line gives the multiplication factor to convert the voltage to strain in Figure 5-6.

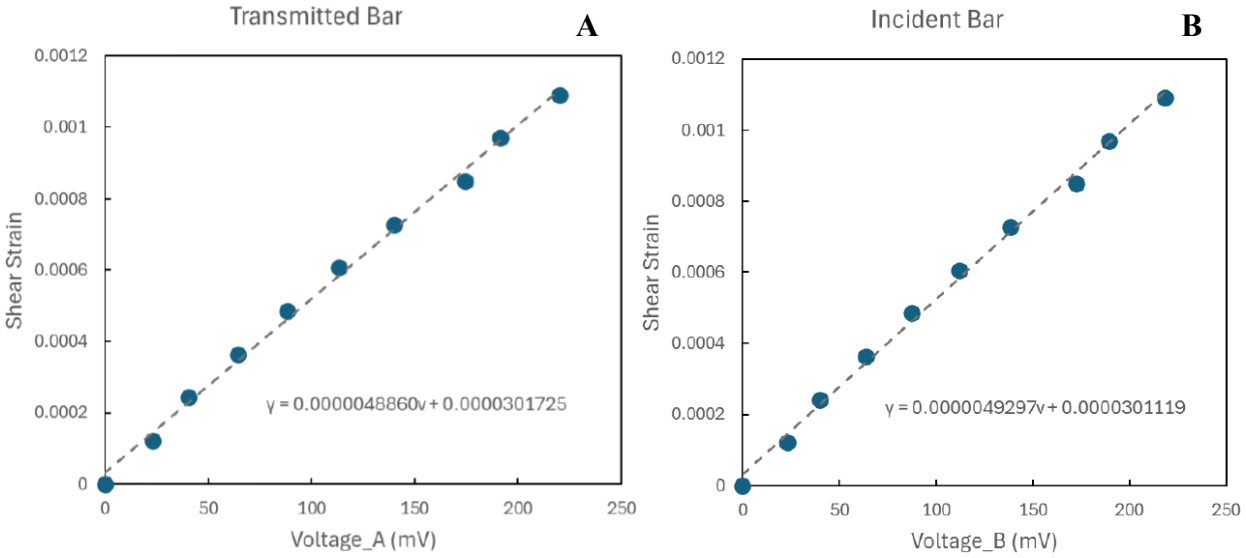

Figure 5-6: Voltage transmitted bar (A) and voltage incident bar (B)

5.3.1.2 Governing equations

Using data from the incident, transmitted, and reflected waves along with other input values, the strain rate, shear strain, and shear stress can be calculated as described in Figure 5-7 and Equation 5.3-2 - Equation 5.3-7 [3] [7] [8].

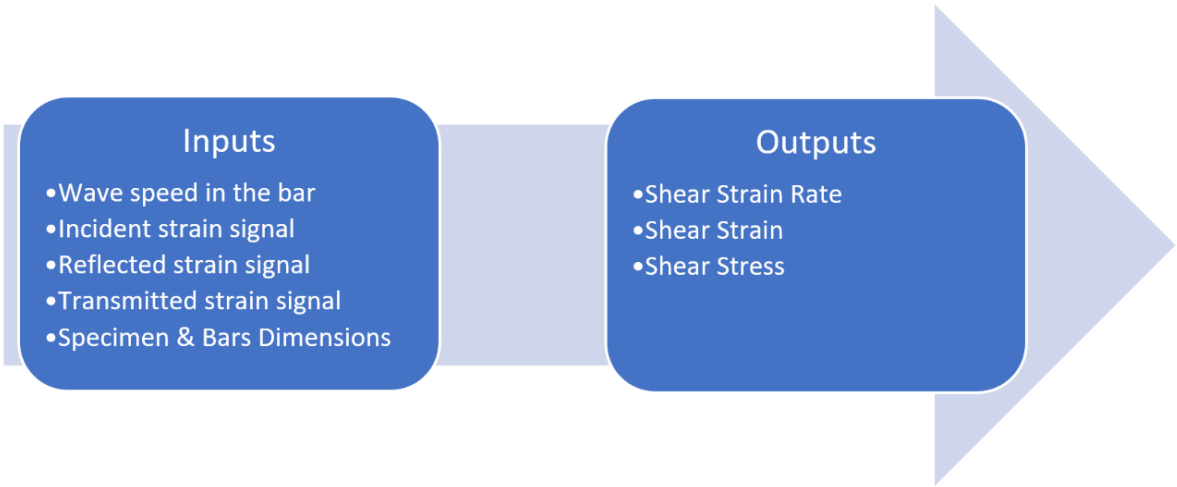

Figure 5-7: Torsion bar inputs versus outputs

Strain Rate	**General Form**	$\dot{\gamma}_s(t) = \frac{CD_s}{L_s D}[\gamma_T(t) - \{\gamma_1(t) - \gamma_R(t)\}]$	Equation 5.3-2
	Simplified Form	$\dot{\gamma}_s(t) = \frac{2CD_s}{L_s D}\gamma_R(t)$	Equation 5.3-3
Shear Strain	**General Form**	$\gamma_s(t) = \frac{C}{L_s}\frac{D_s}{D}\sum[\gamma_T(t) - \{\gamma_1(t) - \gamma_R(t)\}]\Delta t$	Equation 5.3-4
	Simplified Form	$\gamma_s(t) = \frac{2CD_s}{L_s D}\gamma_R(t)\Delta t$	Equation 5.3-5
Shear Stress	**General Form**	$T_{s(t)} = \frac{GD^3(\gamma_1(t) - \{\gamma_R(t) + \gamma_T(t))}{16D_s^2 t_s}\gamma_T$	Equation 5.3-6
	Simplified Form	$T_{s(t)} = \frac{GD^3}{8D_s^2 t_s}\gamma_T$	Equation 5.3-7

5.3.2 Test Matrix

The test matrix was designed such that there are three samples per strain rate (A, B, and C). The angle of torsional loading in the first sample series is 6° and is increased by 2° until the maximum allowable torsional force of the bar is reached (10°). In doing to doing so, an overall characterization of the material behaviour with respect to stress and strain was developed.

Name of Specimen	Temperature at the time of the test	Angle of Twist
TB6-A	23°C	6°
TB6-B	23°C	6°
TB6-C	23°C	6°
TB8-A	23°C	8°
TB8-B	23°C	8°
TB8-C	23°C	8°
TB10-A	23°C	10°
TB10-B	23°C	10°
TB10-C	23°C	10°

Table 5.3-1: Test matrix for Torsional Kolsky Bar

5.4 Results and Discussion

5.4.1 Strain Rate, Shear Strain, and Shear Stress Plots

A standardized method of measuring material behaviour is the use of a stress-strain curve. These curves demonstrate essential properties including the material's elastic region, plastic region, and yield point.

The strain rate was calculated in relation to time as displayed in Figure 5-8. This data demonstrates that the average strain rates of the 6° and 8° samples (neglecting sample TB8-C due to data out of range, deeming it a statistical outlier) were very similar, whereas, in the 10° samples, this significantly increased.

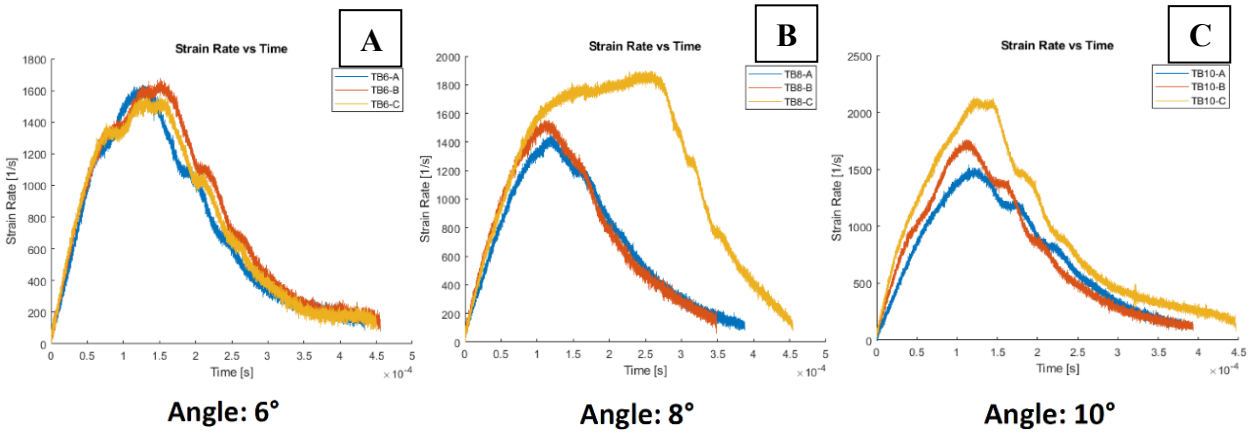

Figure 5-8: Strain rate versus time graph for 6° (A), 8° (B), and 10° (C)

Shear strain versus time was then measured and compared in Figure 5-9, which demonstrated results similar to the strain rate comparison. The shear strain of the overall samples ranged from 0.25-0.4. None of these samples fractured during testing and would likely demonstrate greater values in a larger testing procedure.

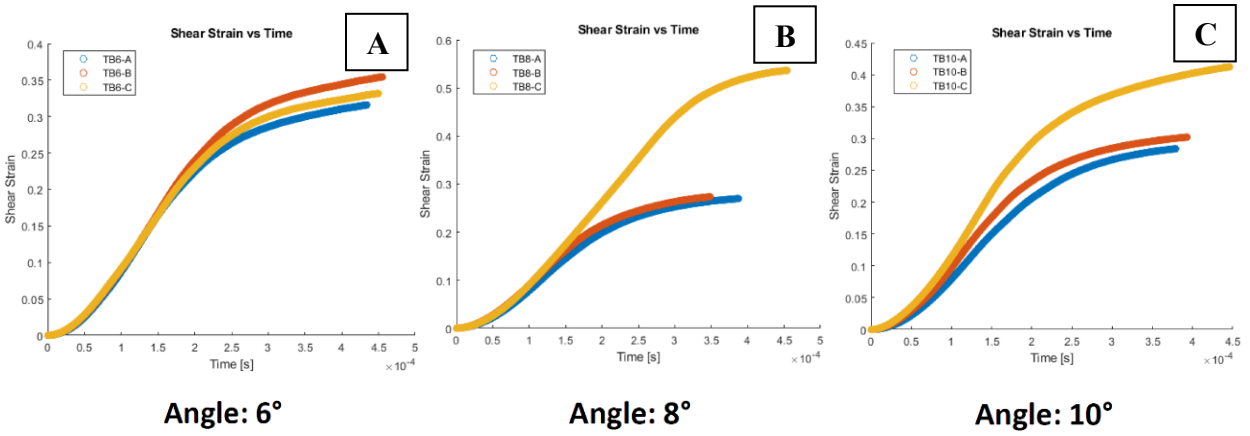

Figure 5-9: Shear strain versus time graph for 6° (A), 8° (B), and 10° (C)

Lastly, the shear stress and shear strain of each set were compared in Figure 5-10. This showed a trend of increasing maximum stress with increasing angles ranging from 700 – 1200 MPa. One aspect that was noticed in this graph was that the 8° angle samples did not display a deload phase, which indicates that the full data set near the end may not have been collected. This would explain why the strain rate and toughness were lower on the 8° samples.

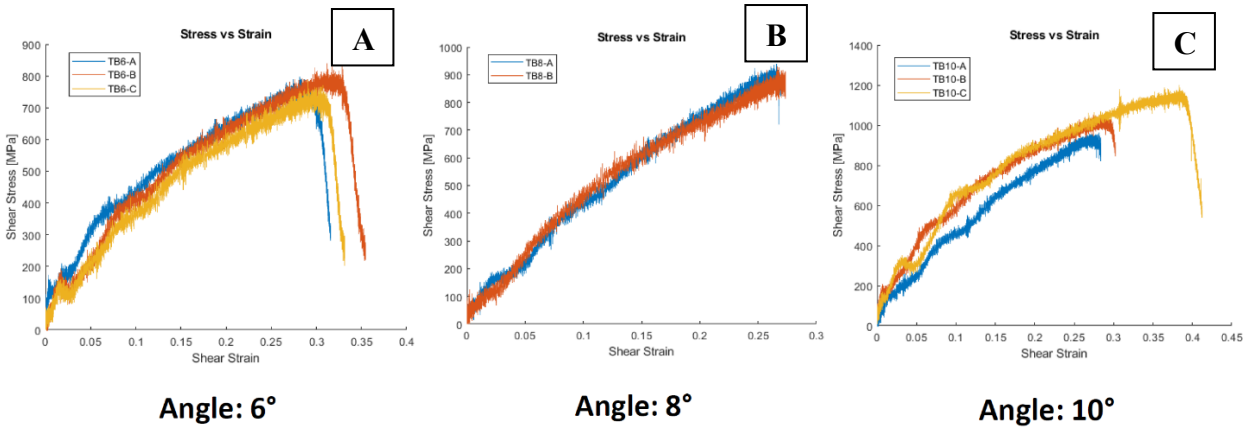

Figure 5-10: Shear stress versus shear strain graph for 6° (A), 8° (B), and 10° (C)

Rotational Angle (°)	Max Shear Stress (MPa) (Average ± STD)	Toughness (J/m^3) (Average ± STD)
6	852.1 ± 7.7	175.0 ± 8.6
8	932.1 ± 33.7	146.0 ± 0.13
10	1105.0 ± 93.9	240.1 ± 67.9

Table 5.4-1: High strain rate torsion testing results and averages summary

5.5 Conclusion

It has been established the initiation of failure and localized stress regions in Armox 500T is critically dependent on the deformation mechanisms of the material. To better understand these mechanisms, it is important to develop a study involving the overall characterization of Armox at increasing strain rates. It was observed in a general trend that the Armox responds to increasing shear strain with increasing angle of twist with a range of 700 – 1200 MPa.

The fracture point was not reached during these experiments and there were no visible signs of plastic deformation or shear bands which limits the investigation and evidence in this study. Nonetheless, this experiment can be used as fundamental data to establish never-before-seen high strain rate torsional characterization of Armox 500T. Further studies into the failure under this type of stress can be achieved through future studies and investigation. This would include the use of more samples, specifically at the 8° stage, as well as thinner wall samples so that plastic deformation and fracture could be studied.

5.6 References

[1] D. Jena, D. Jena and S. Kumar, "Simulation of bullet penetration using finite element method," in *2019 International Conference on Range Technology (ICORT)*, Balasore, 2019.

[2] A. Gilat, "Torsional Kolsky Bar Testing," *Mechanical Testing and Evaluation,* vol. 8, pp. 505-515, 2000.

[3] M. N. Bassim, "Torsional Hopkinson Testing AlgoTuf 400F," in *DRDC Valcartier CR 2011-060*, Winnipeg, 2012.

[4] F. Yazdani, M. Bassim and A. Odeshi, "The formation of adiabatic shear bands in copper during torsion at high strain rates," *Procedia Engineering,* vol. 1, no. 1, pp. 225-228, 2009.

[5] N. Panic, "High Strain Rate Induced Failure in Steels at High Shear Strains," Winnipeg, 1999.

[6] Digi-Pas, "Torpedo Digital Level DWL-200," 2024. [Online]. Available: https://www.digipas.com/product/precision-measurement/torpedo-digital-level/dwl-200.php.

[7] L. Fuentes, J. Gomez-Leon and C. Trujillo , "TORSIONAL SPLIT HOPKINSON BAR OPTIMIZATION," 2012.

[8] A. Gilat, "Torsional Kolsky Bar Testing," *ASM Handbook,* vol. 8, pp. 505-515, 2000.

CHAPTER 6
Conclusion and Future Work

6.1 Conclusion

Through the series of tests and analyses performed, it is evident that the performance of Armox increased in elevated temperatures up to 200°C. This was shown in the high strain rate compression testing where the maximum impact momentum the specimen could withstand without fracturing was 2.0% more than room temperature as well as achieving 2.6% more compression. In the low strain rate tensile testing, there was a 3.7% increase in toughness. This is due to the material microstructure remaining almost entirely intact while also having the ability to have higher ductility features and prevent heavy stress-concentrated areas due to its ability to distribute stresses such as dislocations throughout the specimen more effectively. This was seen in both high-strain-rate compression and low-strain-rate tensile testing. Beyond this temperature, the microstructure of Armox becomes compromised and its intended performance significantly decreases.

If the entire specimen is resting at a higher energy state (heated), then when it is impacted, the stresses are less concentrated on just the ASB region. This is why the ASBs at 200°C were less prevalent than at room temperature where the energy difference between the ASB and non-ASB region is substantial.

The cause of adiabatic shear bands is evidently caused at high strain rates by the development of dislocations, granular changes, phase transformations, and dynamic recrystallization. It is also evident that ASBs are directly related to the mode of ultimate failure in Armox 500T. At these strain rates, the development of adiabatic shear bands begins with high deformation and enlarged grains close to the edge of the material. As the impact momentum is increased, this region becomes heavily concentrated with energy, enough to cause microstructural changes and develop

dislocation-dense regions with voids and porosity within the ASB. This region at further increased strain rates would cause the material to fail through the path of the ASB. These ASBs had increased microhardness, demonstrating a lack of evidence to support thermal softening theories. However, the thermo-mechanical model remains highly important as significant performance changes were seen across all temperatures including at 400°C, where the failed sample showed evidence of heavy brittleness properties and material compromisation with failure at much lower impact momentum.

At lowered temperatures, Armox reveals higher brittleness features and decrease in toughness during low strain rate tensile conditions by 11.8% compared to room temperature samples. Therefore, the use of Armox 500T in low-temperature, polar, or arctic settings poses a greater risk.

6.2 Future Work

With high strain-rate high-temperature compression tests were completed to help characterize and develop modeling of the Armox 500T steel. However, the high strain-rate torsional testing was only conducted in room temperature conditions. This was due to the bar being constructed out of Al 6061, making it unideal for elevated temperatures which would significantly damage the equipment and produce inaccurate data. If the bar was replaced and calibrated with a high-strength material which can withstand these temperatures such as 4340 steel, high strain-rate high-temperature tests could be conducted to retrieve more data and performance properties of Armox 500T.

The high strain rate testing proved to be effective. However, could have been approached differently to provide more conclusive evidence. The high-temperature testing did not allow for the use of a high-speed camera due to logistics, space, and equipment safety. Nonetheless, the room temperature testing could have used a high-speed camera with digital image correlation to allow for live analysis and a deeper understanding of the failure mechanism in the compression

testing. More specifically, a high-speed thermal camera which has the ability to show the rise in temperature and how it specifically affects the failure mode during impact could have been used to better understand the thermal effects on Armox 500T during impact.

The intended use for Armox 500T contains various environments including reduced temperature conditions. This condition is highly untested for Armox 500T and would be useful if the material is to be used in arctic conditions where it is exposed to extremely low temperatures, yet must still perform to its intended standards. For this reason, prolonged low-temperature exposure testing should be performed on Armox to better understand if there are significant changes to the material microstructure. In the interest of performance, the material should also be impacted with a high strain rate to study how it performs under these sub-zero conditions as it may significantly change the use of this product in specific environments.

Lastly, the high strain rate torsional tests did not display any indication of fracture or failure. This is likely due to the wall thickness of the specimen being too high. In future testing, this would be reduced so that the plastic deformation and fracture can be observed in depth. Moreover, the use of Digital Image Correlation (DIC) would be used alongside the strain gauge sensor to depict more accurate and live strain results including failure mode analysis.

Appendix A: DHPB MATLAB Code

```
close all hidden;
clear all;
clc;

set(0,'defaultfigurecolor',[1 1 1])
%% Direct Hopkinson Bar Code - Gurnek Tak

%% Input section
% Samples: RT1-A RT2-B RT3-A RT4-A RT7-B RT8-B RT9-B
VelData = [8.1733 9.033 9.8581 10.8144 12.7221 13.7772 15.6879];
Li = [6.99 6.98 6.96 6.97 6.99 6.98 7.00];
Lf = [6.52 6.42 6.30 6.04 5.76 5.55 5.07];
Di = [6.32 6.30 6.33 6.33 6.28 6.32 6.28];
Df = [6.67 6.65 6.81 6.99 7.18 7.24 7.70];
value = 2;
sro = 0;

%% Import Files
data = cell(ones);
[files,path] = uigetfile('MultiSelect', 'on','*.txt');
if iscell(files)
  for n = 1:length(files)
    data{n} = importdata(fullfile(path,files{n}));
    time0{n} = data{n}(:,1);
    time0{n} = time0{n}-time0{n}(1);
    strain0{n} = data{n}(:,2);
    strain0{n} = strain0{n}-strain0{n}(1);
  end
end
N = length(files); % number of datasets

%% Constants
Cal_Slope = 1000*(19.233+19.59)/2; %N/V = 19.400
K = 140e9; %Bar Bulk Modulus (Pa)
Young = 200e9;
p = 7850; %Bar density (kg/m3)
BarL = 0.18; %Bar length (m)
BarD = 0.0381; %Bar Dia (m)
BarA = pi*(BarD/2)^2;
BarV = BarL*BarA; %Bar Vol (m3)
BarM = BarV*p; %Bar Mass (kg)
C = sqrt(K/p);

%% Filtering
v = 0.3;
r_bar = BarD/2;
fc = (0.3*sqrt(2)*C)/(2*pi*r_bar*v); %cutoff freq Hz
wpass = fc*2*pi; %cutoff freq in rad/s
fs = 2e6;
%Electrical Constants:
fc = (0.3*sqrt(2)*C)/(2*pi*r_bar*v); %cutoff freq for low pass filter (Hz)
fix = 1;
for m=1:N
```

```
    [b, a] = butter(4, fix*fc/(fs/2), 'low');
    strain0{m} = filtfilt(b,a,strain0{m});
end
%% Data Reduction
Clean_strain = cell(N,1);
Clean_time = cell(N,1);

for j=1:N
    % Loading curve
    count = 0;
    cond = 15;
    vecLength = 0;
    time2 = zeros(1);
    strain_V2 = zeros(1);
    time = time0{j};
    strain_V = strain0{j};

    %% Strain Gauge Voltage to Strain via Gauge Factor & Vout/Vin
    GF = 2;
    Vin = 5;
    WB = 1;
    GAIN = 2004;
    Vr = ((strain_V/GAIN)/Vin-(strain_V(1)/GAIN)/Vin);
    BarStrain2 = -2.*Vr./(GF.*(1+2.*Vr));
    BarStrain2 = -(BarStrain2-mean(BarStrain2(1:200)));
    BarStrain2 = BarStrain2(100:end);

    time = time(100:end);
    step1 = 0;
    count2 = 0;
    cond2 = 15;
    vecLength2 = 0;

    for i=2:length(BarStrain2)-1
        a = BarStrain2(i);
        b = BarStrain2(i+1);
        t1 = time(i-1);
        t2 = time(i+1);
        slope(i) = (b-a)/(t2-t1);
        if abs(b)>abs(a)
            count = count+1;
        elseif count >= cond
            count = cond;
        else
            count = 0;
        end
        if count >= cond && abs(a) > 0.00001
            vecLength = vecLength+1;
            strain_V2(vecLength) = BarStrain2(i);
            time2(vecLength) = time(i);
            step1 = 1;
        end
        if length(strain_V2)>=200 && abs(a) <= 0.000005
            break
        end
```

```
    end

    Clean_strain{j} = strain_V2;
    Clean_time{j} = time2-time2(1);
    if abs(max(Clean_strain{j})) < abs(min(Clean_strain{j}))
        Clean_strain{j} = -Clean_strain{j};
    end
end

%% Results and Plotting
%Variable initialization
Force = cell(N,1);
Deformation = cell(N,1);
Sigma = cell(N,1);
Epsilon = cell(N,1);
Yield = ones(N,1);
Ultimate = ones(N,1);
MaxStrain = ones(N,1);
Strain_Y = ones(N,1);
Strain_U = ones(N,1);
StrainRate = ones(N,1);
Toughness = ones(N,1);
MaxStress = ones(N,1);
YoungModulus = ones(N,1);

%Plot initialization
mrkr_freq = 20;
mrk_size = 8;
string = ["o" "x" "v" "d" "*" "^" "+" "^" "s" ">" "<" "square"];

for k=1:N
    L1 = Li(k);
    D1 = Di(k);
    L2 = Lf(k);
    D2 = Df(k);
    V = VelData(k);
    P = BarM*V; %Impact Momentum
    e = (L1-L2)/L1;
    Area = pi*(D1/2)^2;

    if sro == 1
        strainrate = sr(k);

    else
        strainrate = (C/(2*BarL))*e;

    end

%_____________________________________________________________________
% CALCULATE STRAIN AND STRESS AS WELL AS STRAIN RATE FOR FILES HERE
T_overTf = Clean_time{k}./(Clean_time{k}(end));
Strain = log(L1./(L1-((L1-L2).*T_overTf)));

Load = Clean_strain{k}*K*BarA;
stress = ((L1-(L1-L2).*T_overTf).*(Load./(L1*Area)));
```

```
SS = [Strain; stress]';
sigma_t = max(stress);
st_idx = find(stress==sigma_t);
epsilon_t = Strain(st_idx(1));
total_Astrain = Strain(end);
strainrate2 = Strain*C/(2*BarL);
strainrate3 = max(strainrate2);

 % Calculate Toughness
    Toughness(k) = trapz(Strain, stress);

 % Calculate Maximum Stress
    MaxStress(k) = max(stress);

    Force{k} = Load;
    Sigma{k} = stress';
    Epsilon{k} = Strain';
    Ultimate(k) = sigma_t;
    MaxStrain(k) = total_Astrain;
    Strain_U(k) = epsilon_t;
    StrainRate(k) = floor(strainrate);

    fprintf('Dataset%2.0f: \n',k)
    fprintf('Tensile Strength = %2.2f MPa \t Strain at Ultimate Stress = %2.4f
\n',sigma_t,epsilon_t)
    fprintf('Max Major Strain = %2.4f \t          Strain Rate = %2.2f s-1
\n\n',total_Astrain,strainrate)

    fprintf('-------------------------------------------------\n');
    fprintf('Dataset | Tensile Strength | Strain at Ultimate Stress | Max Major Strain
| Toughness | Maximum Stress | Young''s Modulus\n');
    strainrate = floor(strainrate);
    fprintf('-------------------------------------------------\n');

    figure(1)
    hold on
    grid on
    plot(Strain,stress,'DisplayName',strcat('ε̇ = ',num2str(strainrate),' s-1'),...
       'Marker',strcat(string(k)),'MarkerIndices',1:mrkr_freq:length(Strain),...
       'MarkerSize',mrk_size);
    xlabel('True Strain')
    ylabel('Stress (MPa)')
    title('23°C Compression ARMOX 500T - Stress-Strain')
    legend('show')
    hold off

    figure(2)
    hold on
    grid on
    plot(Clean_time{k}*1e6,Force{k}*1e3,...
        'DisplayName',strcat(num2str(StrainRate(k)),' s-1'))
    legend('show')
    xlabel('Time (us)')
    ylabel('Force (kN)')
```

```
    title('23°C Compression ARMOX 500T - Force-time')
    hold off

    figure(3)
    hold on
    grid on
    plot(Strain, stress,'DisplayName',strcat('Dataset ', num2str(k)),...

'Marker',strcat(string(k)),'MarkerIndices',1:mrkr_freq:length(Strain),'MarkerSize',mr
k_size);
    xlabel('True Strain')
    ylabel('Stress (MPa)')
    title('Stress-Strain Curve Comparison')
    legend('show')
    hold off

    fprintf('%8d | %16.2f | %26.4f | %16.4f | %9.2f | %14.2f | %16.2f\n', k, sigma_t,
epsilon_t, total_Astrain, Toughness(k), MaxStress(k), YoungModulus(k) / 1e9);
    fprintf('-----------------------------------------------\n');
end

SSdata0 = [Epsilon Sigma];
max(Load);
f1 = figure(1);
f4 = figure(2);
movegui(f1,[200 -100]);
movegui(f4,[-200 -100]);

figure(4)
hold on
plot(StrainRate,Ultimate,'Marker',strcat(string(2)))
ylabel('Strength (MPa)');
xlabel('Strain Rate (s-1)');
title('Compressive-Shear Strain-Rate Strengthening of ARMOX 500T');
legend('Ultimate Flow Stress');
hold off
```

Appendix B: MTS Data Analysis MATLAB Code

```
close all hidden;
clear all;
clc;

%% Tensile MTS Testing Code - Gurnek Tak

% Define temperature labels corresponding to the order of file selection
temperatureLabels   =   {'Q0-A','Q0-B','Q0-C','QRT-A','QRT-B','QRT-C','Q100-A','Q100-
B','Q100-C','Q200-A','Q200-B','Q200-C','Q300-A', 'Q300-B'};

% Open a dialog to select multiple Excel files
[fileNames, pathName] = uigetfile('*.xlsx', 'Select the files in the order of 0°C, RT,
100°C, 200°C, 300°C', 'MultiSelect', 'on');

% Check if the selection was made
if isequal(fileNames, 0)
    disp('User selected Cancel');
else
    disp(['User selected files.']);

    % Initialize variables to store maximum stress values, toughness values, and
dataset names
    maxStressValues = [];
    toughnessValues = [];
    datasetNames = {};

    % Initialize a figure for the stress-strain plots
    figure;
    hold on; % Allows multiple plots in the same figure

    % Check if fileNames is a cell array (multiple files selected) or a string (single
file)
    if ischar(fileNames)
        % Convert to cell array for consistency if only one file was selected
        fileNames = {fileNames};
    end

    % Ensure that the number of selected files matches the number of labels
    if length(fileNames) ~= length(temperatureLabels)
        error('The number of selected files does not match the number of temperature
labels.');
    end

    % Loop through each selected file
    for k = 1:length(fileNames)
        % Full path to the current file
        filePath = fullfile(pathName, fileNames{k});

        % Import the data from the current Excel file
        dataTable = readtable(filePath);

        % Extract stress and strain data
```

```
        stress = dataTable{:, 2}; % Adjust if your data is in different columns
        strain = dataTable{:, 1}; % Adjust if your data is in different columns

        % Plot the stress-strain graph for the current dataset with the temperature
label
        plot(strain, stress, 'LineWidth', 2, 'DisplayName', temperatureLabels{k});

        % Calculate and store the maximum stress value for the current dataset
        maxStress = max(stress);
        maxStressValues = [maxStressValues, maxStress]; % Append to max stress values

        % Calculate the toughness and store it
        toughness = trapz(strain, stress); % Numerical integration for toughness
        toughnessValues = [toughnessValues, toughness]; % Append to toughness values

        % Use temperature labels for dataset naming
        datasetNames{end+1} = temperatureLabels{k}; % Append dataset name
    end

    % Customize the stress-strain plot
    xlabel('Strain');
    ylabel('Stress (MPa)');
    title('Stress-Strain Graphs by Temperature');
    legend('show');
    grid on;
    hold off;

    % Plot maximum stress comparison
    figure; % New figure for maximum stress comparison
    bar(maxStressValues); % Create a bar graph of maximum stress values
    set(gca, 'xticklabel', datasetNames); % Set x-axis labels to dataset names
    xlabel('Temperature (°C)');
    ylabel('Maximum Stress (MPa)');
    title('Maximum Stress Comparison by Temperature');
    grid on;
    % Add numbers on top of the bars for maximum stress
    for i = 1:length(maxStressValues)
        text(i, maxStressValues(i), num2str(maxStressValues(i), '%.2f'), ...
            'HorizontalAlignment', 'center', 'VerticalAlignment', 'bottom');
    end

    % Plot toughness comparison in a new figure
    figure; % New figure for toughness comparison
    bar(toughnessValues); % Create a bar graph of toughness values
    set(gca, 'xticklabel', datasetNames); % Set x-axis labels to dataset names
    xlabel('Temperature (°C)');
    ylabel('Toughness (J·m^-^3)');
    title('Toughness Comparison by Temperature');
    grid on;
    % Add numbers on top of the bars for toughness
    for i = 1:length(toughnessValues)
        text(i, toughnessValues(i), num2str(toughnessValues(i), '%.2f'), ...
            'HorizontalAlignment', 'center', 'VerticalAlignment', 'bottom');
    end
end
```

Appendix C: Preliminary Thermal Exposure Testing

9.1 Introduction

It is evident that the extreme temperatures effect the microstructure and performance of materials. ASBs are created in areas of high stress concentration and energy which is why there is an increase in temperature in the material after high strain rate impact, particularly in the literature of ballistic impact. This deems it critical to understand the affects of heat exposure alone on the microstructure and composure of the initial properties of the materials.

To understand the independent effects of temperature on the microstructure of Armox, the specimen were exposed to different conditions and analysed microscopically. In this study the unimpacted cylindrical Armox specimen were exposed to 100°C, 200°C, 300°C, 400°C, 500°C, and 600°C in a furnace (Figure C-1) for one hour before being cooled in ambient air conditions. This would replicate different conditions of heat produced by impacting the Armox and its effects on the microstructure of the material in comparison to the original received material. The test matrix can be seen in Table 9.2-1.

Figure C-1: Thermo Scientific Lindberg Blue M furnace used for static high temperature exposure testing

9.2 Test Matrix

Sample	Temperature	Duration	Quenching Method
AR25	25°C	1 Hour	Ambient Air Cooled
AR200	200°C	1 Hour	Ambient Air Cooled
AR300	300°C	1 Hour	Ambient Air Cooled
AR400	400°C	1 Hour	Ambient Air Cooled
AR500	500°C	1 Hour	Ambient Air Cooled
AR600	600°C	1 Hour	Ambient Air Cooled

Table 9.2-1: Test matrix for prolonged temperature exposure testing

9.3 Optical Microscope Imaging: Temperature affects on Armox 500T (unimpacted)

The as received sample shows the lathed random orientation microstructure of Armox. These lathes are large, well defined in high contrast, and come in the form of groups of lathes also referred to as packets. An example of this can be seen in Figure 3-22 and Figure C-2.

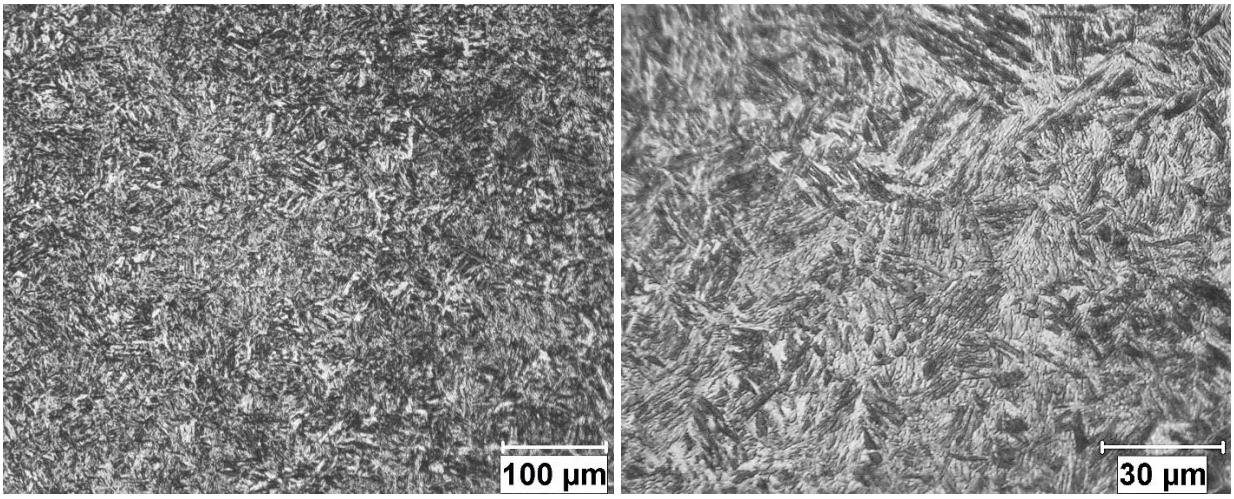

Figure C-2: OM image of Armox as received 100x and 400x magnification

As the temperature is increased to 200°C, these packets begin to lose definition and demonstrate a more homogeneous mixture of elements. At 300°C, the Armox loses its entire lathed microstructure and none of the initial material properties are recognizable with very small grains. These grains appear to be slightly larger at 400°C exposure which indicates a possibility of grain growth with prolonged exposure.

Significant changes to the integrity of the material are significant with exposure to 500°C and 600°C exposures. At 500°C the pits and voids as well as large grain boundaries become present in the material. These features become more enhanced and frequent as the temperature is increased to 600°C.

The increase of temperature alone can affect the microstructure and mechanical properties of Armox 500T. The as the process of diffusion of alloying elements begin, the material also reaches a static recrystallization temperature which further relieves the material of its quenched hardness properties. Below is a series of figures demonstrating these effects in Figure C-3 - Figure C-7.

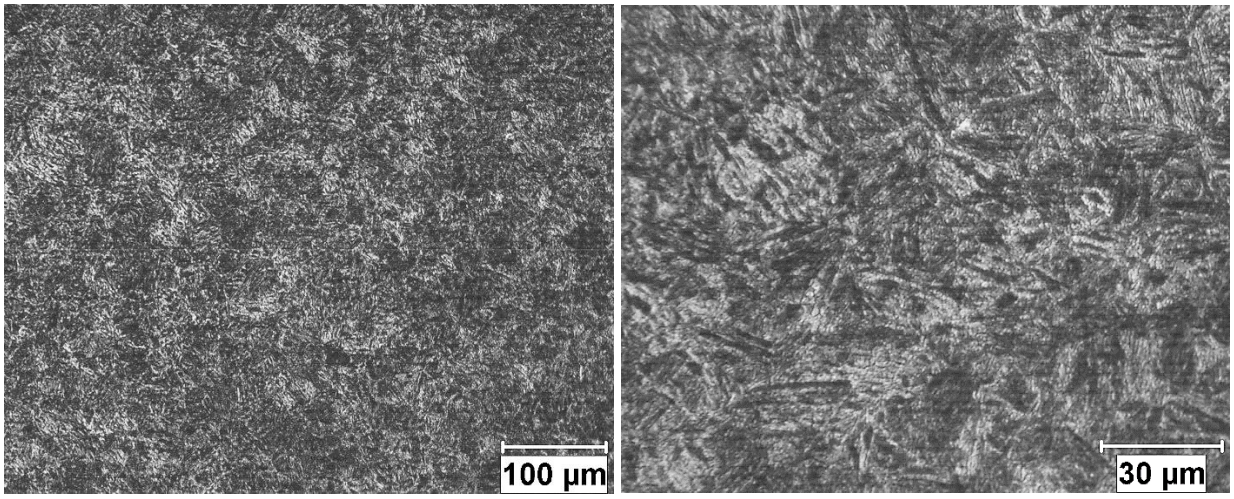

Figure C-3: OM image of Armox 200°C (1 hour exposure, unimpacted) 100x and 400x magnification respectively

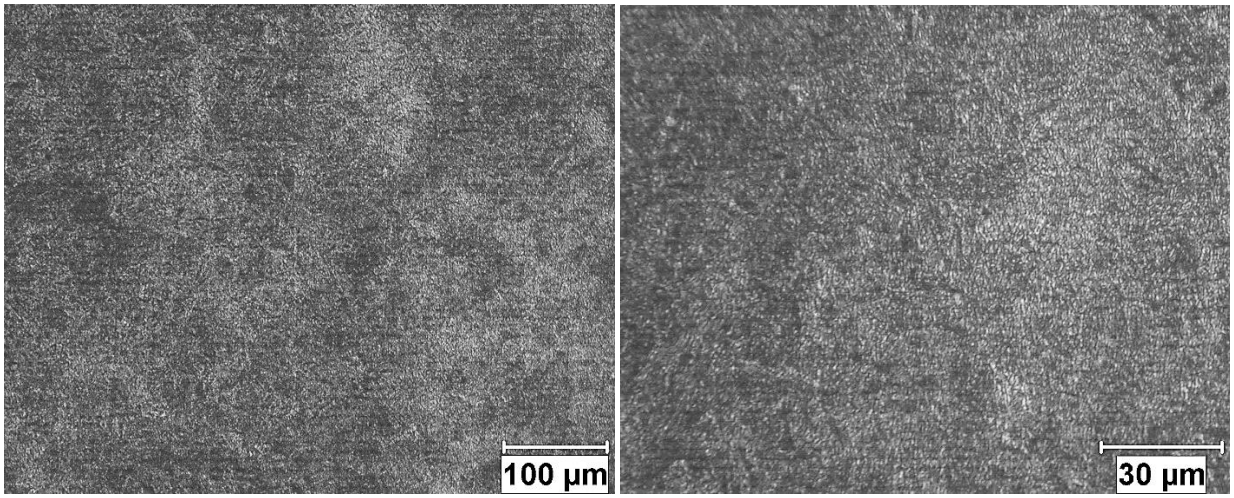

Figure C-4: OM image of Armox 300°C (1 hour exposure, unimpacted) 100x and 400x magnification respectively

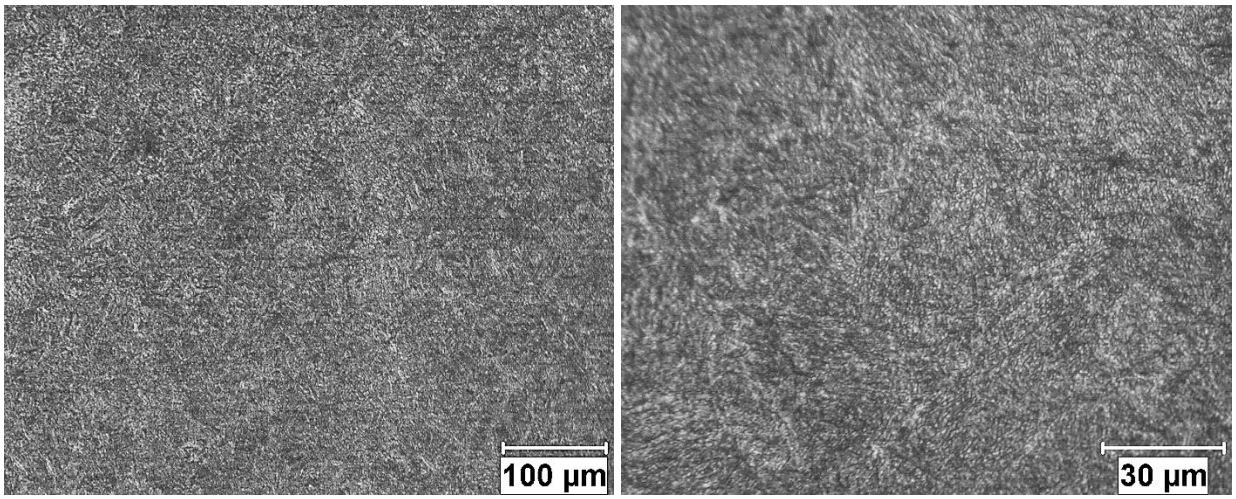

Figure C-5: OM image of Armox 400°C (1 hour exposure, unimpacted) 100x and 400x magnification respectively

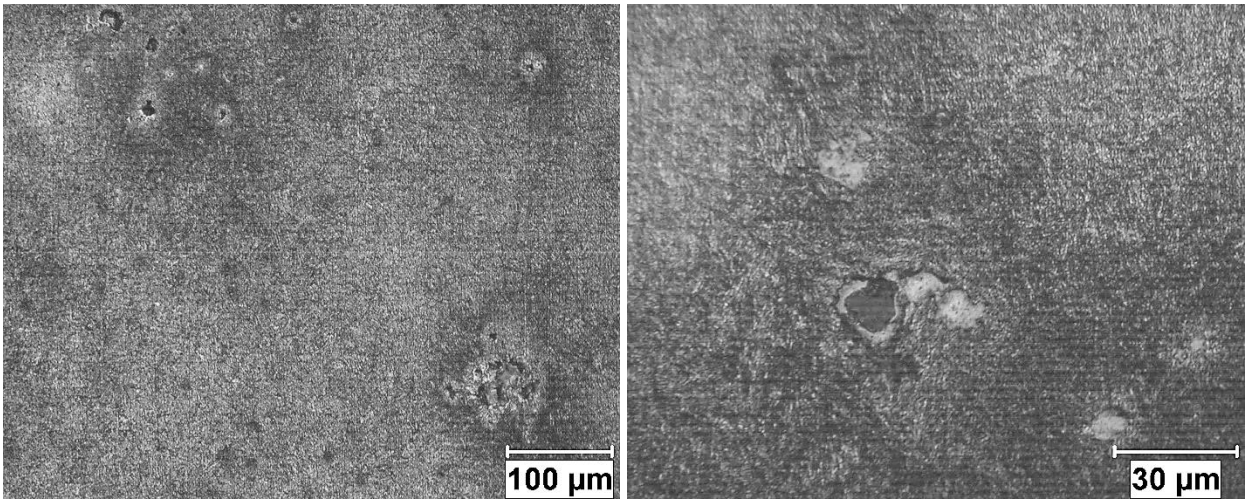

Figure C-6: OM image of Armox 500°C (1 hour exposure, unimpacted) 100x and 400x magnification respectively

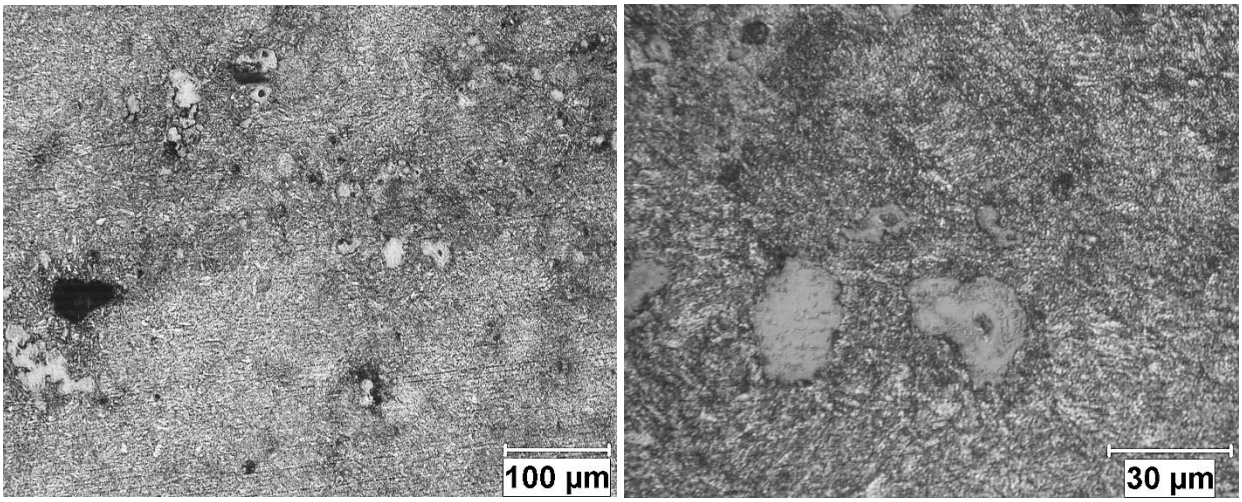

Figure C-7: OM image of Armox 600°C (1 hour exposure, unimpacted) 100x and 400x magnification respectively

9.4 SEM High Temperature Exposure Unimpacted

Using SEM to observe and compare different the different temperature effects on the surface of the material can be seen in Figure C-8 - Figure C-10. Comparing these samples at 5000x magnification, from room temperature to 200°C, it is apparent that there are changes to the microstructure. The length and size of the packets of lathes are reduced to less than 10 µm. There are some large grains still present indicating the original properties are in existence. Observing the 300°C and 400°C exposed samples, the grain sizes are significantly reduced further reduced to les than 5 µm and demonstrates not of the original microstructural property features seen in the room temperature exposed sample.

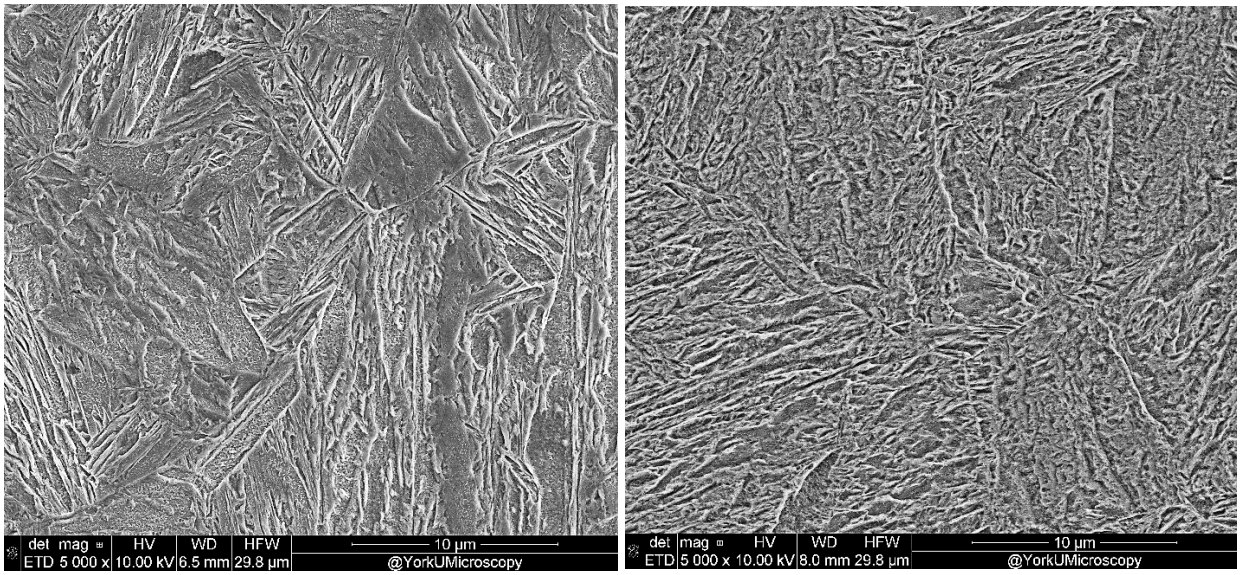

Figure C-8: SEM image of Armox room temperature and 200°C samples respectively (1 hour exposure, unimpacted) 5000x magnification

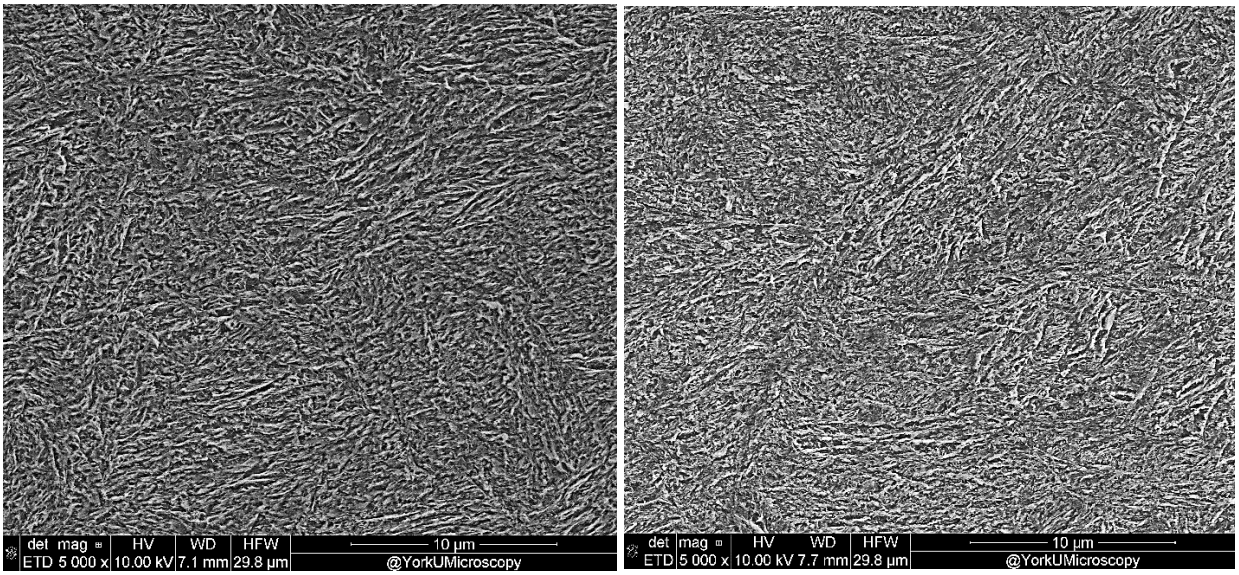

Figure C-9: SEM image of Armox 300°C and 400°C samples respectively (1 hour exposure, unimpacted) 5000x magnification

Observing the 500°C and 600°C exposed samples seen in Figure C-10, it is apparent that there is some form of diffusion of alloying elements and formation of pockets and voids in the material. These voids were found to be more consistent and larger in size in the 600°C sample. These microstructural changes are extreme and demonstrate that the original microstructure is completely compromised. The exact nature of these voids and areas of diffusion as well as its elemental composition can be further analysed using Energy Dispersive Spectroscopy (EDS) analysis.

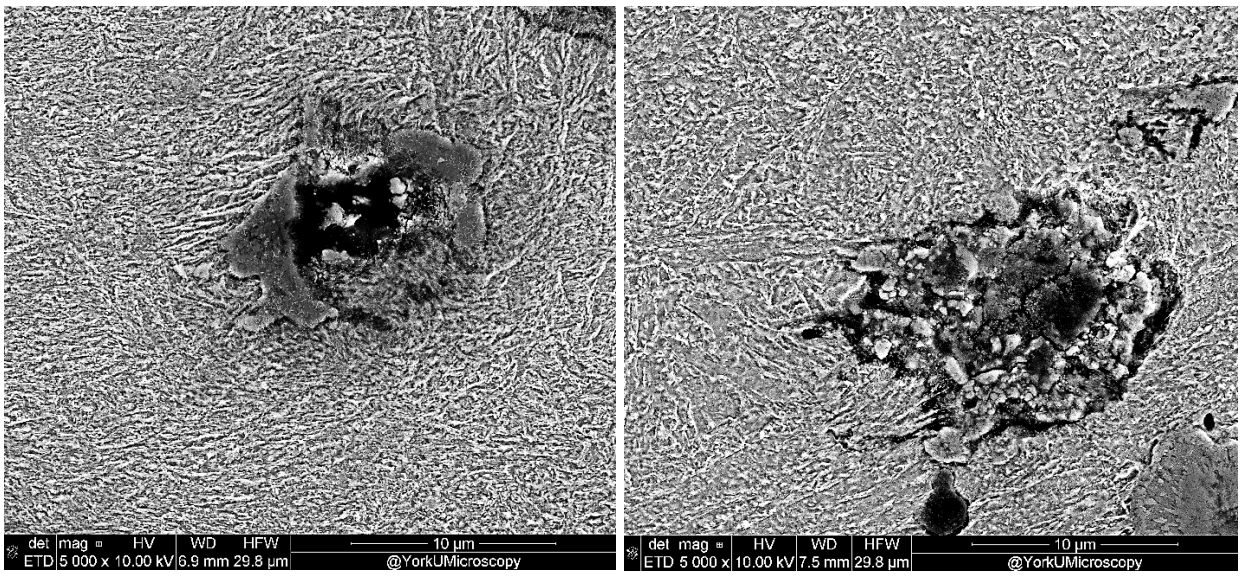

Figure C-10: SEM image of Armox 500°C and 600°C samples respectively (1 hour exposure, unimpacted) 5000x magnification

9.5 Temperature Affects on Armox 500T and its Hardness

The original hardness of the Armox was measured at 53.22 HRC. As the temperature was increased to 200°C, the hardness was slightly reduced to 51.96 HRC, indicating that the hardness is not significantly affected and the microstructure still holds its properties and retained martensitic structure. Beyond this temperature, it is seen that there is a significant decrease in these properties as the hardness drops to well below 50 HRC. This would be a result of loss of martensitic structure and diffusion of critically alloying elements such as carbon.

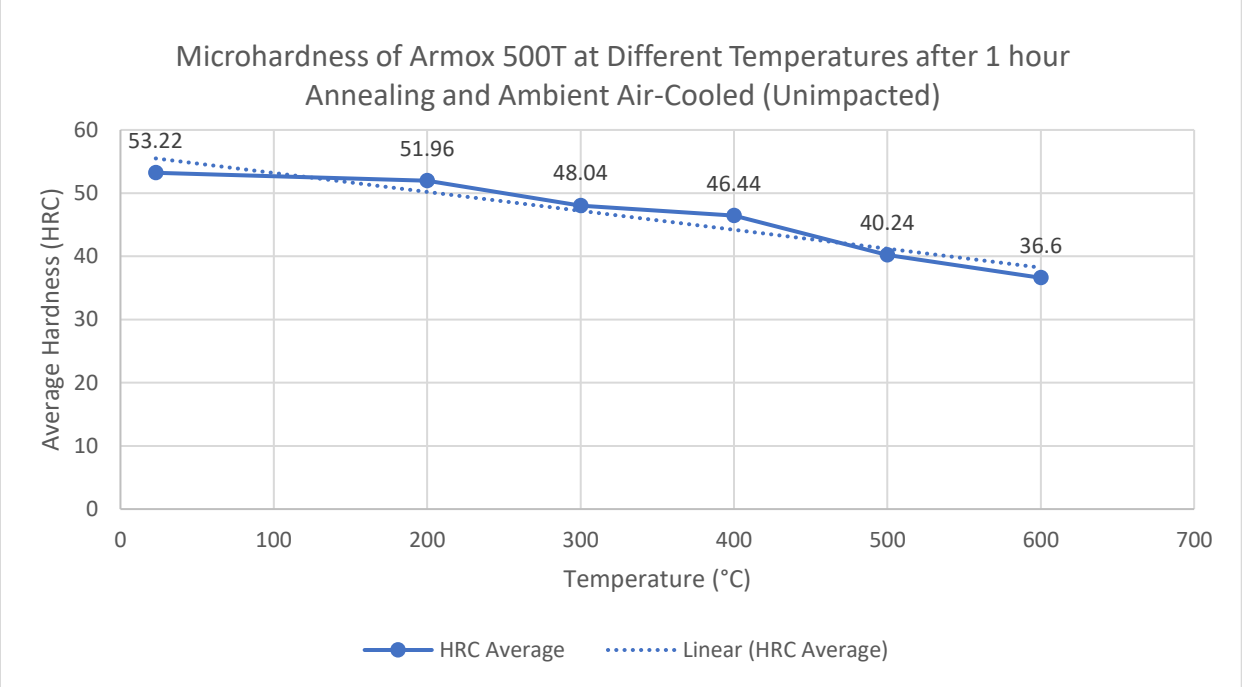

Figure C-11: Microhardness of Armox 500T at different temperatures after 1 hour of annealing and air cooled at ambient temperature